APPLICATIONS OF MICROFLUIDIC CHIPS IN OPTICAL MANIPULATION & PHOTOPORATION

Robert Frank Marchington

A Thesis Submitted for the Degree of PhD
at the
University of St. Andrews

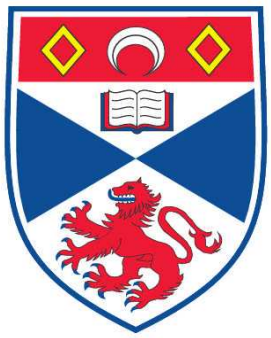

2010

Applications of Microfluidic Chips in Optical Manipulation & Photoporation

Robert Frank Marchington

A thesis presented for the degree of
Doctor of Philosophy

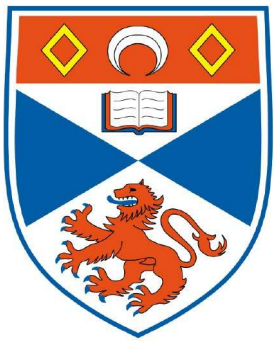

Optical Trapping & Microphotonics Groups
School of Physics & Astronomy
University of St Andrews

June 2010

Dedicated to

Mum & Mike

Joe

& Xanthoula

Applications of Microfluidic Chips in Optical Manipulation and Photoporation

Robert Frank Marchington

Submitted for the degree of Doctor of Philosophy

June 2010

Abstract

Integration and miniaturisation in electronics has undoubtedly revolutionised the modern world. In biotechnology, emerging lab-on-a-chip (LOC) methodologies promise all-integrated laboratory processes, to perform complete biochemical or medical synthesis and analysis encapsulated on small microchips. The integration of electrical, optical and physical sensors, and control devices, with fluid handling, is creating a new class of functional chip-based systems. Scaled down onto a chip, reagent and sample consumption is reduced, point-of-care or in-the-field usage is enabled through portability, costs are reduced, automation increases the ease of use, and favourable scaling laws can be exploited, such as improved fluid control. The capacity to manipulate single cells on-chip has applications across the life sciences, in biotechnology, pharmacology, medical diagnostics and drug discovery.

This thesis explores multiple applications of optical manipulation within microfluidic chips. Used in combination with microfluidic systems, optics adds powerful functionalities to emerging LOC technologies. These include particle management such as immobilising, sorting, concentrating, and transportation of cell-sized objects, along with sensing, spectroscopic interrogation, and cell treatment.

The work in this thesis brings several key applications of optical techniques for manipulating and porating cell-sized microscopic particles to within microfluidic chips. The fields of optical trapping, optical tweezers and optical sorting are reviewed in the context of lab-on-a-chip application, and the physics of the laminar fluid flow exhibited at this size scale is detailed. Microfluidic chip fabrication methods are presented, including a robust method for the introduction of optical fibres for laser beam delivery, which is demonstrated in a dual-beam optical trap chip and in optical chromatography using photonic crystal fibre.

The use of a total internal reflection microscope objective lens is utilised in a novel demonstration of propelling particles within fluid flow. The size and refractive index dependency is modelled and experimentally characterised, before presenting continuous passive optical sorting of microparticles based on these intrinsic optical properties, in a microfluidic chip.

Finally, a microfluidic system is utilised in the delivery of mammalian cells to a focused femtosecond laser beam for continuous, high throughput photoporation. The optical injection efficiency of inserting a fluorescent dye is determined and the cell viability is evaluated. This could form the basis for ultra-high throughput, efficient transfection of cells, with the advantages of single cell treatment and unrivalled viability using this optical technique.

Declarations

Candidate's declarations:

I, Robert Frank Marchington, hereby certify that this thesis, which is approximately 41,000 words in length, has been written by me, that it is the record of work carried out by me, and that it has not been submitted in any previous application for a higher degree. I was admitted as a research student in November 2005 and as a candidate for the degree of Doctor of Philosophy in June 2006; the higher study for which this is a record was carried out in the University of St Andrews between 2005 and 2010.

Date ..... Signature of Candidate .....

Supervisor's declarations:

I hereby certify that the candidate has fulfilled the conditions of the Resolution and Regulations appropriate for the degree of Doctor of Philosophy in the University of St Andrews and that the candidate is qualified to submit this thesis in application for that degree.

Date ..... Signature of Supervisor .....

Permission for electronic publication:

In submitting this thesis to the University of St Andrews I understand that I am giving permission for it to be made available for use in accordance with the regulations of the University Library for the time being in force, subject to any copyright vested

in the work not being affected thereby. I also understand that the title and the abstract will be published, and that a copy of the work may be made and supplied to any bona fide library or research worker, that my thesis will be electronically accessible for personal or research use unless exempt by award of an embargo as requested below, and that the library has the right to migrate my thesis into new electronic forms as required to ensure continued access to the thesis. I have obtained any third-party copyright permissions that may be required in order to allow such access and migration, or have requested the appropriate embargo below.
Access to printed copy and electronic publication of thesis through the University of St Andrews.

Date ..... Signature of Candidate .....

Signature of Supervisor .....

Acknowledgements

I would like to begin by thanking my supervisor Professor Kishan Dholakia, for the opportunity to work in his group, for all the support and guidance he has given me, and for always taking time to help out when needed. I would also like to thank Professor Thomas Krauss for the opportunity to work in his group, and for all the useful discussions with him also. I would like to thank them both for giving me the flexibility in carving my own directions of exploration.

The work here has been collaborative throughout and there is a huge array of people to thank. Firstly, the two people that everything hinged on, the legendary George Robb and Stevie Balfour, for their continued efforts in the running of the cleanroom, fixing of equipment and generally helping out in so many occasions. Also to Will and Chris for all of their time and continued help in the cleanroom and SEM, and to Chris and Mark in electronics and all of the workshop guys for making stuff work when it had to!

I'd very much like to thank Peter Reece, for his inspiration, letting me come scribble all over his white board, for the brilliant discussions and ideas that would continue on to the Whey Pat. A big thanks to Klaus also, for always being helpful and for teaching me the ropes with the fibre trap. Thanks to Vene for being terrific fun and for all the days on the evanescent work. My lab partner, and office mate, Steve, thanks to you for all your time throughout on so many projects I've lost count, but most recently on the bacteria work.

Many thanks to Dave Stevenson for all the bio chip cell zap chat throughout, and helping out so so many times and aspects. The same to Lani, thanks for looking after the cells and helping out. Thanks to Lynn and Muriel also. And thanks go to Frank for his help most recently on the photoporation work, but also generally for

his interest and feedback throughout.

A big thanks goes to Praveen, for his help in all aspects, from chips, to optics, for all the useful discussions, his lab work and the proof reading. Many thanks also to Doug and Andrea for their help and good times working together, which I extend to Mark who was also kind enough to proof read as well. Thanks also to Helen for her recent efforts in the microfluidics. Also, thank you Peru for being great fun and an doing excellent job on the seal tag project. Thanks to Bernie and Ailsa for giving us that opportunity.

Many thanks to Wei Huang for the bacteria samples, and thanks to him and Patience for telephone reassurance after I drank them. From my time in the office, I'd like to show my appreciation of the good old days with Dave Gherardi, Phil, Graham, Dan & Dan. Especially to Graham for his particle tracking software, and his good words on Kishan and the group in the first place, that meant I applied. I express my gratitude to Michael for all his hard work on the modelling, for his insights, for taking the time for us to discuss the theory and proof reading my thesis. Thanks to Anna Chiara for being so helpful during the writing up stage, keeping the place running smoothly.

Dave Walsh and Pete need thanking for their amazing homebuilt water cooler, that we installed in the finals hours, saving the day. And thanks for helping out with all the computer troubles and the shutter mounting Dave. Sorry again for breaking that fan! And thanks to Dave Stothard for his continuous source of amusement photographically and acoustically from his nearby lab, and to Tom Edwards for inspiring me to stick around in St Andrews in the first place.

A Very big thanks to Yoshi for his immense input into the work in this thesis, for all of his input, his continued efforts and being a great guy to work with.

On a more personal note I'd like to thank Mum and Mike for their continued support and encouragement, and particularly Mum for proof reading this entire thesis. And a very big thanks to Xanthi for all of her help in the lab, the discussions throughout, motivating me, helping at the weekends, standing in with the cell work and proof reading this thesis.

Publications

Peer Reviewed Publications

[1] R. F. Marchington, Y. Arita, X. Tsampoula, F. Gunn-Moore, and K. Dholakia, "High throughput optical injection of mammalian cells using a microfluidic platform," Biomedical Optics Express 1(2), 527-536, 2010. (See Chapter 6)

[2] P. C. Ashok, R. F. Marchington, P. Mthunzi, T. F. Krauss, and K. Dholakia, "Optical chromatography using a photonic crystal fiber with on-chip fluorescence excitation," Optics Express 18(6), 6396–6407, 2010. (See Chapter 4)

[3] R. F. Marchington, M. Mazilu, S. Kuriakose, V. Garcés-Chávez, P. J. Reece, T. F. Krauss, M. Gu, and K. Dholakia, "Optical deflection and sorting of microparticles in a near-field optical geometry," Optics Express 16(6), 3712-3726, 2008. (See Chapter 5)

[4] W. M. Lee, P. J. Reece, R. F. Marchington, N. K. Metzger, and K. Dholakia, "Construction and calibration of an optical trap on a fluorescence optical microscope," Nature Protocols 2(12), 3226–3238, 2007. (See Chapter 1)

[5] N. K. Metzger, R. F. Marchington, M. Mazilu, R. L. Smith, K. Dholakia, and E. M. Wright, "Measurement of the Restoring Forces Acting on Two Optically Bound Particles from Normal Mode Correlations," Physical Review Letters 98(8), 068102, 2007. (See Chapter 4)

[6] K. Dholakia, W. M. Lee, L. Paterson, M. P. Macdonald, R. Mcdonald, I. Andreev, P. Mthunzi, C. T. A. Brown, R. F. Marchington, and A. C. Riches, "Optical separation of cells on potential energy landscapes: Enhancement with dielectric tagging," IEEE Journal of Selected Topics in Quantum Electronics 13(6), 1646–1654, 2007. (See Chapter 1)

Conference Proceedings

[7] R. F. Marchington, Y. Arita, D. Stevenson, F. Gunn-Moore, and K. Dholakia, "High throughput photoporation of mammalian cells using microfluidic cell delivery," in CLEO, San Jose, (JMC6), 2010. (See Chapter 6)

[8] Y. Arita, R. Marchington, D. Stevenson, F. Gunn-Moore, and K. Dholakia, "High Throughput Photoporation of Mammalian Cells using Microfluidic Cell Delivery," in Biomedical Optics (BIOMED), (BTuD92), OSA, (Miami, Florida, USA), 2010. (See Chapter 6)

[9] P. C. Ashok, R. F. Marchington, M. Mazilu, T. F. Krauss, and K. Dholakia, "Towards integrated optical chromatography using photonic crystal fiber," in Proceedings of SPIE, 44(74000R), SPIE, (San Diego, CA, USA), 2009. (See Chapter 4)

[10] D. M. Gherardi, A. E. Carruthers, T. Cizmar, R. F. Marchington, and K. Dholakia, "Novel dual beam fiber traps using endlessly single-mode photonic crystal fiber," in Proceedings of SPIE, (703828), SPIE, (San Diego, CA, USA), 2008. (See Chapter 4)

Patents

[11] Application: The University of St Andrews, R.F. Marchington, P. Ashok, K. Dholakia, "Optical Trap," (Marks & Clerk, Glasgow, UK), WO/2010/007371, 21/01/2010.

List of Abbreviations

1D One dimensional

2D Two dimensional

3D Three dimensional

AC Alternating current

ACE Acetone

BA Back aperture

B. Anthracis Bacillus anthracis bacteria (Anthrax)

B. Thuringiensis Bacillus Thuringiensis

C. elegans Caenorhabditis elegans

CAD Computer aided design

Calcein AM Calcein acetoxymethyl ester

CAM Calcein AM

CARS Coherent anti-Stokes Raman scattering

CCD Charge coupled device; camera

CMOS Complementary metal oxide semiconductor

CW Continuous wave

D_2O Deuterium oxide, heavy water

DEP Dielectrophoresis

DIH_2O Deionised water

DMEM Dulbecco's modified Eagle's medium

DNA Deoxyribonucleic acid

DOE Diffractive optical element

DsRed Double strand plasmid DNA; red fluorescent protein

EC solvent Glycol monomethyl ether acetate, MicroChem photoresist solvent

FACS Fluorescence-activated cell sorter

FCS Fetal calf serum

FFF Field-flow fractionation

fs Femtosecond

GaAs Gallium arsenide

GPS Global positioning system

HEK293 Human embryonic kidney 293 cell line

HIV Human immunodeficiency virus

HL60 Human promyelocytic leukemia 60 cell line

hr Hours

IPA Isopropanol

IR Infrared radiation

LG Laguerre-Gaussian

LMA Large mode area

LOC Lab-on-a-chip

MACS Magnetic-activated cell sorter

MEM Modified Eagle's medium

μFACS Microfluidic fluorescent-activated cell sorter

Micron Micrometre

min Minutes

μTAS Micro-total-analysis-system

NA Numerical aperture

NOA Norland optical adhesive

p *p*-polarised light (TE)

PCF Photonic crystal fibre

PDMS Poly(dimethylsiloxane)

PI Propidium iodide

PMMA Poly(methyl methacrylate)

Pol Polarisation

PSD Power spectral density

QPD Quadrant photodiode

RACS Raman-activated cell sorter

RBC Red blood cell

RCF Relative centrifugal force

RIE Reactive ion etcher

rpm Revolutions per minute

s *s*-polarised light (TM)

SDS Sodium dodecyl sulphate; surfactant

sec Seconds

SEM Scanning electron microscope

SERS Surface-enhanced Raman scattering

SLM Spatial light modulator

SOI Silicon on insulator

SU8 MicroChem Corp. epoxy-based negative photoresist

TAS Total-analysis-system

TE Transverse electric

TIRFM Total internal reflection fluoresence microscope

TIRF Total internal reflection fluoresence

TIR Total internal reflection

TM Transverse magnetic

UV Ultra-violet

Contents

Chapter 1

Optical Manipulation of Microscopic Particles

In the realms of science fiction, the concepts of tractor beams and force fields are familiar to all of us. The year 2010 marks the fortieth anniversary of Ashkin's first laboratory demonstrations of trapping and moving objects using beams of light [12]. For the time being, moving large planet-sized spaceships is a little out of reach for the picoNewton forces produced by light, but none the less, optical traps and tweezers are now in use in laboratories all over the world for a wide range of applications involving trapping, manipulating or probing micrometre and smaller sized objects. The familiar interactions of reflection and refraction are exchanges of momentum between light and an object, capable of exerting sizeable forces on the micrometre scale; the size regime of bacteria, yeast, cells and some of the smallest living organisms.

Particles or living cells can be completely immobilised in an optical trap, picked up and moved around using optical tweezers, or propelled across surfaces in an optical guide. Different sizes or refractive indices of these particles have varied responses to optical fields, allowing the fractionation of particles in optical sorting devices, using optical forces alone, and without the need for additional markers or tags. In optical nanosurgery, a focused laser beam is capable of punching self-healing pores (photoporation) in the cell membrane for optically-mediated insertion of drugs, foreign DNA or other agents, without damaging the integrity of the cell.

Used in combination with microfluidic systems, optics adds powerful functionalities to emerging lab-on-a-chip (LOC) technologies. *En route* to complete, large-scale biochemical and biomedical analysis or synthesis, encapsulated on a small chip, the field has seen a surge in development and application in the last decade [13]. Miniaturisation of laboratory processes brings advantages such as portability, reduced costs, point-of-care usage, automation and reduced reagent consumption. The integration of these systems with the full optical manipulation "toolbox", adds additional functionality such as particle management including routing, sorting and concentrating; spectroscopic detection and interrogation; and cell injection.

This thesis addresses optical trapping, sorting and injection of particles and cells, in centimetre-sized self-fabricated microfluidic chips. This chapter reviews the field of optical manipulation in the context of applicability to microfluidics and LOC. The behaviour of fluids in microscopic dimensions is non-intuitive and quite different to our macroscopic experience, and Chapter 2 details the fundamentals of fluids in the microfluidics regime. Chapter 3 describes the fabrication of these microfluidic chips using soft lithography techniques, and in Chapter 4 a versatile method for the integration of optical fibres for in-chip beam delivery is presented. Chapter 4 demonstrates the use of these integrated fibres in optical trapping for fundamental studies on optically bound matter, and photonic crystal fibre is applied to optical chromatography. Chapter 5 describes investigations into a novel near-field technique for the insertion of evanescent light into microfluidic chips for optical sorting of particles by intrinsic optical properties, and Chapter 6 demonstrates microfluidic focusing and delivery of cells to a focused femtosecond laser beam for high throughput optical injection of a fluorescent dye.

1.1 Introduction

In the realm of microfluidics, optical traps, tweezers and guides offer a huge array of functionalities to LOC or total analysis systems (μTAS) . Optical fields within microfluidic environments can immobilise cells in a fluid flow to allow long spectroscopic acquisitions [14]; expose cells to controlled concentration gradients of chemi-

cals in laminar flow environments [15]; shunt particles at will within an integrated optoelectronic chip with microfluidic networks [16]; position microlenses within fluid channels between on-chip optical components [17]; act as optical switches to deflect particles in fluorescent-activated sorting devices [18]; or direct droplet-encapsulated samples in digital microfluidics [19, 20].

A number of new optical applications within microfluidic environments are explored throughout the work presented in this thesis. In Chapter 4, a dual-beam trap is utilised for probing the nature of optically bound matter. Optical chromatography using photonic crystal fibre accomplishes sensitive particle fractionations based on size, refractive index and the presence of a dielectric tag in Chapter 4. Evanescent fields are coupled into a microfluidic channel using the objective lens of the microscope for size-based fractionation of particles and simultaneous imaging in Chapter 5; and in Chapter 6, a controlled microfluidic delivery of mammalian cells to a focused femtosecond beam enables the first realisation of high throughput optical injection of a reagent, into thousands of cells during short experimental runs.

Serving as a background to the explored optical geometries and techniques realised throughout the thesis, this chapter starts on the topic of optical trapping and tweezing. In view of their utilisation in applications for LOC systems, on-chip approaches to the dual-beam trap geometry are detailed, before looking at the external introduction of optical tweezers into fluidic chips, and the governing gradient and scattering forces. Advanced optical methods are discussed, including some "novel" beams with fascinating propagation properties such as the Bessel beam and Airy beam, and the introduction of evanescent fields using waveguides or total internal reflection (as utilised in Chapter 5). Finally, the topic of optical sorting and optical potential energy landscapes for the passive fractionation of particles based on their intrinsic optical properties, is introduced, along with a review of alternative and complementary non-optical sorting techniques.

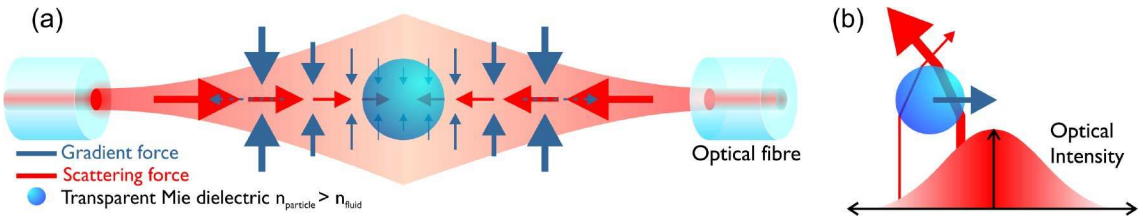

Figure 1.1: *(a) A dual-beam fibre optical trap. Two divergent co-aligned counter-propagating beams will attract and immobilise a particle. The trapping force on a particle can be split into two components; the scattering force that acts in the direction of beam propagation and the gradient force that acts in the direction of highest optical intensity. (b) Illustration the optical gradient force, on a Mie particle (diameter larger than the optical wavelength). Light is refracted as it passes through the particle and imparts momentum on it such to conserve that due to the ray's directional change, giving rise to a net* gradient *force pulling the particle towards the region of highest optical intensity.*

1.2 Optical Trapping in Microfluidic Environments

1.2.1 Dual Beam Optical Trapping

The first demonstration of an optical trap by Ashkin [12] consisted of two divergent, co-aligned and counterpropagating laser beams, directed into a sample chamber containing transparent 3 μm latex beads. Ashkin found that beads that drifted near either beam were drawn in and accelerated towards the other beam, until coming to rest at a stable equilibrium point between the two. Blocking either beam caused the bead to be accelerated away from the remaining beam. The beam divergence, as necessary to form a stable trap was achieved using free-space optics, more recently the versatility of dual beam trapping has been increased with the use of single mode optical fibre for divergent beam delivery, as demonstrated by Constable and Kim [21] and as shown in Figure 1.1.

Figure 1.1 shows schematically the two optical-derived forces behind the effects observed by Ashkin. The first of these forces was hypothesised by the astronomer Kepler in the 17th century. To explain his observation that a comet's tail always points directly away from the sun regardless of the comet's trajectory, he proposed a so called radiation pressure to explain the effect. Photons carry h/λ momentum (where h is Planck's constant and λ is the wavelength) and upon incidence on a reflecting surface, a photon receives a momentum change of$-2h/\lambda$ upon reflection, and $+2h/\lambda$ is exerted on the mirror to conserve momentum, which is realised as a

force on the mirror. For Ashkin's latex bead in the trap, only a portion of light is reflected (as governed by the Fresnel equations [22]), but this *scattering force* is picoNewtons in size and capable of guiding and trapping the beads as observed.

The second force is the *gradient force* and, as visualised in Figure 1.1b arises from the refraction of light as it passes through the bead. The bead bends light rays as they pass through, changing their direction, and so the bead receives some momentum, realised as a force, and in a direction towards the light ray. Rays of higher intensity will exert larger forces, thus the net force acting on a bead will be towards the region of highest optical intensity. For a dual beam trap, it is the gradient force that pulls in the bead in the lateral direction, and the scattering force that traps it in the axial direction.

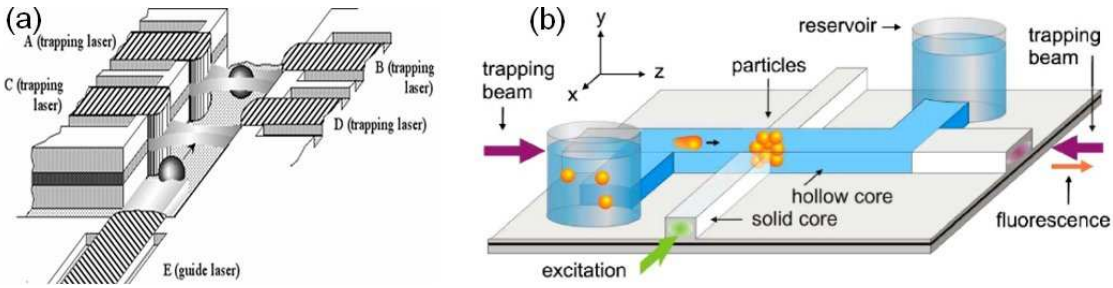

Figure 1.2: *Two integrated optical trapping systems. (a) Microfluidic channels and etched into a GaAs quantum well wafer, along with ridge waveguide laser structures, allowing the integration of various optical trapping and guiding geometries and microfluidic circuits* [16]. *(b) Fluid-core waveguides are utilised for trapping and concentration of particles inside the waveguide, for subsequent excitation of fluorescence using an orthogonal solid-core waveguide* [23].

Compared to non-divergent trapping geometries (the topics of Section 1.2.2-1.3.2), dual beam traps have several advantages; the use of divergent beams facilitates large capture volumes, and as the optical power is distributed across the whole particle rather than focused to a small region, the risk of absorption-induced photodamage to biological particles is minimised. Dual beam traps are much more capable of trapping larger particles (up to 0.1 mm has been demonstrated [24]) and high index particles [25]. The relative ease of positioning waveguides with divergent outputs in close vicinity to microfluidic channels has given dual beam traps its recent resurgence of interest, in view of the advantages drivers towards LOC systems. These include the possibilities of total analysis systems on a single portable, cheap, dis-

posable and sterile chip. Optical traps, as one of an array of tools for chip-based systems have demonstrated: immobilising cells in a fluid flow for fluorescence [26] and Raman spectroscopy [24] acquisitions; concentrating particles [23]; rotating cells for complete 360^o imaging [27]; stretching cells to obtain elasticity information for investigations into cancers [28,29]; trapping and size-dependent translation of nanoparticles [30].

The waveguides used in dual beam traps to date predominantly have been single mode optical fibres [17, 21, 24, 25, 30–32], but integrated liquid-core [23], embedded femtosecond-written [33] and photonic crystal fibre [30] have also been used. A novel and LOC approach approach by S. Cran-McGreehin *et al.* [16] removed the requirement for external laser sources and waveguides through the incorporation of semiconductor lasers onto the microfluidic chip itself (see Figure 1.2). A rapid method for incorporating optical fibres into the commonly used chip material PDMS, is demonstrated in Chapter 4 with a full protocol for creating a pre-aligned fibre trap with integrated microfluidic channels for particle delivery.

1.2.2 Single Beam Optical Tweezers

A dual beam trap can immobilise single or multiple particles along the axis of two counter-propagating beams, and by changing the relative intensities of the two beams, one is able to move particles in one degree of freedom along the optical axis. In 1986 Ashkin reported a trapping geometry that revolutionised micromanipulation [34], a tool to later to become known as *optical tweezers*. With applications from the unravelling of DNA to *in vitro* fertilisation, optical tweezers offer the ability to trap and freely manoeuvre microscopic objects in three dimensions using purely the forces of light [35], utilising only the gradient forces from a single focused beam.

The work horse of single cell manipulation, optical tweezers have developed into an amazingly versatile, sensitive and very calibrateable tool for the biophysical sciences [36]. Not only can single cells or other microscopic particles be picked up and moved around, but measureable forces can be extracted down to sub-picoNewton resolution [4]. Figure 1.3 illustrates how a single laser beam, focused by a high numerical aperture (NA) microscope objective lens can exert gradient forces in three

dimensions such to trap a microscopic particle.

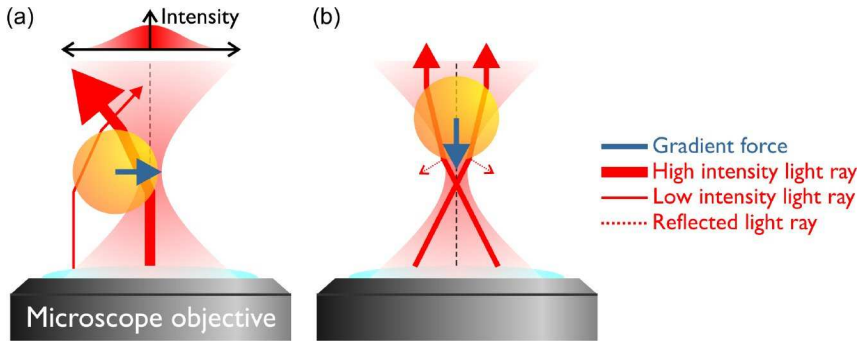

Figure 1.3: *Illustration of how optical tweezers can trap a particle in three dimensions using one focused beam. (a) Laser light is focused by a high numerical aperture (NA) objective lens to form a tightly focused diffraction-limited spot. The light is refracted through the particle and imparts momentum on it such to conserve that due to the ray's directional change. Regions of highest optical intensity have a larger contribution and thus there is a net force acting on the particle, towards the region highest intensity (the gradient force), i.e. towards the beam focus. If the gradient forces are higher than all resistive forces (such as Stokes drag force and gravitation), then the particle will move to and become trapped at the focus. Moving the position of the focus will in turn move the particle allowing a particle to be picked up and transported at will in its environment. (b) Similar ray-tracing arguments can be applied in the axial direction, giving rise to 3D trapping using gradient forces alone. There is a slight displacement of the sphere from the beam focus in the axial direction due to additional force contributions from radiation pressure and gravity.*

Optical tweezers have been used to simultaneously immobilise cells and obtain spectroscopic signals [14, 37]; probe surface interactions or fluids in microrheology studies [38]; influence the growth of light-sensitive organisms [39] and neurons [40]; and position a single metallic nanoparticle for subsequent femtosecond optical injection through a cell membrane [41]. One can even use micrometre sized colloidal particles as handles for even smaller objects, such as proteins or macromolecules including single strands of DNA [42–44], allowing one to tweeze and measure forces down to femtoNewtons with Angstrom level precision.

Directing optical tweezers into a microfluidic channel inside a chip is interchangeable to their use in a Petri dish of cells, with the requirement of optically flat transparent entrance surfaces (for minimal aberration) and that the distance into the channel is within the working distance of the objective lens (typically 170 μm). Optical tweezers can facilitate the loading of multiple particles into dual beam traps [5, 45]; positioning microlenses [17]; exposing cells to different fluid flow streams [15]; directing particles within sorting schemes [18]; and making force mea-

surements using trapped microspheres such as quantifying fluid flow velocities [46].

A typical optical tweezers setup is shown in Figure 1.4, detailing the optics required to deliver a diffraction-limited focal spot to within a sample chamber, and that can be translated using a *steering mirror* for moving the trapping particles. By placing the steering mirror at the conjugate plane to the back aperture, the beam can be repositioned within the sample, whilst ensuring it still passes directly through the back aperture of the objective lens.

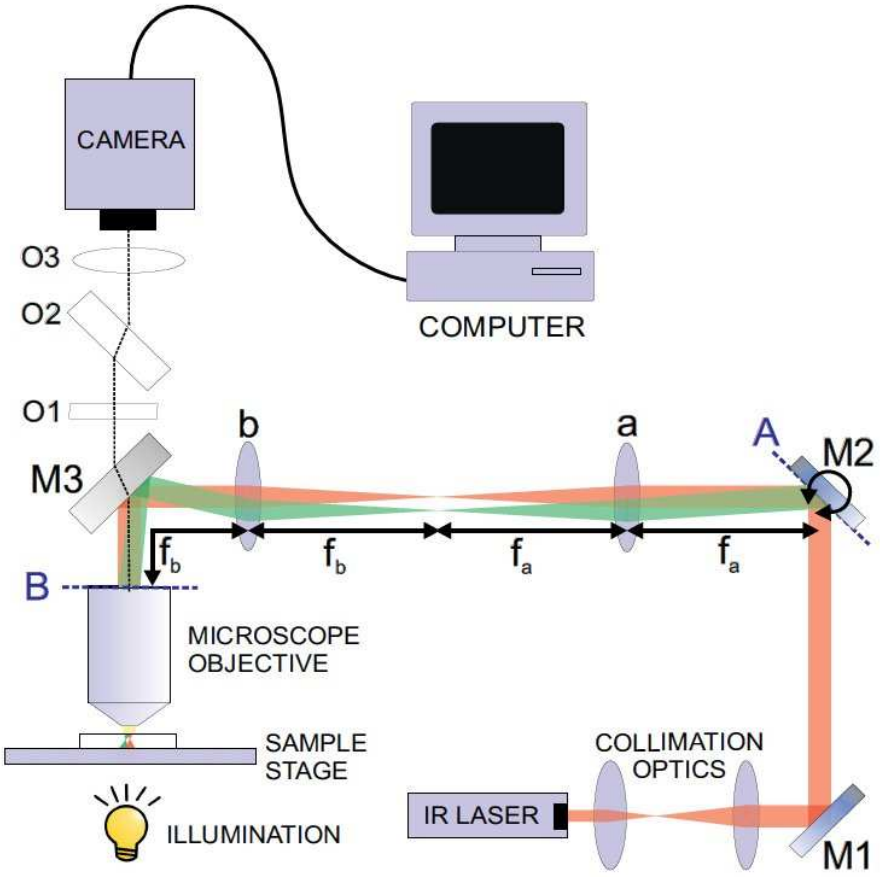

Figure 1.4: *An overview of a basic optical tweezers system. The laser output is expanded and collimated using a pair of lenses, such that the size delivered to the back aperture* B *of the microscope objective is overfilling, thus making full use of the numerical aperture to obtain the smallest possible spot (diffraction-limited) in the sample plane. The mirrors* M1 *and* M2 *act as a periscope. In order to tweeze a trapped particle around in the sample, lenses* a *and* b *relay the image at* M2 *(the "steering" mirror) to the back aperture* B*, such that they are conjugates, such that the location of of the beam on the back aperture is maintained at all times. A change in angle of* M2 *then translates to a change in angle at B, and consequentally a change in position of the focal spot in the sample plane.* M3 *is a dielectric to reflect the infrared tweezers beam, but transmit visible light, such that the sample can be imaged using a CCD camera. An infrared filter* O1*, a path corrector* O2 *and a tube lens* O3 *may also be included depending on the exact optics used.* [47]

1.2.3 Calibration & Force Measurements

An optical trap represents a potential energy well for a trappable object that can be fully characterised using a number of techniques. The forces in a trap are analogous to that of a Hookean spring (for a low Reynolds fluid), with force being proportional to displacement in such a harmonic oscillator. Thus, the perturbation to a trapped bead indicates an external force, which may be readily measured from the position of the bead. An optical trap can therefore act as a force transducer, readily capable of picoNewton force measurements [4, 48].

For trapping on-chip, the most utilised method of force measurement is through the Q-value; a dimensionless number defining the efficiency of transfer of momentum from the optical beam to the particle [48]:

$$F = Q\,\frac{n_{medium}P}{c} \tag{1.1}$$

where F is the force that needs to be overcome to remove the particle from the trap for a given optical power P, in a fluid medium of refractive index n_{medium} and where c is the speed of light. Q can readily be found through the use of a microfluidic flow or a motorised microscope stage, to translate the fluid surrounding the particle at a known (or measurable) velocity. By increasing this velocity, at some point the Stokes fluid drag force overcomes the trapping force and the particle escapes the trap. Calculating this threshold Stokes drag force and equating it to Equation 1.1 reveals a value for Q. Relative values of Q can quantify changes to the particle or the fluid, and if the Stokes force can be calculated, absolute forces can be obtained. Details of the Stokes fluid drag force, and importantly the required numerical correction (Faxén correction) to account for the influence of a nearby boundary surface are discussed in Section 2.5. Q-values can be used for example, to obtain fluid viscosities and/or temperature [49], map out flow-induced shear stresses in microfluidic channels [46], identify regional refractive index changes, or measure the mobility of sperm cells for instance [50].

The Q-value obviously has some drawbacks in that a fluid flow must be introduced, that the particle is lost from the trap in every measurement, and that it is

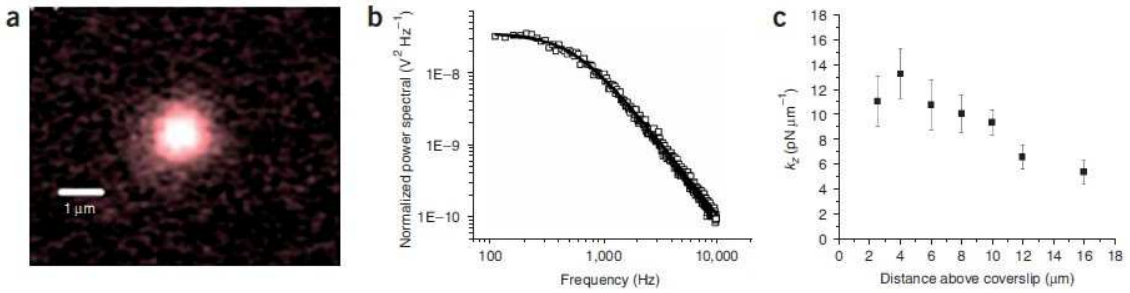

Figure 1.5: *Measurement of optical tweezers trap stiffness for a (a) single trapped colloid by the use of a QPD. (b) The power spectral density of the Brownian-driven fluctuations in position of a trapped particle are Lorentzian in nature, whose roll-off or corner frequency is proportional to the force exerted on the trapped particle by the optical tweezers. (c) Trap stiffness, k_z as a function of distance from the coverslip z, revealing the increasing influence of chromatic aberrations on the quality of the focused beam. The influence of increasing Stokes drag as the particle is brought closer to the surface (see Section 2.5) was incorporated into the QPD analysis software.* [4]

difficult to take measurements from precise locations with a moving sample stage. More crucially, the Q-value obtained depends ultimately on the experimental setup, with no two optical tweezers delivering the same value for identical samples, and its value will even change over time for the same system due to mechanical drift and optical misalignments. An alternative measurement, the trap stiffness, is setup-independent, yielding absolute force measurements ($\leq$picoNewton), without prior calibration, or the introduction of fluid flow or other external forces. The method relies purely on the Brownian-induced fluctuations of the particle position over time, which may be measured using a fast camera or quadrant photodiode (QPD). An optically trapped particle in a low Reynolds fluid is analogous to an overdamped harmonic oscillator, which is driven to oscillate by thermally generated Brownian motion [48]

$$m\frac{d^2x}{dt^2} + \gamma\frac{dx}{dt} + k_x x = F_f(t) \tag{1.2}$$

where the first term, the inertial component for particle mass, m can be neglected, γ is the Stokes drag coefficient, k_x is the trap stiffness, x is the position simplified here to one dimension, and $F_f(t)$ is the driving time t dependent Browian motion force. By recording either the time-dependent position of the particle, or the frequency response of the fluctuations in the position, the potential well and trapping force

(stiffness) can be inferred.

There are two typical setups for accomplishing this [4]. The first [5] is to acquire positional information of the particle over a period of time (dependent upon the pixel resolution, typically of the order of several minutes) using a high frame rate camera (100 - 1000 frames per second) and utilising particle tracking software (pattern-matching based centroid fitting such as [51]) to map its position over time (see Section 4.2 for an example). A more accurate method is to relay the time-varying interference pattern between the incident tweezers beam and the forward scattered light of the trapped particle to a quadrant photodiode (QPD). It can be shown that the power spectral density (PSD), S_{xx} of the positional fluctuations contained within this interferogram, $x(t)$ has a Lorentzian form [48]

$$S_{xx}(f) = \frac{k_B T}{2\pi^2 \gamma (f_c^2 + f^2)} \tag{1.3}$$

where f is the frequency of fluctuation and the roll-off frequency f_c is given by $f_c = \frac{k_x}{2\pi\gamma}$ [48]. This roll-off frequency can be obtained without the requirement for a calibrated detector, and thus is a convenient method for extracting force measurements from a tweezers system. A rapid method for obtaining the trap stiffness of a particle in a dual-beam trap, is by temporarily blocking one of the beams, and measuring the particle position as a function of time as it is restored back to the central equilibrium position [16, 21].

1.3 Novel Beams & Near-Field Geometries in Optical Manipulation

Dual beam traps and optical tweezers are very flexible tools and have a wide applicability of usage across the biosciences. They are both restricting however in that their use is to confined to small interaction volumes. The dual beam trap can only trap particles that pass between the stationary optical beams, and the beam of optical tweezers either side of the focus is highly divergent, restricting the trapping volume to the order of micrometres. The Gaussian beams used in these “conventional” traps

are however, only one of a series of solutions to the Helmholtz wave equation, and many other beams have been utilised in optical manipulation.

1.3.1 Novel Beams

One such beam is the Bessel beam, often termed a "diffraction-free" beam, which is a propagation-invariant solution to the Helmholtz wave equation [52]. A series of concentric rings surrounding a central core contribute to the continued re-forming of its cross-sectional intensity profile as it propagates, producing a beam that does not diffract and that can reform around obstructions. Two good examples of its use are in photoporation where it can be used in place of a tightly focused Gaussian beam to remove the requirement of having to accurately position the focus on the cell membrane [53]; and in optical sorting as described later in Section 1.10.

A recently exhibited and rather exotic beam, the Airy beam propagates parabolically aided by its two side lobes, that has been shown to propel particles and biological cells over 20 μm walls between sample chambers, in what is termed the *optical snowblower* [54, 55]. The ability to shunt cells or particles between large arrays of on-chip sample chambers could have application in cell culture or drug studies, where chemical concentrations could be varied across the chip, or in sorting applications. A Laguerre-Gaussian (LG) beam propagates with a helical phase front and carry orbital angular momentum [56] and as such are capable of exerting a torque on a trapped particle. At the beam centre exists a phase singularity, which manifests itself as a doughnut shaped intensity profile, and therefore is useful for trapping particles of lower refractive index than the surroundings [57, 58] or highly polarsiable (metallic) nanoparticles [59]. The Bessel beam can be formed with a conical lens (axicon) and the LG beam with a spiral phase plate, and all of these beams can be formed using a hologram, preferably via a spatial light modulator (SLM) for dynamic beam alterations, that is placed in the Fourier plane to the objective lens focus.

1.3.2 Near-Field Optical Trapping and Guiding

An increasing number of devices are making use of near-fields for the control of particles on chip. The generation of an evanescent field through total internal reflection (TIR) or waveguiding confines light to a sub-micrometre above a surface, usually being the substrate of the microfluidic device. The topic of TIR is explained in depth in Chapter 5, but for the time being we can tentatively acknowledge that light undergoing TIR at the boundary of a medium of lower refractive index (e.g. surrounding the high index core of a waveguide or above a glass-water boundary) will produce an exponentially decaying evanescent field over a few hundred nanometres. The rapid decay of such an evanescent field produces strong gradient forces for trapping particles, and in the direction of the plane, can exert scattering forces for propelling them across the surface. These phenomena are explored in depth in microfluidic environments in Chapter 5.

1.3.2.1 Prism Configurations

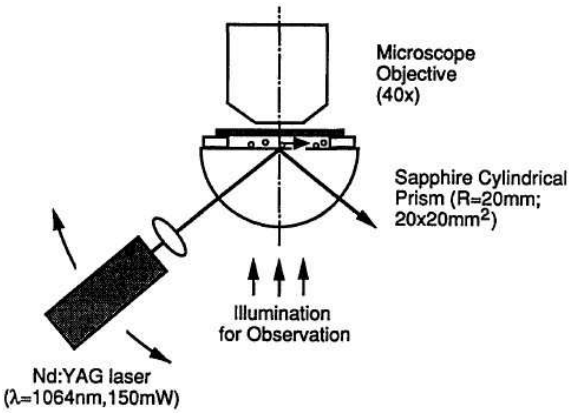

Figure 1.6: *An experimental setup for the generation of evanescent waves through TIR using a semi-cylindrical prism. A sample chamber on the prism allows particles in a fluid medium to be transported across the surface of the prism by the evanescent illumination.* [60]

The simplest method for controlled generation of evanescent fields is by use of a prism, such as that depicted in Figure 1.6 and has been the most widely applied for studies in near-field optical manipulation. Kawata and Sugiura in 1992 [60] first used the geometry to propel 1-27 μm diameter polymer and silica spheres across the prism, obtaining speeds of 20 $\mu m s^{-1}$ for an optical power density of 2.4×10^{-2}

$mW\mu m^{-2}$ at 1064 nm. This work was later extended by Oetama and Walz [61], who verified their experimental observations of evanescent-guided particles with a theoretical model.

More recently, the ability to extend the evanescent illumination to a large area has been employed to optically organise thousands of micro-particles [62]. Techniques such as surface plasmons [63] and optical cavities [64] have been employed, by depositing gold or dielectric layers respectively on to the prism (known as the Kretschmann configuration) for near-field enhancement. The potential use for near-field optical standing waves in size-dependent delivery of micro-particles in a tilted washboard potential has also been demonstrated [65,66], and the possibility of using nano-antennas in a TIR geometry for near-field enhancement has very recently been studied numerically [67].

1.3.2.2 Particle Guiding atop a Waveguide

Evanescent waves can also be accessed at the boundary of an optical waveguide and there are several examples where their applicability has been demonstrated in micro-manipulation. Kawata *et al.* [68] first reported the use of a channelled waveguide for the propulsion of dielectric and metallic particles in 1996, with a similar but more in depth analysis reported later by Grujic *et al.* [69] and the demonstration of the guiding of biological cells by Gaugiran *et al.* [70]. The applicability to active optical sorting was demonstrated by Grujic *et al.* [71] where the two branches of a Y-branching waveguide could selectively be coupled to in real time, allowing particles to be directed along one of two waveguides at will. Schmidt *et al.* [72] investigated the size dependence of the guiding force along a ridge waveguide within an integrated microfluidic chip and more recently Yang *et al.* [73] have reported the routing of particles in and out of a ring resonating waveguide by wavelength tuning. Evanescent guiding has also been demonstrated by Brambilla *et al.* [74] through accessing the evanescent field within an optical fibre by thinning a short section to form a sub-micron nano-wire, upon which micro-particles can be trapped and guided.

1.3.2.3 Near-Field Trapping using Total Internal Reflection Microscope Objective Lenses

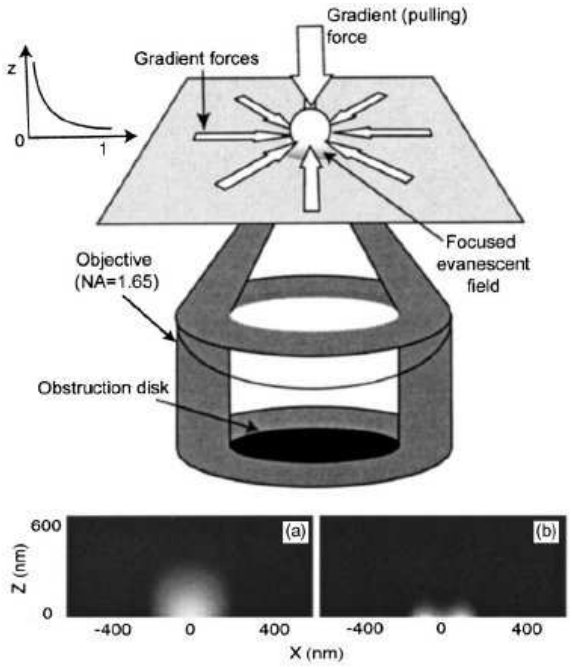

Figure 1.7: *Optical trapping under focused evanescent wave illumination. An obstruction disc is placed at the back aperture (BA) of a total internal reflection (TIR) microscope objective lens, blocking all rays in the sample but those that arrive under TIR conditions. The trapping region is reduced to 10% and 50% in the lateral and axial directions respectively compared to far-field trapping. Non-symmetric illumination of the BA result in guiding forces along the sample surface for trapped particles, as explored in Chapter 5.* [75]

A third method for generating evanescent waves is by use of a TIR objective lens (or TIRF objective lens when used in fluorescence microscopy). The use of TIR objective lenses in the field of optical manipulation has been pioneered by M. Gu and co-workers [75, 76]. By placing an obstructive disc at the back aperture of a TIRF objective lens, rays below the critical angle were excluded, thus producing a purely evanescent illumination in the focal plane and enabling particles to be trapped in the highly confined region through optical gradient forces [75]. The resulting trapping region using the technique was reduced to 10% in the lateral direction and 50% on the axial direction compared to that produced by a non-evanescent far-field trap [75]. TIRF lens trapping has so far been applied to the rotating and stretching of red blood cells [77] and to enhancing multiphoton fluorescence in micro-particles by exciting whispering gallery modes [78].

The first use of a TIR lens for propelling particles is explored in Chapter 5, which after characterising size and refractive index dependence, is applied in a microfluidic chip for continuous sorting of micro-particles by these intrinsic optical properties. The next section reviews the field of optical sorting, putting this passive fractionation into perspective with other methods.

1.4 Fractionation of Microscopic Particles using Optical Fields

Using light to create an optical trap is one example of how optical potential energy, in that case a single potential well, can be used for manipulation of microscopic particles. Tailoring the shape of the potential energy profile can produce interesting optical fields for particles to interact with. This section reviews the use of a variety of *optical potential energy landscapes* for passively sorting particles based on their intrinsic optical properties, such as refractive index, shape or size. This will serve as a background for Chapter 5 where the use of evanescent waves for sorting colloidal particles in a microfluidic chip will be demonstrated, with applicability to cell sorting, and in Section 4.3 where a chip-integrated photonic crystal fibre is used for optical chromatography.

The field of cell sorting is a diverse one, with areas of maturity such as fluorescence- and magnetic- activated cell sorters (FACS, MACS) but also one that has received continued and ever increasing interest since conception in 1972 [79] due to its increasing pertinence in a wide range of clinical and biological applications [80]. This section will first review the motivations for sorting microscopic particles, particularly biological cells and with focus towards microfluidic techniques, before describing some common and more obscure non-optical methods for fractionation, followed by a review of active and passive optical methods. Note that a distinction is made between flow cytometry and for instance FACS, where the latter adds sorting/fractionation functionality to the former.

1.4.1 Motivation for the Fractionation of Particles within Microfluidic Platforms

A recent review [80] listed twenty five key applications of flow cytometry, the majority of which are in clinical applications including the harvesting of stem cells, monitoring the progression of HIV, immunophenotyping and assessment of sperm quality; but also many in the wider biological sciences and research. Many of these applications require not only the counting of specific sub-populations within a sample, but also the separation and collection of these cells for further use, in a sterile manner and with minimal damage.

The trends in flow cytometry have been towards higher throughput, increased detection variables, with current fluorescent-activated sorting systems capable of 10^5 cells per second and for anything up to 16 measureable parameters [80]. The devices remain however, as expensive, complicated benchtop instruments, often requiring a specialist operator, utilising modest sample volumes that need to be brought to the machine, wherever it happens to be located; all of which are barriers inhibiting more widespread use.

The idea of sterile, cheap, portable, disposable fluidic chips or cartridges, that utilise small sample volumes for point of care analysis, diagnosis, or sample purification is as appealing as ever. Other advantages of sorting within microfluidic environments include increased particle control due to the removal of turbulence and laminar for such low Reynolds number systems, and the facility to work with small numbers of particles, which is of particular importance for separating out rare cells [6].

1.4.2 Fractionation by Non-Optical Techniques

Some of the more prominent sorting techniques, all of which have been applied in microfluidic environments are described below, although this is not intended to be a fully comprehensive list. A review by Pamme [81] details some of these in more detail and lists some of the more obscure fractionation methods with a focus on LOC implementations, as does Huh *et al.* [82].

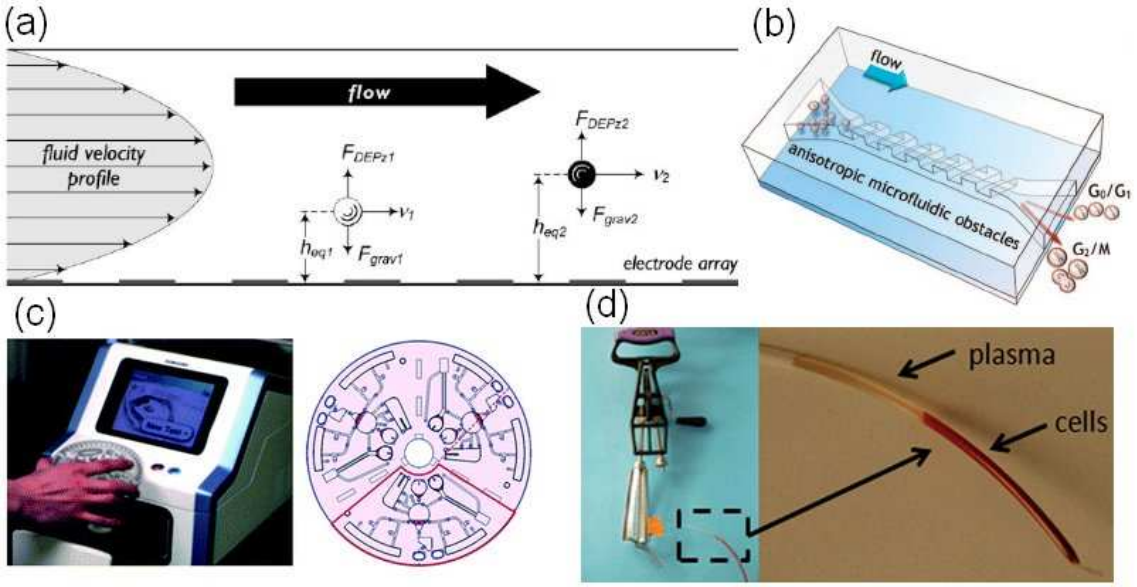

Figure 1.8: *Examples of non-optical sorting schemes. (a) Field-flow-fractionation where in this example, dielectrophoresis is used to position sub-populations into different heights in a parabolic shaped fluid velocity profile, thus separating in time their passage through a downstream detector* [83]. *(b) In-channel structures have particle-dependent effects on the flow through hydrophoretic chips, allowing sorting by size* [84]. *(c) High-tech and (d) low-tech examples of centrifugation devices, the first being a lab-on-a-compact-disc centrifugal-driven analysis system* [85]*, the second being an adapted egg whisk for blood separations in developing nations* [86].

1.4.2.1 Sorting by Centrifugation

The most common sorting method of all, the centrifuge, is an item found in every common biology laboratory. Spinning a sample at a high angular velocity generates a large centrifugal force, compacting suspended particles into a pellet at the bottom of the sample tube. This is useful in itself, for separating particles from the aqueous phase, such as cells from a culture medium. Differences in size and density in the particles in the sample can produce different bands in the sample, allowing them to be carefully separated using a pipette. It only works if the particles of interest are abundant in the sample, if they are very different in size or density to the other unwanted medium or particles, and if the bands are clear enough to see by eye or under a microscope.

High rotational speeds can compromise the particles, which was observed in early work in preparing the cells for the photoporation experiment in Chapter 6, where 30 % of the cells were observed to have died before even reaching the optics laboratory

due to centrifugation (as confirmed with propidium iodide, 1.2 RCF, HL60 cells). It is however a very accessible technique, never more pronounced than the report by the Whitesides group of the use of an adapted egg whisk for cell separations (plasma separated from whole blood), with particular application for the developing world [86]. There has been continued interest in utilising centrifugal forces in compact-disc type microfluidic cartridges, but with minimal sorting demonstrated to date other than fluid removal from particle suspensions [85].

1.4.2.2 Magnetic-Activated Cell Sorting (MACS)

MACS is a well established technique, particularly in immunology, for separating out a single cell type [87]. Prior to the separation process, the cells are incubated with antibody-coated paramagnetic microbeads. This permits preferential attachment of the beads to the cells of interest through antibody-antigen binding, thus allowing the cells to be physically separated out using an external magnetic field. This technique is only applicable to selecting cells by surface markers and is reliant upon suitable antigens on the cell surface allowing the paramagnetic beads to accurately bind to or "tag" the cells of interest. Furthermore, the number of paramagnetic tags that can be used in parallel is more limited than for fluorescent tags in FACS. MACS can be often utilised as a pre-enrichment step for other use in other sorting techniques [80]. There have been a handful of sorting directed LOC magnetic systems, still in proof of principle stage [88] whilst an integrated CMOS microfluidic system has been demonstrated for magnetically-tagged single cell trapping and manipulation [89].

1.4.2.3 Field-Flow Fractionation (FFF)

Field flow fractionation [90] is a sorting technique similar in concept to gas chromatography (but lacking a stationary phase) but applicable to microparticles, being successfully applied to bacteria, viruses, yeast and mammalian cells [91]. The sample fluid is passed through a microfluidic channel and the sample analytes differing in mass, size or other physical properties are driven by an applied field (e.g. dielectrophoresis [83,92]) into different velocity regions within the parabolic flow profile of the flow channel (see Section 2.2). The analytes are then carried downstream through

the channel at different speeds, and exit the channel after different "retention" times. This is a batch separation technique, not capable of providing continuous separation of particles.

1.4.2.4 Hydrophoretic Fractionation

Hydrophoresis is the movement of particles suspended in a fluid due to the incorporation of microstructures, inducing position-varying hydrostatic pressure fields [93]. Typical geometries include slanted ridges or grooves in one or more of the channel walls, inducing rotational fluid flow, anisotropic flow resistances, and the formation of different flow paths in response to these flow patterns, according to particle size or density [93]. Demonstrations include colloidal separations with a resolution of 0.1 μm [37], mammalian cells according to cell cycle phase [84], DNA according to base-pairs with 6% resolution for 15-35 kilobases [94], and a 210-fold enrichment in white blood cells in whole blood [93]. Other hydrodynamic sorting mechanisms exist without periodic microstructures, instead utilising the exposure of different sized particles to varying fluid velocities or shears near the presence of a channel boundary [95].

1.4.2.5 Dielectrophoretic Fractionation

Dielectrophoresis (DEP) induces a force on an uncharged polarisable dielectric particle, suspended in an electrolyte, when placed in a non-uniform, normally AC, electric field [96, 97]. Two regimes exist, positive dielectrophoresis where the induced dipole moment is larger than that of the fluid, causing the particles to move towards the region of highest electric field density, and negative dielectrophoresis where the particles move away from the field [96]. The strength and sign of the force is dependent upon the cube of the particle radius and on its frequency-dependent polarisability, thus by changing the AC frequency, the attraction or repulsion of different species of particles can be controlled [96]. Various implementations have been demonstrated in microfluidic formats, including the trapping of biological cells [98–101], the fractionation of blood cells [102], bacteria [103] and the isolation of cancerous cells from blood [92]. The requirement for an inherent difference in

DEP response between target and non-target cells is present here just as in other passive sorting techniques, which equally can be overcome [103, 104] by the inclusion of dielectric tagging through suitable surface binding, as also demonstrated in passive optical sorting [6, 105].

1.4.3 Active Sorting using Optical Forces

As seen in Section 1.2, optical forces offer the capability to exert sizable forces on microscopic particles, capable of immobilising and positioning at will cells and colloids within fluid flow streams. Further absorption can be minimised, preventing detrimental effects and, as such, optical traps and tweezers offer a means for controlling cellular samples without physical contact. Gradient and scattering forces clearly therefore have much further applicability than to just trapping and force measurements, with optically-mediated fractionation being one of these, where the role of optics can play one or more of the necessary functions for a complete sorting device.

Optical sorting can be divided into two distinct types, active and passive. In active sorting, particles are selectively tagged with markers prior to the sorting process, making use of chemical or biological techniques, such as antibody-antigen binding [106] to distinguish and selectively attach to the desired sub-population of interest. Commonly used markers include fluorescence tags as used in FACS, magnetic beads as used in MACS, and dielectric beads in optical sorting [6, 105], all of which have all been used within microfluidic sorting contexts. Active sorting also includes techniques, such as in the case of RACS (Raman-activated cell sorter) [107] where particles are interrogated first, then fractionated accordingly, making it an active technique despite the lack of tags. Passive sorting (see Section 1.4.4) however, purely relies on the intrinsic response of the particle to a force due to its optical and hydrodynamic properties, such as shape, size, and refractive index. As a result, passive sorting does not require a tagging step or prior information on each and every particle. Here the focus is on demonstrations that use optical forces in the fractionation processes.

1.4.3.1 Fluorescence-Activated Cell Sorting (FACS)

The FACS is a well established and powerful active cell sorter, capable of sorting up to 40,000 cells per second [80], the workings of which are summarised in Figure 1.9. The cells or particles are placed into suspension and injected into a *sheath* fluid flow stream, within an acoustically-driven vibrating nozzle. The cells flow single file through a detection region where they are interrogated according to anything up to 16 fluorescence and scattering parameters [80], which may be placed at multiple angles for additional size-dependence information. The cells may be tagged with fluorescent probes that may be intracellular such as fluorescent proteins for staining of organelles or indicative of cell functionality [82], or by attaching external fluorescent beads through antibody-antigen binding. The vibrating nozzle causes the formation of droplets, which after rapid data processing are individually addressed using an electrical charge to direct them to the appropriate collection vials. The most common applications are in analyses for cell surface antigen expression, cell physiology (e.g. free Ca^{2+} or pH), apoptosis, cytokine expression and DNA content [108].

A number of implementations of FACS systems have been demonstrated in microfluidic chips, the first of which was Fu *et al.*'s report in 1999 [109] on sorting fluorescent beads and E. coli bacteria at a rate of 10 particles per second. Of particular relevance are Wang *et al.*'s [18] and Perroud *et al.*'s [110] microfluidic FACS ($\mu FACS$) systems that utilise optical tweezers as the sorting switch, greatly simplifying the chip in this micrometre interpretation. In the Wang study, cells were hydrodynamically focused into a linear flow through a detection and subsequent deflection region. This active cell sorter used two lasers; one at 488 nm to excite GFP in cells, and a near-infrared laser operating at 1070 nm as an optical switch that deflects the selected cells into the appropriate stream at a Y-junction in the chamber. The presence of the desired cell type is indicated by the fluorescence signal recorded upon a photomultiplier. Cell viability and membrane integrity were explored and studied using a trypan blue exclusion test, along with additional testing for heat shock and shear stress through the expression of indicator genes. Various non-optically switched $\mu FACS$ have also been reported [111–114], some of which

are reviewed in Andersson *et al.* [115].

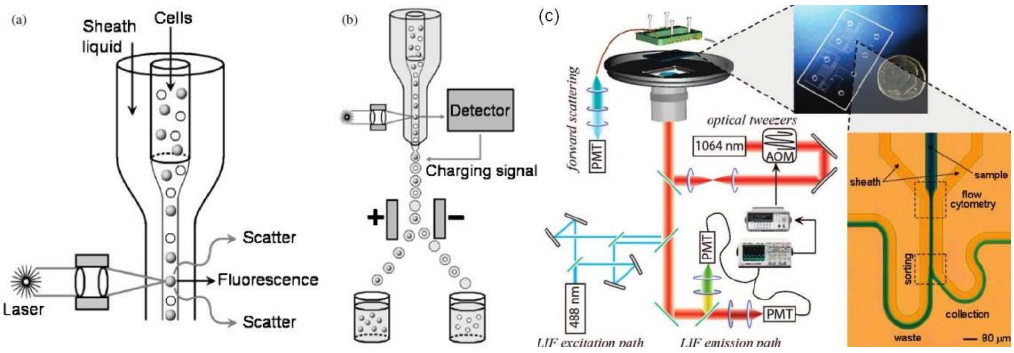

Figure 1.9: *The basic functionality of a fluorescence-activated cell sorter. (a) The cells are forced into single file flow by the sheath fluid and excited with numerous laser sources for fluorescence and scatter generation.* [82] *(b) Acoustic actuation of the fluid nozzle forces droplet formation of the cell sample. Fast acquisition and processing of the data allows* in situ *electrical charging of droplets according to their contents and are directed to the appropriate collection vial accordingly. Modern FACS devices are capable of sorting tens of thousands of cells per second.* [82] *(c) An example of a microfluidic FACS system, where forward scattering and fluorescence can be employed to distinguish particles in a hydrodynamic focused flow in a microfluidic chip. An optical tweezers beam is used to deflect particles between one of two output flows according to the obtained signal.* [110]

1.4.3.2 Raman-Activated Cell Sorting (RACS)

Unlike $\mu FACS$ where the miniaturisation process produces a significant reduction in throughput, Raman-activated sorting techniques are unique in that the acquisition time for non-resonant Stokes Raman spectroscopy is sufficiently long (typically 10's of seconds to minutes) that a microfluidic delivery of cells is necessary to maintain such a slow fluid flow. RACS therefore only is a microfluidic technique, at least so far, but perhaps using surface-enhanced Raman scattering (SERS) [116, 117] or fluorescence suppression techniques [118] throughput could be improved for more macroscopic implementations. Lau *et al.* [107] reported a RACS system, that utilised the Raman excitation beam simultaneously as optical tweezers (Raman tweezers) to move a cell out of the main fluid flow, acquire a signal and then release it into the laminar flow stream towards the appropriate collection chamber. A number of Raman/CARS microfluidic cytometry systems have also been reported [119, 120].

1.4.4 Passive Optical Sorting Techniques

Optical passive sorting, is a technique that relies on the intrinsic optical properties of a particle, such as its refractive index, shape and size, to cause one species of particle to behave differently in the response to a given optical landscape to that of another. A particle of higher refractive index will require a stronger external force to overcome the gradient forces of a trap for instance; or optical fringes of the width of one particle diameter will be unlikely to withold particles of diameters twice the fringe spacing. Unlike active sorting techniques, passive sorting does not require the particles to be tagged in any way, and no prior knowledge of the particle is required for fractionation to occur. The incorporation of dielectric particles, through preferential antigen-antibody surface attachment or phagocytosis, enables the enhancement of optical differences in situations where significance does not otherwise exist, turning a passive sorting technique into an active sorting process.

1.4.4.1 Static Passive Optical Sorting

In static passive sorting, no fluid flow is required, with the effect been driven purely by optical forces. Ricárdez-Vargas *et al.* [124] demonstrated the use of a moving 1D interference pattern, producing an array of optical line traps, that could shunt particles in two directions. By tuning the fringe spacing, size dependence could be introduced to allow translation of only particles below a given threshold, and by tuning the optical power the translated fringe pattern would only be effective on particles of high refractive index. Čižmár *et al.* [66] extended the ideas, making use of a tilted washboard potential (i.e. a tilted fringe pattern produced by a power mismatch in the two interfering beams) in the Kretchmann near-field geometry (see Section 1.3.2.1), allowing different particles to be simultaneously translated in opposite directions (see Figure 1.10a). Paterson *et al. [121]* applied static sorting to several biological cell types, including blood cells (see Figure 1.10b), and to mixtures of normal and cancerous cells, bone-marrow cells and stem cells, whose refractive indices were enhanced through preferential dielectric tagging [6].

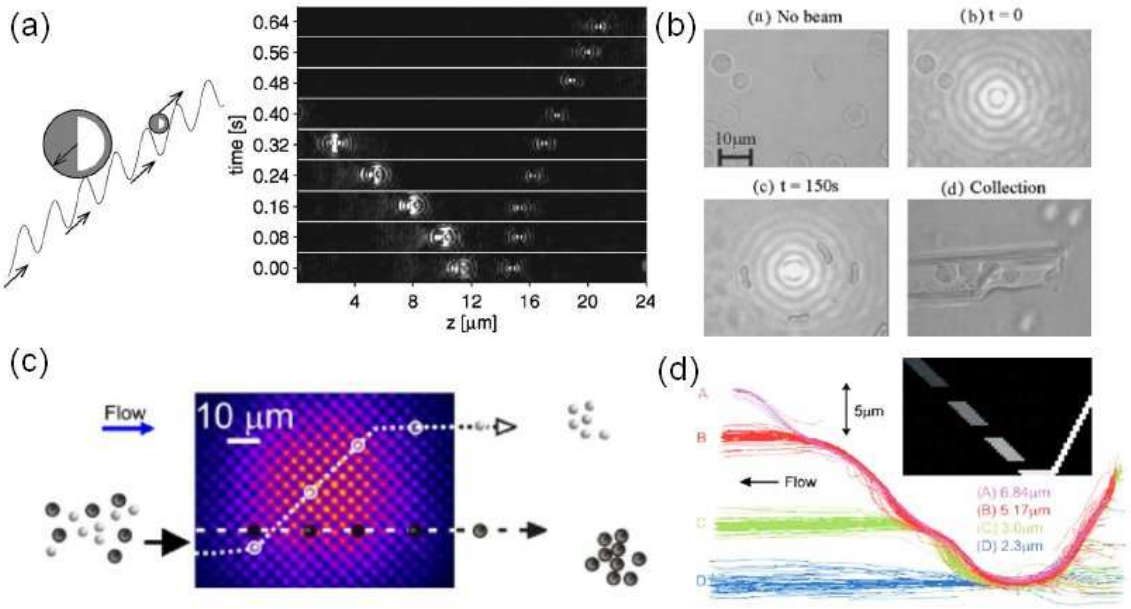

Figure 1.10: *Examples of the use of optical potential energy landscapes for passive sorting microscopic particles based on differences in their intrinsic optical properties. (a) Moving tilted washboard interference pattern allows the translation of particles of different sizes in opposite directions. The larger particles sit across two fringes and bounce their way down the the overall tilted potential, whereas the smaller particles are trapped in and translated by the moving fringes* [66]. *(b) The concentric rings of a static Bessel beam trap RBCs due to their concave shape, whereas the larger more spherical lymphocytes lie across multiple rings and thus make it to the most intense central core of the beam, where they are guided to the top of the sample chamber. Collection then can occur using a micro-capillary tube* [121]. *(c) Used in combination with a moving sample stage or microfluidic flow, optical lattices, such as this body-centred tetragonal formed from five interfering beams, may be used to spatially separate particles as they traverse the optical landscape* [6, 122]. *(d) The use of an AOD or SLM may be used to produce customised and dynamic optical landscapes. Here, an AOD raster-scans four potential energy wells (inset), with reducing intensities, such that different sized particles escape the optical field at different points* [123].

1.4.4.2 Optical Chromatography

In Section 4.3, the integration of photonic crystal fibre into PDMS microfluidic chips will be discussed for applications in optical chromatography, a distinct category of passive optical sorting. As first reported by T. Imasaka *et al.* in 1995 [126], optical chromatography was demonstrated to be capable of fractionating dielectric particles by size, and later by refractive index [127] and by hydrodynamic profile (predominantly shape) [128]. In this first experiment, a dielectric particle was introduced into a capillary tube by a laminar liquid flow. A lightly focused counter-propagating free-space laser beam was aligned parallel to this fluid flow. The optical gradient forces

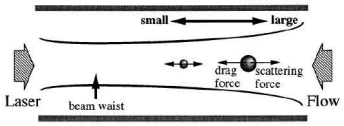

Figure 1.11: *The basic sorting scheme of optical chromatography, where the balance of the Stokes fluid drag force and the optical scattering force forms increased retention distances (or equilibrium distances) for larger particles or those with higher refractive indices.* [125]

trapped the particle along the centre of the laser beam and accelerated it against the fluid flow, away from the beam waist due to the radiation pressure. Counter to this, the Stokes fluid drag force decelerated the particle until finding an equilibrium position where the fluid drag force and radiation force balanced. The distance between the equilibrium position and the beam waist was termed the *retention distance* and is dependent upon the intrinsic optical and hydrodynamic properties of the particle. The retention distance is also a function of the laser power and fluid flow rate [9, 129].

A later paper [129] demonstrated the first biological applications of optical chromatography, where human erythrocytes were shown to be split into two subpopulations using the technique. The potential of optical chromatography as a biological tool was thoroughly embedded through another paper by the group, where the technique was applied to immunoassay of protein [106]. Polymer beads coated in antibody (anti-mouse IgG) were flowed into the optical chromatography setup and the retention distance was observed. A concentration of antigen (mouse IgG) was then flowed in, generating bead-bead binding through the presence of the antigen. Bound coagulated beads exhibited an increased radiation pressure thus receiving an increase in retention distance by up to 500 µm compared to the unbound free beads. The ratio of free to bound beads was calculated providing a reaction probability, and protein concentration of 10's $ng\,mL^{-1}$ could readily be measured. The reversibility of the reaction in real time was also investigated by monitoring the exchange to and from the bound and unbound as visualised on camera. As such, optical chromatography provided the capability to study for the first time a single bond reversible reaction, as well as the capacity to watch the reaction in real time. A follow-up paper [130] improved the sensitivity of the experiment down to 1 $ng\,mL^{-1}$ by altering the bead size, and provided an investigation into the role of antigen concentration

in dissociation.

As well as supplying a means of separating particles according to retention distances dependent upon particle properties, optical chromatography has branched into three not so dissimilar approaches, namely the *optical funnel*, the *optical channel* and the *optical chromatography filter*. The various names are more of an indication of a different application rather than a change in experimental setup. The optical funnel is a technique for measuring the force a biological particle can exert to escape the gradient forces of the optical field within an optical chromatography setup. This was first applied to fresh water bacteria Trachelomonas volvocina [131] and later to sperm cells for varying medium pH [132] and allowed for large numbers (100's) of cells to be characterised in a few hours.

The optical channel is another variation on the optical chromatography for measuring the elasticity of a cell. Unlike the work on the dual-beam fibre trap optical stretcher by J. Guck and coworkers [133], here the fluid flow gives rise to the stretch of a trapped cell, rather than the optical field. Briefly, a flow of cells is flowed against a lightly diverging optical beam, which traps cells on axis. The cell is allowed to flow through the beam focus, at which point it elongates in one direction due to the fluid shear stresses, and the stretch is measured from a CCD image giving a one dimensional shear strength measurement of the cell. Here, erythrocyte shear strength was measured as a function of the age of the cell [134].

The most recent variation on optical chromatography is the optical filter, which is the result of developments from S.J. Hart, A.V. Terray and coworkers in the field of optical chromatography. The first paper on optical chromatography published by this group demonstrated sorting by refractive index [127]. Separations of several hundred of microns were exhibited for a polydisperse sample of silica, PMMA and polystyrene spheres. This was followed by the exciting report of the separation of the etiological agent of the mammalian disease anthrax, Bacillus anthracis bacteria, from both its spore and from the common environmental interferent, pollen. The separation of mulberry and ragweed pollen was also demonstrated. The publication was of utmost interest to the biodefense area as B. Anthracis is a common biological warfare threat. In another publication a distinct optical chromatographic separa-

tion between B. Anthracis and its close relative B. Thuringiensis was reported [128], caused by a combination of subtle differences in their morphologies. On close inspection, B. Thuringiensis was observed to be more of an oblate spheroid in shape and also exhibited a larger exosporium, giving rise to changes in both the hydrodynamic and optical forces involved.

Using fluid channels of varying dimensions allows for specific separation of species to be enhanced [135]. S.J. Hart, A.V. Terray and coworkers used customised PDMS chips with varying channel dimensions to enhance the optical chromatography separations, demonstrated on colloidal particles and spores of B. Anthracis and Mulberry pollen. The focusing lens was adjusted to move the beam waist and position the separation such that the two particles laid either side of a point where the channel width increased rapidly. The linear fluid flow is slower in a wider channel, hence sees a reduced Stokes fluid force and an increased retention distance compared to that in the narrower flow channel region. As a result, the retention distance of one species can be artificially increased to accentuate an already present difference in retention between two species.

In 2007 S.J. Hart, A.V. Terray and coworkers reported a new chip design and application that they termed an optical chromatographic filter [136]. Here, instead of holding two or more species at different retention distances, the laser and flow parameters are altered such that one species is held up and the others are allowed to flow through. The channel is made narrower and shorter, and the beam fills the entire channel ensuring that all particles feel the optical force. These adjustments evade the common issues with previous designs, where only a small fraction of particles are trapped by the beam, and allows for a large number to be held up without producing instabilities in the equilibrium positions due to re-scattering of the beam due to the particles. The new setup allows for separations of particles, or as demonstrated with B. Anthracis, a sample can be enriched to produce a more concentrated pure sample. The technique represents a more robust experimental setup, capable of dealing with much higher number of particles, as demonstrated in their later publication where separation efficiencies of 99% were achieved for thousands of polymer and silica particles compared to tens in previous setups. The

particle trajectories in an optical chromatography filter setup has also been modelled [137], using a finite element method for solving the Navier-Stokes equations and a ray optics model for the optical field.

1.4.4.3 Optical Lattices

Extending the idea of using interference patterns for optical sorting and taking the technique towards continuous fractionation, MacDonald *et al.* [122, 138] demonstrated the use of diffractive optical elements (DOE) to create optical landscapes produced by interfering anything up to five beams, producing 2D or 3D lattices of lines or spots (optical lattice), as shown in Figure 1.10c. A moving sample stage or microfluidic chip was utilised to flow particles through the optical landscape, allowing the fractionation of particles by size or refractive index, with up to 96 % efficiency and for 25 particles per second (slightly higher than for μFACS reports at the time) at flow rates of 35 $\mu m s^{-1}$. Attachment of dielectric tags for active sorting has also been demonstrated with the optical lattice, through functionalisation of dielectric spheres with anti-CD33 for specific attachment to HL60 cells [6].

1.4.4.4 Dynamic Optical Landscapes

Dynamic optical landscapes make use of a spatial light modulator (SLM) or an acousto-optic deflector (AOD, or acousto-optic modulator, AOM) to create a customisable potential energy landscape within a sample. The uses of such devices far outreach just optical sorting. The AOD is based on the Bragg diffraction effect, where an acoustic wave induces a sinusoidal modulation in pressure across an optically-transparent crystal, manifesting as a periodic refractive index modulation and thus is equivalent to a diffraction grating. By tuning the acoustic wave frequency, the spacing of the diffraction fringes can be tuned, and can be applied in both up-down and left-right directions, hence an AOD allows full angular control of a laser beam. As part of an optical tweezers system, an AOD can be placed at the conjugate plane to the steering mirror (and the objective back aperture), allowing the tweezers beam to be dynamically steering around a sample by computer control. The power of this approach is realised when one considers that AODs can

be switched at tens of kHz, i.e. faster than the Brownian fluctuations of the particle (see Figure 1.5b), enabling the laser tweezers to be repositioned much faster than it takes a trap particle to notice the beam absence. This is useful for time-sharing a tweezers beam to create multiple trap sites, such as time-sharing between two points to create two trap sites [139], each with half the average power. However, the idea can be extended further to produce not just trap sites, but to map out arbitrary optical potential energy landscapes. Milne *et al.* [123] used this for purposes of optical sorting, where they were able to simultaneously fractionate four sizes of microparticles into spatially separated laminar flow streams at 30 $\mu m s^{-1}$, as shown in the particle tracking plot in Figure 1.10d.

The other method for producing a dynamic optical landscape is using an SLM. D. Grier's group have reported theoretical [140] and experimental [141] studies on the use of SLMs for generating lattices of optical potential wells for kinetically locked-in transportation of flowing colloidal particles. A recent study [142] focused on its use in optical fractionation where they reported excellent discrimination for size (Δd =10's nm) and refractive index (Δn =0.005) for diameter d =0.75 μm silica spheres.

1.5 Conclusion

Optical manipulation methods are pertinent to microfluidic systems for further lab-on-a-chip development. The two fields go hand-in-hand, with optical trapping adding functionality as part of a complete on-chip processes, and with microfluidics realising the true potential of optical methods.

This chapter reviewed the field of optical trapping in view of its relevance to microfluidic application, with particular focus on the more-readily integrateable dual-beam trap (as demonstrated in Chapter 4), but also on the use of single beam tweezers for transporting micrometre-sized objects within microfluidic environments and their use as sensitive force transducers. With a suitable choice in the wavelength [143], absorption can be minimised to remove photodamaging effects, making optical methods highly suitable for micromanipulating living cells.

Methods for inserting evanescent fields into chips for manipulating particles on surfaces were explored, guiding particles around chips, or trapping cells with sub-micron exposure depths. A simple adaption to an optical tweezers setup enables evanescent trapping on a standard microscope, which as characterised in Chapter 5 shows linear dependence on particle size and can be readily coupled with microfluidic sorting geometries.

The second half of the chapter reviewed existing fractionation methods, some of which are common place within every biology laboratory and some still proof of principle demonstrations. The use of optical forces for sorting was focused on, methods were distinguished into active and passive techniques, and a brief review of optical sorting was presented, serving as a background to the sorting results detailed in Chapters 4 and 5. Optical sorting provide methods for sensitive, continuous fractionation of microscope particles by their intrinsic optical properties, or with suitable dielectric tagging, based on the presence of specific surface markers.

Optical tweezers and FACS devices are becoming mature technologies, with many commercial examples of each. However, with drivers towards bringing trapping and sorting to lab-on-a-chip for the biomedical, pharmaceutical, environmental industries, many of the workings of such macroscopic devices are being re-evaluated. The research field of microfluidic optical manipulation is thus vibrant and diverse, with plenty of scope for the reviewed techniques to find niche applications through further development and trials.

The following chapter explores the fundamentals of fluid flow when it is scaled down to the microscopic dimensions of the particles accessible with optical trapping forces.

Chapter 2

Fluid Flow at the Micrometre Scale

In Chapter 1, the concepts of optical manipulation techniques with microfluidic sample management were introduced. This chapter introduces the topic of microfluidics, which as seen in the last chapter, can be used in parallel with optical manipulation techniques to further their applicability or functionality, such as for sample delivery, particle management, creating isolated trapping environments, and sorting particles based on their interaction with an optical potential energy landscape. Unlike size reductions in electronic circuitry, reducing fluid flow to the realms of microchip dimensions yields very different physical behaviour than that one is used to in our macroscopic experiences. The Reynolds number is low for microfluidic flows and they are said to be *laminar*, in that they are turbulent-free and reversible, with fluid streams and particles following very predictable deterministic parallel paths, with inertial effects entirely removed and mixing only through diffusion (as in Figure 2.1). This yields desirable effects in terms of precisely positioning fluid flow streams or particles within a flow, particularly in view of the combination of optical manipulation and microfluidics, as discussed in Chapter 1.

The chapter reviews the governing Navier-Stokes equation and introduces the Reynolds number that highlights irrelevance of inertia to microfluidic environments, giving rise to its unusual behaviour. The velocity profile of the tightly confined fluid within microfluidic channels is explained and plotted for the chips utilised in later

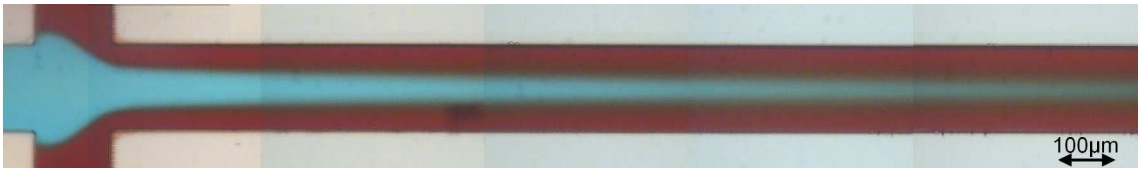

Figure 2.1: *Fluids will flow side by side without turbulence when the channel dimensions approach micrometre dimensions, characterised by a low Reynolds number and what is known as laminar flow. Here three dyes flow left to right, mixing only through diffusion.*

experimental chapters. The technique of hydrodynamic focusing is demonstrated and experimentally obtained results are compared to that predicted from theory. Finally, the force implications on particles within microfluidic channels are considered, and the corrections to the standard Stokes drag equation are presented. The velocity of a cell falling towards a boundary is also considered, with implications for the work in Chapter 6.

2.1 Laminar Flow in Microfluidic Systems

2.1.1 Navier-Stokes Equations

The dynamics of an incompressible Newtonian fluid is described by the Navier-Stokes equation [144],

$$\rho\left[\frac{\partial \underline{\nu}}{\partial t} + (\underline{\nu}\cdot\nabla)\underline{\nu}\right] = -\nabla P + \mu\nabla^2\underline{\nu} + \underline{f} \tag{2.1}$$

where ρ is the fluid density, $\underline{\nu}$ is the fluid velocity, P is the pressure, μ is the fluid viscosity and $\underline{f}$ are any additional external force densities [145]. The equation is in effect Newton's second law, with the forces per unit volume on the right hand side, due to a pressure gradient $-\nabla P$ and viscosity $\mu\nabla^2\underline{\nu}$, and on the left the density (mass per unit volume) multiplied by an acceleration expression. Importantly for fluid flows restricted to micrometre dimensions (microfluidic), with no additional external forces, it can be shown [146] that equation 2.1 can be greatly simplified by considering the negligible influence of the inertial left hand side of the equation,

leaving the Stokes equation [144, 147]

$$\nabla P = \mu \nabla^2 \underline{\nu} \tag{2.2}$$

which is the laminar flow version of the Navier Stokes equation. The validity of this assumption can be conveniently exemplified by the Reynolds number.

2.1.2 Reynolds Number

The Reynolds number is a dimensionless value representing the ratio of inertial to viscous forces in a fluid system. It can be shown that [146]

$$Re = \frac{inertial\ forces}{viscous\ forces} = \frac{\rho U_0 L_0}{\mu} \tag{2.3}$$

where U_0 and L_0 are the characteristic velocity and length scales of a contained fluid. For the syringe pump driven experimental setups described in later chapters, U_0 is the average flow velocity $\hat{\nu}$ as given by

$$U_0 = \hat{\nu} = \frac{Q}{hw} \tag{2.4}$$

where Q is the volumetric flow rate (volume per unit time) as determined by the syringe pump, h and w are the height and width of the flow channel cross-section respectively. The characteristic length scale for flow in a rectangular channel is given by [148, 149]

$$L_0 = \frac{2}{\frac{1}{h} + \frac{1}{w}} \tag{2.5}$$

Calculating the Reynolds number for typical parameters of $U_0 = 100\ \mu m s^{-1}$, $L_0 = 100\ \mu m$ and a density and viscosity of water, produces $Re = 0.01$, i.e. much less than unity. Thus, even for an increase of an order of magnitude of the velocity or the length scale, the viscosity is by far the dominating term in equation 2.1 and inertial effects can be excluded, producing regular, linear and deterministic flow as predictable by equation 2.2. A visual example of laminar flow can be seen in Figure 2.1, where three fluids are flowed along side by side, with the gradual blurring of the

colours only due to progressive diffusion rather than any turbulence-driven mixing. For details on the other insightful dimensionless microfluidic parameters such as the capillary and Dean number, Squires *et al.* [145] is highly recommended.

2.2 Poiseuille Flow Profile

The reduction of the nonlinear partial differential Navier-Stokes equation 2.1 to the linear Stokes equation 2.2 means the fluid flow in microfluidic systems can be easily predicted, without resorting to numerical techniques. Taking Equation 2.2 and assuming non-slip boundary conditions, it can be shown that the fluid flow in a rectangular microfluidic channel can be determined by [144, 150]

$$\nu(x,y) = \frac{4h^2}{\mu\pi^3}\left(-\frac{dP}{dz}\right)\sum_{\ell=0}^{\infty}\frac{(-1)^\ell}{(2\ell+1)^3}\left\{1-\frac{cosh\left[(2\ell+1)\,\frac{\pi x}{h}\right]}{cosh\left[(2\ell+1)\,\frac{\pi w}{2h}\right]}\right\}cos\left[(2\ell+1)\,\frac{\pi y}{h}\right] \tag{2.6}$$

or averaging in one of the planes, the mean velocity is

$$\hat{\nu}(x) = \frac{8h^2}{\mu\pi^4}\left(-\frac{dP}{dz}\right)\sum_{\ell=0}^{\infty}\frac{1}{(2\ell+1)^4}\left\{1-\frac{cosh\left[(2\ell+1)\,\frac{\pi x}{h}\right]}{cosh\left[(2\ell+1)\,\frac{\pi w}{2h}\right]}\right\} \tag{2.7}$$

where ν is the fluid flow velocity in the z direction along the channel, as a function of position x and y in a channel of width w and height h respectively. dP/dz is the pressure drop with distance down the channel which can be assumed to be constant, ℓ is an integer and μ is the fluid viscosity.

Figure 2.2 shows the result of plotting 2.7 for the channel dimensions and flow speed utilised in Chapter 6, showing a typical Poiseuille parabolic-shaped flow profile. The channel dimensions in that case are $w = 150\ \mu m$ and $h = 70\ \mu m$, i.e. a ratio $\epsilon = h/w = 0.47$. The shape of the flow profile depends upon this ratio of the channel width to height, and tends towards a flatter, more *plug*-like velocity profile (Hele-Shaw geometry) for extreme values ($\epsilon \to 0,\ \infty$ i.e. flow between two infinite flat plates) and the transition is explored fully in [144, 150]. An entirely flat velocity profile can be obtained by using non-pressure driven flows, removing the stationary

boundary condition, such as electrokinetic-driven fluid flow [145] .

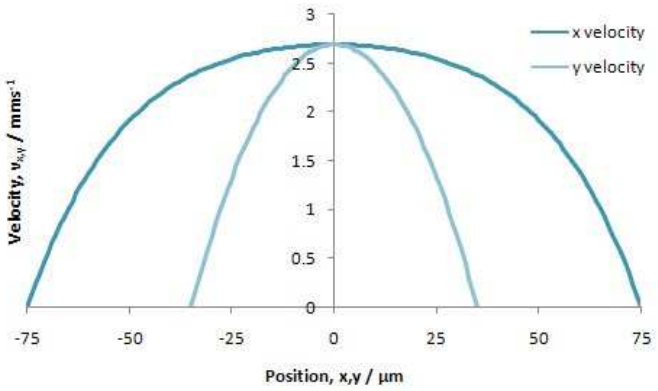

Figure 2.2: *Poiseuille parabolic fluid velocity flow profile as a function of* x *and* y *in the microfluidic channel utilised in chapters 5 and 6, assuming an incompressible fluid with non-slip boundary conditions. Channel dimensions are a width of 150 µm and height of 70 µm (i.e.* $\epsilon = 0.47$*), with a flow rate of 77* $\mu l\, hr^{-1}$*. Velocities plotted are* $\nu_{x,\, y=0}$ *and* $\nu_{x=0,\, y}$*.*

2.3 Hydrodynamic Focusing

After reviewing the velocity profiles in a pressure driven Poiseuille flow, it is apparent that any particle suspended within microfluid flow can travel at a large range of velocities. For delivering particles to an optical beam for sorting, trapping, photoporation etc. it is desirable to firstly have all particles follow similar paths within the fluid, such that they all enter the beam at the same location, and they do this with similar velocities. One method could be to use fluid channels that are similarly sized to the particles themselves, but in practice this is normally prohibited due to the particles attaching to the channel walls, blocking the path of further particle flow. The second option is the use of a positioning technique to place all particles within the same laminar flow stream. There are a number of methods for achieving this, including electrokinetic and optical techniques, however the method utilised in this thesis along with numerous other works is hydrodynamic focusing. [18, 107, 110, 151, 152]

Hydrodynamic focusing is the use of two *buffer* fluid streams to squeeze and thus narrow a third stream, containing the sample, down the centre of a flow channel. By controlling the relative flow rates of the three fluids, the central sample flow can be squeezed to a width as required, or translocated from side to side. This allows the

positioning of the sample fluid into a restricted range in the Poiseuille flow profile, at least in one dimension. Figure 2.3 shows the hydrodynamic focusing of a dye between two flows of DIH_2O, for varying ratios of the buffer and sample flows.

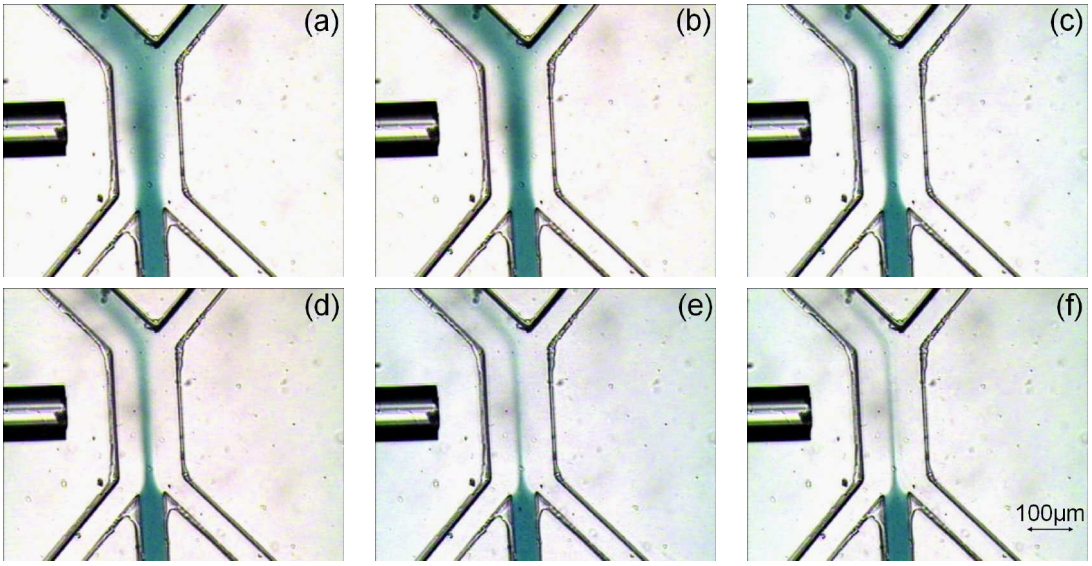

Figure 2.3: *Hydrodynamic focusing in a PDMS microfluidic chip. Flow is upwards in the images, for flow ratios of (a) 1:1:1 (b) 2:1:2 (c) 4:1:4 (d) 8:1:8 (e) 16:1:16 (f) 32:1:32 of the three respective input channels (widths 50 µm). Here, blue food colouring is focused by two buffer water flows. The outlet channels are missmatched (100 µm, 50 µm) in width such that if sufficiently narrowed, all the dye flows to the left hand outlet. The central channel region is 300 µm in length and 150 µm wide. On the left is an integrated optical fibre that is not in use in this demonstration.*

The width of the focused flow stream can be theoretically determined, and Lee *et al.* [150] derived the following equations for this purpose

$$w_f = \frac{w}{\gamma(1+\alpha)} \tag{2.8}$$

where w_f is the width of the focused sample stream in a channel of width w and height h, and $\alpha = \frac{Q_s+Q_b}{w\times h}$ with $Q_{s,b}$ being the volumetric flow rates of the sample and each of the buffer streams. γ is to be determined simultaneously with w_f as defined by

$$\gamma = \frac{\hat{\nu_f}}{\hat{\nu_o}} = \frac{1 - \left(\frac{192h}{\pi^5 w_f}\right)\sum_{\ell=0}^{\infty}\frac{1}{(2n+1)^5}\frac{sinh\left[(2\ell+1)\pi w_f/2h\right]}{cosh[(2\ell+1)\pi w/2h]}}{1 - \left(\frac{192h}{\pi^5 w}\right)\sum_{\ell=0}^{\infty}\frac{tanh[(2\ell+1)\pi w/2h]}{(2\ell+1)^5}} \tag{2.9}$$

where $\hat{\nu}_{f,o}$ are the mean velocities of the focused stream and the overall output

stream respectively. The widths of the focused streams in Figure 2.3 were measured and are plotted along with the theoretically predicted values in Figure 2.4, showing excellent agreement.

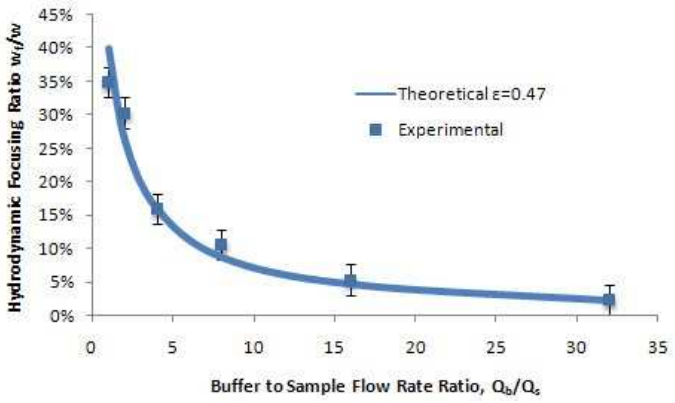

Figure 2.4: *Experimental and theoretical determinations of the relative reduction in sample fluid width by the use of hydrodynamic focusing, for different ratios of sample and buffer flow rates, for the chip dimensions utilised in Chapters 5 and 6.*

Focusing a sample in a second dimension, so as to restrict its position in both x and y position, is indeed also possible. There is a discrepancy in the literature as to whether to call this 2D or 3D hydrodynamic focusing, arising from the requirement for three dimensional microfluidic structures to be fabricated in order to restrict a sample in two dimensions [153]. 3D hydrodynamic focusing strictly is containing a sample within a spheroid or similar shape, surrounded and contained using a buffer fluid. The closest example of this is by Lin *et al.* [154] where particles are contained within a "hydrodynamic vortex trap", where a recirculation of the fluid occurs in close proximity to a sudden expansion in the channel width. There are a number of different designs in the literature for obtaining 2D hydrodynamic focusing [153–158]. An interesting design makes use of chevron shaped structures on the top and bottom of the channel after a 1D hydrodynamic focusing junction, which acts to pull the buffer streams in on top and from below the sample, thus restricting it in the vertical plane as well.

2D hydrodynamic focusing was not employed for any of the experimental chapters. Many fabrication challenges were found in creating 3D structures within PDMS, particularly with the two restrictions of maintaining the coverslip as the base of channel, and having the sample focused within 50 μm of the coverslip for

access with a high NA objective lens. It could of be of utmost interest to future studies, particularly in optical sorting or photoporation (see Chapter 6) for improved precision in delivering particles to optical beams.

2.4 Diffusion & the Péclet Number

With inertial effects removed, the chaotic turbulent mixing and thermal convection of our high Reynolds environment is non-existent in microfluidic devices. Laminar flow of fluids leaves only diffusion as a means for mixing fluids, proving advantageous in some applications but forcing complete redesign of what were simple macroscopic processes [145]. These effects are of particular importance to on-chip chemistry, where for a reaction to occur between two reagents, there must be intimate contact between the interacting molecules, occurring only through the diffusion across the constituent fluid boundary. The degree of mixing of reagents is of direct impact on the yield of the reaction, thus many methods for wrapping fluids or increasing surface areas between the reagents have been developed [145, 159], including the use of extreme hydrodynamic focusing. Conducting reactions in microfluidic configurations for rapid diffusion allows precise, homogeneous mixing of reagents, thus improved yields and levels of control in reactions can be expected from these systems [117,160]. At the other end of the process, the reliance on turbulence forces new methods of separation of post-reaction products, with optical sorting techniques being of relevance to fractionating off colloidal particulates (such as those reviewed in Section 1.4 and detailed in Chapter 5 and Section 4.3).

The Péclet number, Pe gives a good indication of the diffusive mixing within microflows [145]

$$Pe \equiv \frac{U_0 w}{D} \sim \frac{Z}{w} \tag{2.10}$$

defined as the distance, Z (expressed in the number of channel widths, w) a fluid must flow before complete mixing of an introduced substance with diffusion coefficient D, at a fluid velocity U_0.

This becomes important in Chapter 6 when considering photoporation of large

molecules such as plasmid DNA. The diffusion coefficient for 4.7-5.2 kilobase DsRed or GFP of the order of 100 nm in length, is approximately 2 $\mu m^2 s^{-1}$ [145, 161], and for $w = 100\ \mu m$ with $U_0 = 77\ \mu l\, hr^{-1}$ one obtains $Pe = 11,000$, i.e. complete mixing will not occur for 11 m. Until on-chip mixing is addressed in this system, plasmid DNA would have to be introduced into the entire fluid piping with prior mixing, increasing the consuption at least 100-fold compared to if it could be inserted directly on-chip along with the cells.

2.5 Stokes Drag Force & Hydrodynamic Correction Factors

The force exerted on a sphere by a moving fluid, or likewise a sphere moving through a stationary fluid, is known as the Stokes drag force [146]

$$F_{drag} = 6\pi\mu a\nu \tag{2.11}$$

where a is the radius of the sphere, ν is the fluid velocity and μ is its viscosity. The value of this resistive force is necessary for inferring the forces exerted on a particle within a fluid due to an optical field, such as for the purposes of calculating the trap stiffness or Q-value measurements in an optical trap (Section 1.2.3) or calculating the expected velocity of a particle guided by an optical field (Section 5.6.1.2). Equation 2.11 is applicable to a single sphere in an infinite fluid, and is valid only in situations where the boundary effects of a nearby surface (within 10 radii), such as a channel wall, do not influence the effective viscosity of the fluid, which increases as the proximity to the boundary increases.

For distances of $h > 1.04a$, Goldman *et al.* [162] showed that the Faxén correction factor deviates less than 10%.

$$F_{Faxen} = \frac{6\pi\mu a\nu}{1 - \frac{9}{16}\frac{a}{h} + \frac{1}{8}\left(\frac{a}{h}\right)^3 - \frac{45}{256}\left(\frac{a}{h}\right)^4 - \frac{1}{16}\left(\frac{a}{h}\right)^5} \tag{2.12}$$

where h is the distance from the boundary. It is quite rare for the Faxén correction not to be applicable in an optical tweezers measurement. For even closer proximities

or when the particle is in contact with the substrate one can use the lubrication values of this correction [163] where, assuming the particle not to rotate, is

$$F_{Krishnan} = 6\pi\mu a\nu \left[\frac{8}{15} ln\left(\frac{h-a}{a}\right) - 0.9588\right] \tag{2.13}$$

Comparisons of the calculated velocities of optically guided particles using Stokes, Faxén and Krishnan calculated fluid drag forces are given in Table 5.2, for a particle optically trapped and guided across a surface using an evanescent wave.

2.6 Settling of Particles

The velocity of a falling sphere can easily be calculated by equating Stokes drag against the particle's gravitational weight. In a microfluidic environment however, the presence of a wall creates a lubricating layer that will increase the effective Stokes drag on the particle, and is particularly relevant when the particle is within ten times its radius from the surface (see Section 2.5) [164]. A corrected "settling" velocity v_{set}, at a distance y above a surface, can be approximated to [164]

$$v_{set} \approx \frac{v^0_{set}}{1 + \frac{a}{y-a}} \tag{2.14}$$

where $v^0_{set} = \frac{2}{9}(\rho_c - \rho_m)g\frac{a^2}{\mu}$ is the uncorrected Stokes velocity, for a particle with radius a and density ρ_c, in a fluid medium of density ρ_m and viscosity μ , under acceleration due to gravity g. This is calculated for typical values of a mammalian cell-sized sphere within water in Figure 2.5 ($a = 15\ \mu m$, $\rho_c = 1.1 \cdot 10^3\ kgm^{-3}$, $\rho_m = 0.998 \cdot 10^3\ kgm^{-3}$, $\mu = 1.003 \cdot 10^3\ Pa\,s$), demonstrating that a cell can be expected to fall at rate close to 10 μms^{-1} within typical microfluidic volumes. Integrating 2.14 reveals that it takes this model cell just 5.6 s to drop 50 μm to the channel floor, or in other words, a cell travelling at 100 μms^{-1} in a fluid flow will last just 18 μm before coming into contact with the floor (neglecting the counteracting effect of the Bernoulli effect that is not significant below 500 μms^{-1} [165], and the parabolic flow profile). This was of particular relevance for designing the chip for Chapter 6 where reservoirs were incorporated onto the chip that hinged on the

reliance of gravity for cell insertion and later collection.

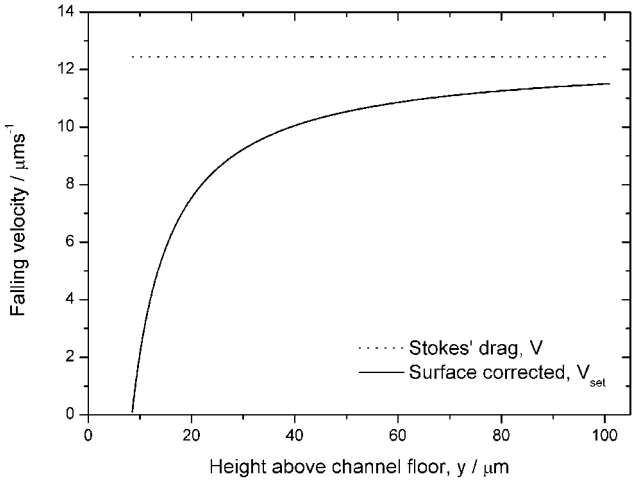

Figure 2.5: *Graph of settling velocity of a 15 μm cell-sized solid sphere as a function of distance from a surface, showing the effect of the presence of the surface in creating a boundary layer of fluid that acts to increase the Stokes drag. However, a cell within a typical 100 μm sized microfluidic channel will still be expected to fall out of suspension within 10 seconds.*

2.7 Conclusion

The motion of fluids driven via pressure through micrometre sized channels was reviewed, with the numerical examples and graphical figures being directly applied to the later experimental chapters. The chapter reviewed the governing Navier-Stokes equation and introduced the Reynolds number that highlights the complete irrelevance of inertia in microfluidic environments, giving rise to its unusual behaviour and greatly simplifying fluid flow. The Reynolds number, Péclet number, Poiseuille fluid flow profile and hydrodynamic focusing ratio was calculated for the chips utilised in the experimental Chapters 5 and 6, highlighting the nature of these low Reynolds number systems. The reliance on diffusion-only mixing and implications of a high Péclet number to the photoporation experiment in Chapter 6 were discussed, where the introduction of relatively large molecules such as plasmid DNA must be pre-mixed in macrofluidic environments to ensure homogeneity, unless specific mixing functionality is added to the chip.

The technique of hydrodynamic focusing was introduced (as implemented in Chapters 5 and 6), a commonly applied technique in microfluidic systems, particularly in sorting and fast diffusion applications to restrict a sample to a narrow region with a fluidic channel. Experimental results were presented which were found to agree exceptionally well with the theoretical predictions. The implications of a microfluidic environment on the viscous forces felt by particles within a fluid were discussed, particularly the necessary corrections to the standard bulk Stokes fluid drag force when a particle is in the vicinity of a static boundary, which has direct implications for optical tweezers and trapping measurements, and for the theoretical predictions of the evanescent guiding experiment in Chapter 5. The velocity of a cell falling towards a boundary was also considered, with design implications for the chip in Chapter 6. The next chapter introduces the fabrication of chips for microfluidic applications.

Chapter 3

Fabricating Microfluidic Chips by Soft Lithography

Lab-on-a-chip (LOC) methodologies promise all-integrated laboratory processes, to perform complete biochemical or medical synthesis and analysis encapsulated on small microchips. Scaled down onto a chip, reagent and sample consumption is reduced, point-of-care or in-the-field usage is enabled through portability, costs are reduced, automation increases the ease of use, and favourable scaling laws can be exploited, such as improved fluid control. The nature of the flow of fluids and suspended particles constrained to the micrometre channels of these chips was explored in Chapter 2 and an array of processes that utilise the advantages of microfluidics, many combined with optical fields and forces, were detailed in Chapter 1, with a selection of examples in Chapters 4 to 6.

In this chapter, the processes used and the considerations for the fabrication of microfluidic chips in one material, polydimethylsiloxane (PDMS) is presented. The fabrication process of PDMS chips is termed *soft lithography* where wet, unpolymerised PDMS is poured onto a hard master mould, cured in an oven, and then peeled and sealed to a substrate. The process is a rapid method, taking two hours of baking to complete, before restarting the process with the same mould. Commercially, microfluidic PDMS chips are unavailable due to their lack of robustness and the limited scalability, with PMMA and glass being more popular chip materials. PDMS is, however, an excellent material for producing microfluidic chips for proof

of principle experiments. The ability to bond it to a wide range of substrates, including silicon and microscope coverslips, makes it a practical option in a research environment, and its optical transparency makes it ideal in a wide range of settings.

Soft lithography was used throughout the work presented in this thesis. In this chapter, the relevant chemistry, optical and material properties and fabrication considerations are reviewed for PDMS as a chip material and for the key mould constituent, SU8. Methods for interfacing the microfluidic channels to external piping are reviewed, and finally methods for integration of optical components are considered, including a novel method for the integration of optical fibres. This chapter serves as a background to the full fabrication protocol given at the end of Chapter 4.

3.1 Soft Lithography

There are a number of possible materials and processes for fabricating microfluidic circuits, including hot embossing of PMMA [166]; femtosecond irradiation and chemical etching of glass [167]; polymerisation of various photoresist including Norland optical adhesive (NOA) [168], SU8 [169] and photo-patternable PDMS [170]; as well as a number of techniques that make use of cheaper of more readily obtainable materials [171–174]. For simple straight channels one can use glass capillary tubes [24] which may be pulled to smaller dimensions, and are commercially available in a wide range of cross sectional profiles [175]. Soft lithography provides fast methods for realising functional microfluidic chips, using a simple replica moulding process from a hard master. Once a mould has been established one can use it repeatably to form many consecutive identical PDMS chips, with the moulds that were used for the work in Chapter 6 fabricating in excess of 100 identical chips through the course of many months.

Soft lithography, pioneered particularly by G.M. Whitesides and coworkers, is a group of fabrication methods concerned with forming structures with feature sizes generally on the micrometre scale, but capable of reaching 30 nm. Conventionally, features on this size scale are fabricated using photolithographic techniques, whereas

soft lithography makes use of flexible elastomers to mould or imprint features. In fact, as soft lithography does not necessarily rely on optical exposure to define structures, the 100 nm lower limit for photolithography (due to optical diffraction and the shortest wavelengths transmitted by optical lenses) can be surpassed using soft techniques [176].

The most commonly used soft lithography material is polydimethylsiloxane (PDMS), the chemistry and physical properties of which shall be reviewed here, prior to detailing fabrication procedures for PDMS microfluidic chips in Chapter 4.

3.1.1 Overview of PDMS Chip Fabrication

To put the material requirements into context, a brief summary of the standard soft lithography replica moulding procedure is given below. A full fabrication protocol can be found in Section 4.A.

1. 2D chip design is drawn on a computer design package, containing the fluidic circuit to be transferred to PDMS
2. The design is printed to a monochrome photomask
3. A master mould is formed in photosensitive epoxy (SU8) by photolithography using the photomask
4. PDMS is cast from the master mould using soft lithography
5. Cured PDMS is cut into chips, fluid inlets are punched into the chip, and the device is sealed to a suitable substrate ready for laboratory use

3.2 Polydimethylsiloxane as a Chip Material

3.2.1 Chemistry of Siloxanes

PDMS is available commercially from several companies and the most commonly available, Dow Corning Sylgard 184 was used throughout the later chapters for forming all microfluidic chips. It is purchased as a two-part “silicone elastomer kit”,

containing a *base* and a *curing agent* which when mixed will polymerise to form PDMS. The key chemical constituents are shown in Figure 3.1.

(a) Dimethylsiloxane copolymer (b) Methylhydrosiloxane copolymer [177]

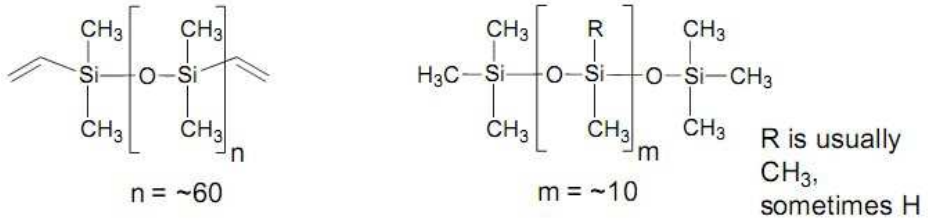

Figure 3.1: *Key PDMS pre-cursers, where (a) is a vinyl-terminated siloxane oligomer and (b) is a shorter, partially hydrosilane-terminated siloxane oligomer. The base contains (a) and a platinum complex, whereas the curing agent contains (a) and (b). Each methylhydrosiloxane oligomer contains a minimum of three hydrosilane ($Si-H$) groups available as hydrosilation reaction sites.* [177]

The base and curing agent both contain the purely vinyl-terminated siloxane oligomer (3.1a), whereas the partially hydrosilane-terminated siloxane oligomer (3.1) is only found in the curing agent [177]. The base also contains a platinum complex necessary as a catalyst for the reaction shown in Figure 3.2. Upon mixing, hydrosilation takes place between the vinyl ($SiCH = CH_2$) and hydrosilane (SiH) groups of the copolymer pre-cursers, forming $Si - CH_2 - CH_2 - Si$ linkages [176]. The hydrosilane groups provide multiple reaction sites, giving rise to three-dimensional cross-linking [177]. The ratio of base to curing agent determines the degree of cross-linking and ultimately the rigidity of the final PDMS elastomer. The reaction is temperature dependent, taking 24 hours to fully cure at room temperature, or just 10 minutes at 180°C.

The product of the reaction is a three dimensional intertwining network of cross-linked polymer chains. At the heart of the PDMS molecule is an inorganic flexible $[-Si - O-]_m$ backbone, surrounded by an organic coating of lubricating methyl groups.

3.2.2 Physical Properties

Borrowing chemistry from silicon-based inorganics and carbon-based cross-linked organics, the resulting properties of PDMS are surprisingly close to what one could

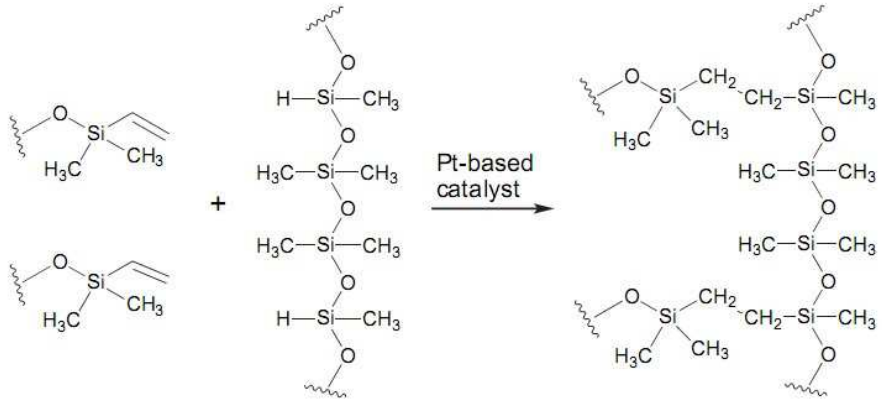

Figure 3.2: *Hydrosilation reaction between dimethylsiloxane and methylhydrosiloxane co-polymers to form cross-linked polydimethylsiloxane silicone elastomer. The relative ratios of the pre-cursers determine the rigidity of the final elastomer. The reaction does not produce any by-products and can be accelerated by heat.* [177]

envisage for an amalgamation of glass (silicon-based) and plastic (carbon-based). The cross-linking of many of these polymer chains makes for a structure that is flexible and reversibly deformable, but whose surface chemistry is defined by the methyl groups [178]. Table 3.1 summarises the physical properties of cured PDMS.

Many of the properties exhibited by PDMS have proven to be very desirable for fabricating microfluidic chips. The temperature-dependent curing time allows it to be mixed, poured onto a mould and cured through heating. Being elastomeric and reversibly deformable, it can be peeled from delicate mould features without damaging the mould or itself, creating an inverted cast in PDMS of the mould. Features of the order of microns can be easily obtained through this replica moulding method.

PDMS is non-toxic, making it a good choice for containing biological samples or implanting *in vivo*. It is also resilient to temperatures in excess of 200^oC and to ethanol, making it easy to sterilise by either for biological applications. Its rubber-like behaviour makes PDMS a forgiving material to work with, having much less stringent fabrication requirements than silicon, silica or other alternatives. The moulded PDMS can be sealed reversibly to itself or many other materials through van der Waals bonding, or sealed irreversibly to many materials through a short exposure to an air plasma.

Once PDMS has been replica moulded, it normally needs to be sealed to a sub-

Property	Characteristic	Consequence
Optical	Transparent; UV cutoff 240 nm	Can illuminate through PDMS for imaging; optical detection from 240-1100 nm
Mechanical	Elastomeric; Young's modulus typically 750 kPa but tunable over 2 orders of magnitude [179]	Conforms to surfaces; facilitates release from moulds; allows actuation by reversible deformation
Electrical	Insulator; Breakdown 2x10^7 $V\,m^{-1}$	Allows embedded electrical circuits; Electrophoresis possible on contained fluid
Thermal	Insulator; Thermal conductivity 0.2 $W m^{-1} K^{-1}$; Thermal expansion coeff. 310 $\mu m\, m^{-1} K^{-1}$; Can withstand 200^oC.	Does not allow dissipation of optical absorption heating or electrophoretic resistive heating; can be autoclaved for sterilisation
Interfacial	Low surface free energy 20 $erg\, cm^{-2}$	Releases from mould easily; can be reversibly sealed to materials
Permeability	Impermeable to liquid water Permeable to gases and non-polar solvents	Contain aqueous solutions in channels; allows gas transport through material bulk; incompatible with many organic solvents
Reactivity	Inert Oxidised by plasma exposure	Unreactive toward most reagents, including ethanol; surface can be etched; can be modified to be hydrophilic and also reactive toward silanes; can be permanently bonded
Toxicity	Non toxic	Can be implanted *in vivo*; supports mammalian cell cultures

Table 3.1: *Physical properties of PDMS. Adapted from* [180, 181]

strate, to seal the fluidic channels or add extra layers with additional functionality to the device. The next section reviews the chemistry and methods for bonding PDMS to various materials.

3.2.3 Surface Chemistry

In its natural state PDMS is hydrophobic, however exposure to an oxygen or air plasma converts the surface methyl ($Si-CH_3$) groups into silanol ($Si-OH$) groups [182], facilitating hydrogen bonding and rendering the surface hydrophilic. This plasma-generated oxidation process has two extremely useful consequences. The first is the that the ability to wet a PDMS microfluidic channel is greatly enhanced if the channel wall is hydrophilic. The second is that a silanol group will readily react with hydroxyl (OH) groups to form covalent $-O-Si-O-$ bonds. Such reactions open the possibility for affixing silanes to the surface of the material for functionalisation [180], or irreversibly bonding PDMS to a number of substrates (including glass, SU8, silicon, polystyrene, polythene or another piece of PDMS [181]).

3.2.3.1 Irreversible Bonding: Plasma-Mediated

As well as exposing the PDMS surface to be affixed, depending on the substrate material, it too may require exposure to the plasma to generate hydroxyl groups on its surface. In the case of silicon and glass, absorption of environmental humidity gives rise to a surface monolayer of silanol groups, meaning only the PDMS needs to be exposed, whereas bonding to another piece of PDMS using a plasma requires exposure on both surfaces.

It should be noted that PDMS after plasma exposure will, in the presence of air, return to its pre-exposure state within 30 minutes [180]. In fact a large degradation in the strength of the bond will occur if not brought into contact with the substrate within 1 minute after exposure. As a result, the PDMS sample must be accessible immediately after exposure and in effect limits the equipment that can be used for the process. Plasma oxidation using a Reactive Ion Etcher (RIE), a commercial oxygen plasma cleaner, and a hand-held corona Tesla coil were all tested as options for this purpose and the results are presented in Section 3.5.

A degree of agility is required to successfully place the PDMS on the substrate such that it fully conforms and it is essential that no dust or other debris is collected on the exposed surface. Further, the oxidised surface must not be inadvertently tou-

ched before placing on the substrate, as this will damage the hydroxyl groups and prevent a successful the bond. This means that one would have a single attempt in correctly placing the PDMS on the substrate, perhaps perfectly aligned to microscopic features on the substrate and in under one minute of exposure to the plasma. This clearly is unpractical, but fortunately these requirements can be relaxed by the use of a polar solvent, such as methanol, ethanol or water [182].

The exposed surface is covered in the solvent immediately after exposure, having three effects: it prevents instantaneous bonding of the two layers when brought into contact; it lubricates the boundary allowing the two layers to be moved laterally relative to one another; and it prevents the treated surface from reconstructing before a bond is accomplished [182]. Once correctly positioned, the composite is placed in an oven or hotplate, evaporating the solvent and allowing the two surfaces to bond. As the two layers are initially lubricated with respect to one another, stresses in the bulk material due to imperfect placement can relax, allowing the layers to come into perfect conformal contact as the solvent evaporates. It was found that the use of methanol greatly improved the evenness of the bond, allowed alignment to substrate structures and ensured that the PDMS was not warped due to imperfect placement.

3.2.3.2 Irreversible Bonding: Curing Agent-Mismatch

Another method for bonding two layers of PDMS, much employed by the Quake group [179], involves producing the two layers with different proportions of curing agent. Two PDMS pieces can be readily permanently bonded together through conformal contact, without the requirement for plasma exposure. When mixing the PDMS, one piece receives an excess of curing agent, whereas the other an excess of base. When brought into contact, heat will initiate hydrosilation at the boundary, forming a bond between the two pieces as strong as the bulk material.

This type of bonding can only be used where both materials to be bonded are PDMS, so is unsuitable where a thin coverslip is required as the base of the chip, so as to allow access to fluid channels contained within via high-NA microscope objectives (as in the case of the bulk of the work in this thesis). This bonding

method was tested and verified, but was not found to be useful for any of the work presented here.

The reduced amount of curing agent in one side of the bond makes the PDMS more flexible than normal and provides an excellent means for creating pneumatic valves using PDMS alone [183].

3.2.3.3 Reversible Bonding: van der Waals

As well as a permanent method of bonding PDMS to substrates, a simpler temporary method is possible that can be more desirable in simpler fluidics applications or surface patterning. PDMS, being flexible, will conform to smooth surfaces and form van der Waals bonds. Such bonds are strong enough to contain a fluid, but not to withstand the positive pressures required to drive a fluid flow. However, generating a negative pressure on a fluid outlet, by sucking using a syringe for example, one can pass fluid through the embedded channels, without separating the PDMS from the substrate. Alternatively, if the channel is made hydrophilic (plasma exposure or to a lesser extent bathing in hydrochloric acid [181]), liquid can flow into the channel through capillary forces alone. Temporary sealing by this method was found to be generally unreliable, particularly for: chips with multiple inlets and where a steady consistent flow was required; where the movement of a microscope stage or pulling on a pipe was likely to separate the PDMS chip from the substrate.

3.2.3.4 Affixing Functional Groups

Functionalisation of PDMS is another useful technique in the fabrication toolbox. The addition of silanol groups through plasma oxidation allows a wide range of silanes ($Si - R$) to be incorporated to the surface. For instance, the surface can be rendered permanently hydrophilic (also reducing non-specific protein absorption) or hydrophobic, through any of a range of silanes, or it can be functionalised for specific protein attachment [182].

One silane that was used extensively to pacify surfaces was (tridecafluoro-1,1,2,2,-tetrahydrooctyl)-1-trichlorosilane (also called 1H,1H,2H,2H- Perfluorooctyltrichlorosilane, or simply trichlorosilane). It was used at multiple stages in the fabrication

procedure, on silicon, SU8 and glass, as well as PDMS. For PDMS, it allowed unreactive layers to be produced. As it cures, PDMS will readily bond with already cured PDMS, forming an homogeneous structure indistinguishable from one made in a single step. By pacifying PDMS, wet PDMS could be poured onto it and separated later after curing, allowing moulds or temporary substrates to be made from PDMS. Details of using trichlorosilane on the mould can be found in Section 3.3.7. Vapour deposition was used throughout to silanise materials by use of a desiccator attached to a vacuum pump.

3.2.4 Degassing PDMS

The PDMS two-part mixture must be very thoroughly mixed before use. An excellent method was to use a disposable plastic fork attached to a hand-drill and mixed for 30 seconds to ensure a homogeneous distribution of the two components. Regardless of the mixing process, upon baking the PDMS would outgas a large amount of air bubbles which, unless addressed, will prevent the formation of a usable chip. This was solved by placing the mixed PDMS in a desiccator attached to a vacuum pump for 20 minutes before pouring onto the mould.

3.3 SU8 as a Mould for Soft Lithography

In order for one to produce PDMS chips containing microfluidic channels, a mould first has to be produced. Moulds were produced by patterning Microchem SU8 epoxy-based photoresist on a silicon substrate using standard photolithography techniques. The basic procedure for producing a mould is as follows:

1. SU8 spin coated onto the substrate to the desired thickness
2. Soft bake: composite warmed on a hotplate to evaporate the solvent, harden and fix the SU8
3. SU8 exposed with UV to photomask pattern in mask aligner
4. Post bake: composite warmed on hotplate to cross-link the exposed regions and further harden these regions

5. Development: solvent used to dissolve unexposed regions, leaving a relief structure of SU8 of the transparent regions in the photomask pattern

6. Hard bake: mould baked in oven for several hours to obtain maximum strength and prolong lifetime

7. Silanisation: mould coated with silaniser to enhance the removal of PDMS

In order to understand the process, the background chemistry of SU8 will first be briefly reviewed, before detailing fabrication considerations for the various steps involved.

3.3.1 Chemistry of SU8 Photoepoxy

SU8 is an epoxy-based polymer, commonly used as a negative tone photoresist, available from Microchem. It comes in a range of formulations each with different viscosities, but all having the same basic constituents in different proportions. Primarily, the formulations have varying quantities of solvent, producing different viscosities and enabling a wide range of thicknesses (0.5 to >200 μm [184]) to be obtained with SU8, through spin coating it onto a substrate. Excluding the solvent, SU8 has two main constituents, a formaldehyde-based polymer (shown in Figure 3.3) and a photoinitiator [185]. Upon irradiation by near-UV, the photoinitiator generates a low concentration of a strong acid, hexafluoroantimaonic acid, which acts as a catalyst for cross-linking the polymer oligomers [186]. The acid protonates (donates H^+) the epoxides on the oligomer, and upon heating cross-linking will occur. Eight reaction sites are available on each polymer molecule, thus a large degree of cross-linking is possible. Upon development, the uncrosslinked regions will be dissolved, leaving only the regions exposed to the UV through the photomask.

3.3.2 Spin Coating

In order to obtain a uniform layer of SU8 across the silicon substrate, it is best spin coated, like many other photoresists used in photolithography. The substrate is held by a vacuum chuck of a spin-coater unit, the surface is covered in liquid resist,

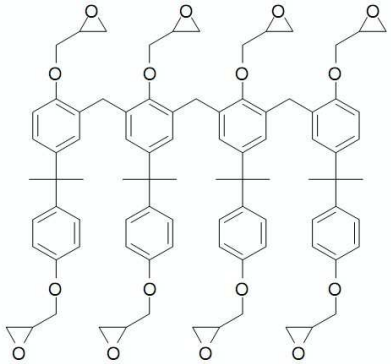

Figure 3.3: *Chemical composition of the main constituent in SU8 photoepoxy. Eight oligomers are available for a high degree of crosslinking upon photoexposure.* [186]

before being spun at a rate of typically 500-9000 rpm for 60 seconds. Some of the material is unable to withstand the centrifugal forces and is flung off, an amount dependent upon its viscosity [187]. A proportion of the solvent is also evaporated off during this spin cycle. The result of the spin is a layer of resist which is found to be dependent upon its spin speed, and for any resist a graph of thickness verses spin speed is always quoted by the manufacture.

Two formulations were utilised for the chips detailed in later chapters, Microchem SU8 2050 and 2000.5. By blending the two formulations it was possible to obtain a wide range of viscosities and any of the other spin curves between 2050 and 2000.5, thus thicknesses of 0.5 to 300 μm could be patterned in single spin steps. It should be noted that the thickness of the resist reduces with the baking steps. A 35 ± 5 % contraction was found to occur between the thickness measured after soft baking and that after exposure and post-exposure bake.

SU8 2050 is extremely viscous and requires special consideration compared to thinner photoresists. SU8 2050 can not be dispensed from syringe easily and should be poured directly from the bottle. In doing so, a zig-zag approach should be used to cover the entire substrate, with the bottle held close to prevent the SU8 from coiling as it flows, capturing many air bubbles. Bubbles can be sucked up by syringe, or the wafer can be left under cover for 15 minutes for the SU8 surface to even out and the bubbles to rise to the surface (where they will not interfere with the final layer). It should be ensured that the whole substrate is covered before spinning, or else there is not an opportunity for it to overcome surface tensions before being

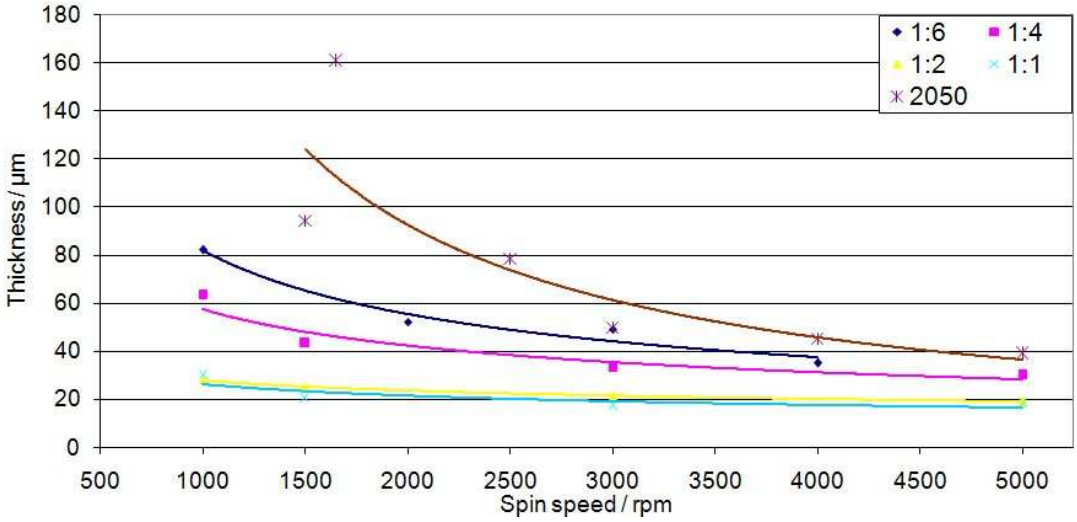

Figure 3.4: *Post-exposure bake thickness verses spin speed for blends of Microchem SU8 2000.5 and 2050. Ratios quoted are 2000.5:2050.*

flung off during the spin cycle.

Rather than employing a single step spin cycle, where the speed is either directly started at the final speed or ramped over time, a three step spin was employed:

1. 10 seconds - 500 rpm
2. 20 seconds - 50% final speed
3. 30 seconds - final speed

The first step spreads the resists, mounding it up at the edges, and a large portion of the excess flies off. The second step causes the vast majority of resist that is to be removed to do so, leaving the final step just to make a relatively small adjustment to obtain the final thickness. The total time is 60 seconds as per the manufacturer's suggested spin cycle, giving an evaporation rate of solvent close to that predicted by a single spin. The acceleration between steps was set to the maximum value of the spinner. This three step spin was found to produce more uniform coatings than in a single step.

After obtaining a uniform coating, there is the edge bead to contend with. The edge bead is resist material mounded up at the edge of the substrate, particularly at the corners, and is a phenomenon of all spun resists. It is particularly a problem where high resolution is desired, as it prevents the photomask being placed in close

proximity to the sample, thus allowing loss of resolution due to diffraction [188]. For thick SU8 the edge bead causes another issue in that once warmed during the proceeding baking steps, the edge bead will re-flow back towards the centre of the sample, significantly increasing the thickness obtained by spin coating and reducing its uniformity. The best method for removal was found to be simply scraping away the edge bead with a coverslip.

The environmental conditions of the cleanroom also play a role when spinning photoresists. The environmental temperature determines the viscosity of the resist, and of the evaporation rate of solvent, both of which affect its thickness. A high humidity was found to have an adverse affect on the adhesion of SU8 to the substrate.

3.3.3 Substrate Preparation

Silicon was used throughout as a mould substrate, as one can get excellent adhesion between SU8 and silicon, 10 cm diameter wafers could be obtained for around £5 each, they can easily be cleaved to size and are more than adequately flat. Silicon has a face-centred cubic structure and for <100> p-type orientated wafers, as used throughout, they can be cleaved in two directions, perpendicular to one another [188]. To cleave, a straight ~1 cm scratch at the edge of the wafer was scribed using a diamond tip. The wafer was then placed with the scribe mark aligned directly above an edge of a glass slide, for instance, and pressure was applied to one side of the wafer causing it to crack its full length along a crystal plane.

The shape of the mould substrate plays a role when SU8 is spun onto its surface. In order to obtain a uniform coating with minimal edge beads, the substrate should not be too rectangular. As a rule of thumb, the length of one side should not be greater than double the other to minimise the edge bead. The substrate should also not be too small as the edge bead will dominate the SU8 profile, giving rise to a layer considerably thicker than predicted by the spin speed.

To obtain good adhesion between the SU8 and the silicon, it is essential that the substrate is clean before spin coating. Two levels of cleanliness were employed, the first being a clean in acetone (ACE) in an ultrasonic bath, followed by a rinse in isopropanol (IPA) and deionised water (DIH_2O), which was for the most part

found to be perfectly adequate. However, at some stages a good level of adhesion could not be obtained without also using a more vigorous piranha solution to remove any possible organic contaminants. As a result in later fabrication work, piranha cleaning was used throughout for piece of mind, but should probably be considered an optional step particularly due to its safety concerns.

A "piranha solution" is formed by mixing sulphuric acid (H_2SO_4) and hydrogen peroxide (H_2O_2), in a ratio of typically 3:1 respectively. The two are carefully mixed, crucially with H_2O_2 being added to H_2SO_4 such to avoid a potentially explosive ratio of 1:1 at any point during the process. The sample is bathed in the solution for ten minutes, or until the sample surface stops bubbling, before thoroughly rinsing in water. The reaction of mixing H_2O_2 and H_2SO_4 is however very exothermic and much care should be taken, with gloves, protective eyewear and clothing being worn. All organic solvents must be removed from the area beforehand, as the combination is potentially explosive. A large beaker of water should be to hand for placing all used glasswear immediately after use. The effectiveness of piranha solution is threefold: H_2SO_4 acts as a powerful dehydrator, H_2SO_4 and H_2O_2 react to form a strong oxidising agent, and the mixture is acidic [189]. The result is that H and O atoms will be stripped off any organics forming H_2O, leaving carbon compounds to be oxidised to CO_2, and anything remaining to receive acid treatment. Surfaces of most materials (including silicon) are hydroxilysed, leaving a hydrophilic coating of OH groups [188, 189].

After sufficiently cleaning the wafer, by either method, it should rinsed in deionised water and dehydrated in a 180°C oven for several hours to remove any remaining water from the surface.

3.3.4 Baking SU8

SU8 must be baked at three stages in the fabrication process: a pre-exposure soft bake to solidify the material; a post-exposure bake to cross-link the oligomers; and a final hard bake to fully cross-link and strengthen the material after development. Although generally a very robust material post processing, much care must be taken in the baking steps if SU8 is to be patterned successfully. The material must not be

subjected to sudden changes in temperature, hence all bakes are broken down into two or three steps to get to the desired temperature. The bake times are dependent upon the SU8 thickness and a good starting point is the manufacturers baking times. Two-step bakes at 65°C and 95°C are recommended for the first (soft) and second (post-exposure) bakes. As a rule of thumb: 65°C prebake time = 1/3 x 95°C bake time.

The soft bake is preferably conducted on a hotplate rather than an oven, so it is normally easiest to conduct all heating steps on a hotplate. In doing so, it is important that a sufficiently large hotplate is used to prevent excessive thermal gradients across the sample, or one known to have a constant temperature across the plate. It is also important that the hotplate is horizontal to prevent internal stresses forming during the bake, or causing an uneven surface. Hot plates were checked with a spirit level.

Periods of five to ten minutes are allowed between some critical steps to allow the SU8 to cool and fully reach thermal equilibrium with the environment. This prevents stressing of the material, leading to cracks or later catastrophic detachment from the substrate in the development or PDMS moulding stages.

SU8 thickness / μm	Soft bake		Post-exposure bake	
	65^oC / mins	95^oC / mins	65^oC / mins	95^oC / mins
35	2	5	1	3
50	3	6	1	5
75	3	9	1	7
100	5	20	1	10
140	5	35	1	15
165	5	30	1	15
225	5	45	1	15

Table 3.2: *Manufacturer bake times for SU8 2000 negative photo-defineable epoxy that should be viewed as a starting point before adapting the times such to optimise the process for the particular substrate and for the environmental parameters. The soft and post-exposure bakes are before and after UV exposure respectively. For the purposes of microfluidic mould fabrication, and where side wall profiles are not of importance, these bake times can be increased by 30% to improve adhesion and improve the success rate during fabrication.*

3.3.4.1 Soft Bake

After spin coating SU8 onto the substrate, it must be baked in order to evaporate the solvent and solidify the SU8, called a soft or pre-exposure bake. This is preferably conducted on a hot plate as oppose to a convection oven, to prevent the solvent evaporating from the top surface and forming a crust before the remaining solvent can escape. The manufacturer's suggested bake times for various thicknesses are shown in Table 3.2.

The SU8 should have solidified after the bake, once cooled back to room temperature. A quick test to ensure the soft bake is sufficient is to gently tap the surface. If a permanent indentation is left then it needs to be baked for longer before exposing, again starting at 65°C and moving up to 95°C. After baking, the sample should be left for 5 to 10 minutes at room temperature before UV exposure.

3.3.4.2 Post Exposure Bake

After exposure, the sample is returned to the hotplate, which selectively cross links exposed oligomers. The purpose of 65°C bake at this stage is simply to avoid the thermal shock in jumping straight to 95°C and as a result, the time here can be relatively short. The time of the 95°C bake is roughly given by: Post exposure bake time = 1.5 x soft bake time. If after development catastrophic detachment of the SU8 from the mould occurs, then it is this bake, along with the exposure time, that should be increased to avoid this.

3.3.4.3 Hard Bake

This is an optional bake performed after development to fully cross link and strengthen the structure before use. It was also found on some occasions to fix small imperfections, such as cracks or small non-adhered sections. The hard bake was conducted just below the glass transition temperature of SU8 (~210°C [190]) at 180°C, for at least a couple of hours. Typically the mould was left in the oven overnight before the final step of silanising. Again, thermal shocks should be avoided. The mould was stepped from 1 minute at 65°C, 5-10 minutes at 95°C before being

placed in the oven, and upon removal was left to cool on a thermal insulator for 5-10 minutes.

3.3.5 Exposure

Exposure of the SU8 layer to the photomask was conducted on a mask aligner, which was measured to consistently have an optical power of 2.78 $mWcm^{-2}$ at 365 nm. The exposure dose is dependent upon the layer thickness, as can be seen from the manufacturer's suggested doses in Figure 3.5, and should be chosen appropriately for a given mould. The spin speed, cleanroom environmental conditions, substrate size and the age of the SU8 blend can all have an effect on the thickness of the layer, often requiring an exposure dose test to be made and examined before immediately exposing the actual mould.

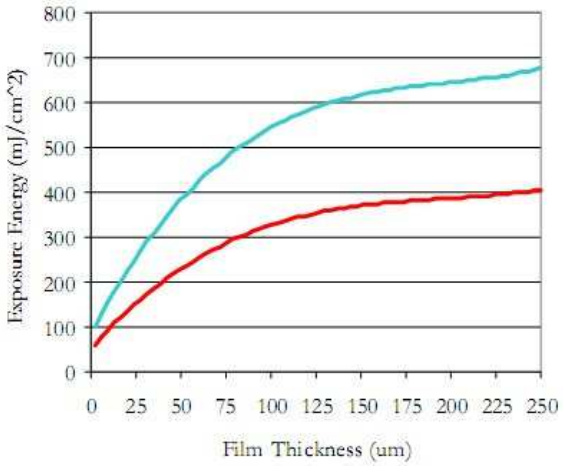

Figure 3.5: *Manufacturer's recommended exposure dose as a function of layer thickness, for a silicon substrate. Glass substrates require a 1.5x dose due to reduced contributions from the back reflection of the substrate. Optimal exposure was found to lie halfway between the i-line (365 nm) curves, representing the upper and lower recommended exposure doses. [184]*

The material of the substrate is also important when finding the correct exposure dose, as it determines the intensity of light that is back reflected by the substrate and does a double pass of the SU8 layer. A glass substrate requires an increase in 50% of the exposure time compared to silicon for instance [190].

Having stated the importance of the correct exposure dose, it can be noted that for most microfluidic applications with feature sizes greater than around 10

μm, the SU8 can be over-, even excessively over-exposed. An over-exposure causes an increasing amount of SU8 to be crosslinked in the upper sections of the layer, producing a non-vertical cross section profile, as shown in Figure 3.6. The angle of the flow channel wall was not considered to be of particular importance except in the case where an optical beam is being directed through it. The advantages of over-exposing are that: it ensures it is sufficiently exposed and therefore that the SU8 adhered well to the substrate; mould fabrication can be a timely process and SU8 is expensive particularly with thick SU8 layers, so it is desirable that the process works every time; a dose test is not necessary; the dose is appropriate for different thicknesses including that arising due to imperfect reproducibility and variable cleanroom environmental conditions; and that the mould fabrication process is reproducible.

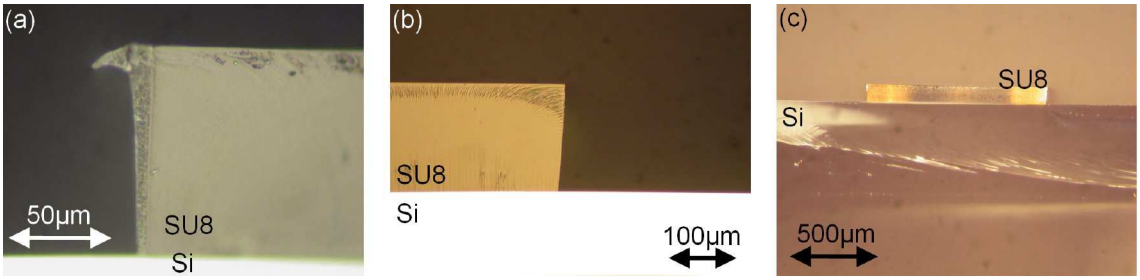

Figure 3.6: *Photographs of side profiles of various SU8 layers, on silicon substrates, where after fabrication, the wafer was cleaved such to cut through the SU8, allowing imaging of the layer. (a) Top hat profile due to the absorption of the shorter wavelength components in the mask aligner UV bulb. This can be eliminated if required by use of a i-line bandpass filter* [184]*. (b) Over-exposure has caused the non-flat side profile. (c) A 1 mm section of SU8 showing a uniform top section.*

3.3.6 Development

After exposure and a cross-linking bake, the features of the mould were developed in MicroChem EC Solvent. The time required is dependent upon the thickness of SU8 and the degree of agitation. Typical development times are 5 minutes for a few tens of micrometres, to 20-30 minutes for a few hundred micrometres in thickness. Generally, moulds were developed in glass Petri dishes, with regular agitation by hand. The time can be significantly reduced by the use of a sonic bath on the lowest setting, but would not be recommended if dealing with small delicate features or

high aspect ratios. After the desired time in the solvent, the mould was placed for 30 seconds into some fresh solvent to prevent the formation of a cloudy white layer thought to be due to saturation of the solvent. EC solvent can be rinsed in IPA and then dried with a nitrogen gun. If any white film is found once placed into IPA, the mould must be developed for longer in EC solvent.

3.3.7 Silanisation

In order to enhance the removal of PDMS from the mould, it can be silanised using a near identical process to that detailed in Section 3.2.3.4, using trichlorosilane vapour without the need for a prior plasma oxidation, as in the case of PDMS. Being able to separate PDMS more easily from the mould is essential in applications where PDMS membrane layers of <100 μm are to produced. Silanisation should be conducted soon after being removed from the hard bake oven; moulds that were left for some time before silanisation were found to have a visually patchy surface indicating a non uniform attachment.

3.3.8 Multiple Layers

Multiple layers of SU8 can readily be fabricated, so as to increase the thickness of on single structure, or to fabricate three dimensional structures. To make a single thicker layer from multiple spin coats, the wafer is spin coated, prebaked, and these two steps are repeated until the required thickness is obtained. To fabricated 3D structures, the first layer is exposed, post-baked, but crucially, not developed. This leaves a flat substrate in order to spin and expose a second layer. The post bake time for the first layer should be reduced considerably in order to compensate for the extra baking steps for upper layers.

Sometimes it is necessary to "patch" together multiple features on a photomask in order to create a complete structure. This can be done by exposing the first features, post baking the wafer for a short period of time, which creates a refractive index change in the exposed features enabling the exposed section to be visualised under the mask aligner, thus allowing subsequent alignments with respect to this

structure.

3.3.9 Photomask

Two types of photomasks were used. Initially iron on soda lime glass masks were used for all work, which had resolutions of as low as 0.5 μm, purchased from Advanced Reproductions Corp. USA. Later, high resolution printed masks were purchased from Circuit Graphics Ltd. UK, which could obtain resolutions of 4 μm, but at a fraction of the cost. These masks are printed to acetate sheets, so in order for them to be successfully used for photolithography, they have to be backed with a rigid flat transparent material. Glass plates were used for this purpose, and the acetate sheet was attached to it using a drop of water, providing strong capillary forces that held the mask in place.

3.3.10 Integration of Optical Fibres

A novel fabrication technique was developed to easily integrate optical fibres into PDMS chips. Much work to date can be found in the literature [21, 24, 25, 30, 31, 72, 133, 151, 191] where optical fibres were used in conjunction with microfluidic chips. Often, the fibres have to be manually aligned to the microfluidic channel or waveguides on chip, or a channel of dimensions a little larger than the fibre is defined in SU8 on the mould, and the fibre is inserted into this channel, providing a rough alignment aid for the fibre. Without matching the height and width of the SU8 to the fibre, such a channel can only act as a rough alignment aid and will no doubt require careful and time-consuming positioning of the fibre by hand or a micropositioning stage. Often the only check for correct alignment is by visualising the movement of particles in response to the optical output of the fibre, or by a trial an error method in optimising the coupling into an on-chip waveguide.

The method developed involved attaching a section of the optical fibre to the mould itself, rather than defining an SU8 channel. As such, a channel of perfectly fibre-sized dimensions was formed in the chip, enabling the fibre to be slotted in ready aligned in two dimensions. This was first demonstrated in the fabrication of

a dual-beam fibre trap chip, where two fibres were inserted into either end of the fibre channel and as such were immediately aligned. Trapping of colloids and biological cells was demonstrated and proved invaluable in studying Brownian motion dynamics in optical binding [5], as the PDMS chamber isolated the experiment from laboratory air fluctuations. Later the same method was applied to integrate a photonic crystal fibre into a PDMS chip for optical chromatography studies, eliminating the standard procedure of manually aligning a free space beam to a long (mm's) length of channel with crucial high precision [2, 9].

The mould for these was formed by first spinning a thin ~5 μm adhesion layer of SU8 onto a silicon substrate, before gently placing the optical fibre onto this. The layer was fully exposed and baked, before continuing on as with the standard procedure; spinning a thicker SU8 layer and defining fluidic channels, positioned under the mask aligner with respect to the ready attached optical fibre. The full fabrication procedure for the fibre trap is detailed at the end of Chapter 4.

3.4 Fabrication Environment & Equipment

For the fabrication of the mould, as previously detailed, the environmental requirements are stringent, requiring a fixed ambient temperature, low humidity and low levels of airborne particles. As a result all mould fabrication was conducted in the cleanroom in St Andrews, with the majority of work being conducted within laminar flow hoods. The fabrication of the PDMS chips is far more lenient, facilitating the moving of the soft lithography process out of the cleanroom to a laboratory laminar flow hood, with dedicated equipment for all of the required steps.

3.5 Bonding PDMS to Substrates

Three methods of plasma-mediated bonding of PDMS were investigate for bonding PDMS chips to glass, PDMS or silicon, as described in Section 3.2.3.1. Firstly an oxygen plasma asher/cleaner was used. The unit was regularly faulty, and at the early development stages of the PDMS chip protocol, provided a lot of confusion

due to unpredictability of when a chip could be bonded. When it was working, an exposure of 10-30 seconds at 100W was sufficient. The asher was later abandoned in favour of using a Reactive Ion Etcher (RIE) unit, as per Jo *et al.*'s recommended parameters [192]. This allowed chips to be uniformly and reproducibly bonded, but due to the high vacuums required, the process took half an hour per chip, despite the plasma exposure only lasting a few tens of seconds.

Haubert *et al.*'s technical note [193] led to the purchase of a hand-held, portable, low-cost, corona treater. The results were found to be excellent, and proved to be lenient on exposure times and doses. Simply waving the plasma emitting tip within 1 cm of the sample for around 10 seconds was enough. As previously mentioned (Section 3.2.3.1), after treatment the two surfaces were rinsed in methanol, placed into conformal contact, and left in a 65^oC for >4 hours.

3.5.1 Integration with Optoelectronic Structures

As well as bonding PDMS to PDMS and to glass, other materials were tested. For development of the integrated optoelectronic trap [16,194], the bonding of PDMS to SU8 was tested and proved successful, by treatment of the PDMS layer only. This could prove useful for interfacing the chip more successfully by using the method in 3.6, as well as producing an optical window, and the possibilities for additional fluidic circuits before entering the GaAs layer.

In collaboration with the Sea Mammal Research Unit (SMRU) in St Andrews, a project was investigated for the inclusion of microfluidics on top of photonic crystal based sensors. The application is shown in Figure 3.7a, showing a seal with an attached tag containing GPS, a long life battery and numerous pressure, temperature and other sensors, plus a mobile phone transmitter for relay of the obtained data when the seal is at the water surface. There is a desire to add additional functionalities to these tags, and the option being investigated was using optical sensors, in particular photonic crystal slot waveguides for sensitive refractive index changes (see Figure 3.7b). Figure 3.7c shows a PDMS microfluidic chip bonded to an SOI substrate containing an array of photonic crystal waveguide sensors.

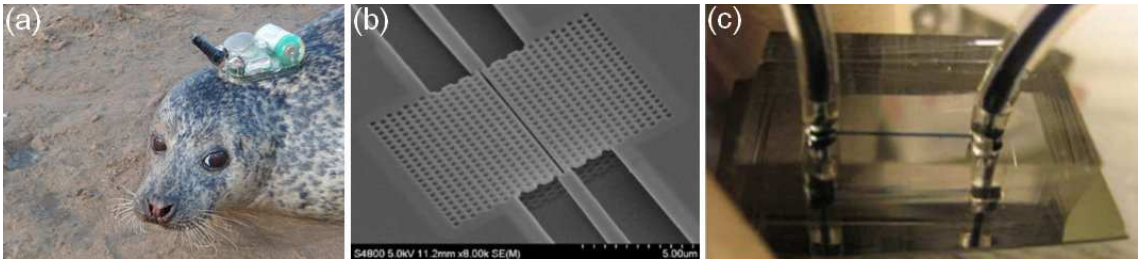

Figure 3.7: *Integration of microfluidics with optoelectronics for refractive index sensing. (a) An application for integrated optoelectronics and microfluidics, in collaboration with the Sea Mammal Research Unit (SMRU), University of St Andrews, where new sensors are desired for incorporation into their existing GPS-equipped seal tags. (b) SEM image of a photonic crystal slotted waveguide in SOI, for refractive index measurements through the translation in the cavity resonance. By suitable surface chemistry, the sensor could potentially target specific molecules, through antigen/antibody binding for instance. (c) Photograph of the PDMS microfluidic section bonded to 5x10 mm silicon substrate and aligned to waveguides, showing fluid channel as indicated by blue dye.*

3.6 Fluid Inlet Interfacing

In early use of the fabricated chips, a robust method of interfacing the microfluidic chips with tubing, for connecting up to syringe pumps, had not been established. This in fact proved to be quite an issue and would regularly be a point of failure when using the chips. Various methods of gluing pipes, pipette tips, glass tubes and later blocks of PDMS [195] were all tested, with limited success. This was mainly due to adhesive flowing into the channels due to capillary action, or later cracking and leaking when in use.

A method was later found that proved to be very successful. Holes were punched into the PDMS where the inlet was required (initially using a sharpened football pump valve, later much more reliably using a Harris Micro Punch), with a diameter around 20% smaller than the tubing to be inserted. The tubing was then simply pushed into the hole, forming a good seal. Depending on the size of the tubing, different thicknesses of PDMS were used to match the criteria of a good seal and such that it could be punched without splitting the PDMS. Where different sized inlets were to be used on the same chip (in the case of the Photoporation chip), multilayered PDMS was used to match these criteria.

3.7 Conclusion

This chapter serves as a grounding for Chapter 4 and outlines the basic soft lithography process, where a master mould is used to cast PDMS replicas, which are subsequently bonded to a substrate, and interfaced with piping for usage. The physical, chemical and optical properties of the silicone elastomer PDMS were reviewed, with particular focus on those properties that make it desirable for the fabrication of microfluidic chips. Surface chemistry and methods for irreversibly attaching PDMS to a substrate using plasma were detailed. A new chip design requires the fabrication of a new master mould and the material SU8 was reviewed for this process, with the necessary spin speeds, bakes times and exposure doses required to successfully produce a chip mould. Some methods for integrated PDMS with optoelectronic structures were presented, before detailing methods for interfacing the microfluidic channels with piping for driving fluid and samples through the chip. The following chapter lists in full a protocol in the Appendix for fabricating PDMS chips with integrated microfluidic channels and optical fibres, based on the aspects reviewed here. It first details two applications of fibre-integrated PDMS chips.

Contribution

All of the work was conducted by R. Marchington, except for that in Section 3.5.1 which were collaborative projects. R. Marchington worked with S. Cran-McGreehin on fabrication development for the integrated optoelectronic trap work and later with D. McRobbie. R. Marchington made the link with B. McConnell and A. Hall from the Sea Mammal Research Unit (SMRU), University of St Andrews to look into collaborative projects, one of which was the development of new sensors for their seal tags. R. Marchington made PDMS chips and bonded them to photonic crystal substrates fabricated by U.P. Dharanipathy, A. Di Falco and M. Scullion from the Microphotonics group.

Chapter 4

Integration of Optical Fibres into Microfluidic Chips for Trapping & Chromatography

The applications for integrating optical and microfluidics components are vast and Chapter 1 detailed many examples. This chapter demonstrates two microfluidic chips where the soft lithography techniques of Chapter 3 were employed. A dual beam fibre optic trap in PDMS was fabricated for immobilising cells and particles within an integrated microfluidic channel, where the chip served the purpose of fluid delivery, fibre alignment and isolation from the surrounding environment. Two optically trapped particles within the trap can become *optically bound*, a unique situation where the refocusing of light by the presence of the particles causes them to lie at a separated distance. Perturbations to one of the particles is transferred to the other through the influence on the optical field and as such, is a fascinating multi-bodied system for studying light-matter interactions. The second chip was utilised in optical chromatography where the unique beam properties of an integrated photonic crystal fibre was used for simultaneous fractionation of particles and fluorescence generation.

In the appendix to this chapter, a step by step protocol for fabricating microfluidic chips in PDMS is given, with a novel method for incorporating optical fibres. The background to all the fabrication steps listed are presented in the previous chap-

ter. By incorporating optical fibres onto the mould for use in the PDMS casting procedure, the location of the optical fibres can be fixed, allowing pre-alignment of on-chip optical beams with micrometre position at the fabrication stage. The use of single fibres on the mould, but intersected by fluid channels, allows pairs of fibres to be intrinsically aligned to one another, or for a fibre to be inherently aligned to a microfluidic channel. Also, the mould can be used in many tens of castings and many identical chips can be made, often a requirement for biological studies where statistics need to be collected over multiple runs or where the chips can not be reused due to bio-fouling or sterility issues. With many points of possible failure in the process, the step by step guide will aid a beginner or advance a novice in the process of soft lithography to produce robust, reproducible chips, which is not believed to be currently available in the published literature. The inclusion of some additional steps enables the integration of optical fibre onto the mould, allowing beam delivery to be integrated into the chip at the fabrication level and with the micrometre resolutions obtainable in photolithographic processes.

4.1 Fibre Traps in Microfluidic Chips

Optical trapping with high numerical objectives is an established tool for non-invasive particle manipulation and force measurements, as seen in Chapter 1. However, single beam traps do lack the ability to exert a uniform optical stress over an extended range. Dual beam traps make use of large beam divergences, typically from the output of two optical fibres [21]. The two counter-propagating beams give rise to large optical pressures for a reduced power density. It allows one to steadily trap single or multiple particles (optical binding) [191] with a reduced risk of optically induced thermal effects (photodamage), which is of particular importance when manipulating biological cells. In addition, optical forces from a counter-propagating fibre trap have also proven to be a great asset for immobilising or interrogating overall cellular structures for diagnostic purposes, such as in the case of optical stretching [133]. It is indeed possible to immobilise a single particle in a fluid flow, whilst collecting fluorescence or a Raman signal through a decoupled microscope

objective [24].

One of the key considerations for counter-propagating fibre traps is the alignment of the two fibres [21]; a misaligned dual beam trap would affect the balancing of the scattering force on the trapped particles and produce an unstable trap [196]. Once the fibres are well aligned, one can simply tune the power from each of the fibres to manipulate the particle position axially within the optical trap.

Various methods of aligning two optical beams for trapping have been developed [17, 21, 24, 25, 31, 32], such as the use of V-grooves etched into a silicon wafer as an alignment aid demonstrated by S.D. Collins et al. [31]. Another approach avoids optical fibres altogether and instead has inherently-aligned collinear trapping laser pairs contained within an all-integrated microfluidic semiconductor chip [16], and the use of integrated waveguides has also been demonstrated [23, 33].

Optical fibres provide a very convenient means of delivering an optical beam from a bench-top laser to within a microfluidic chip. Coupling light into the fibres can be achieved using a fibre launch system, consisting of an objective or graded index lens and a 3D positioning stage, but requires careful alignment to ensure a good laser to fibre couple efficiency. Alternatively, pigtailed laser diodes with FC/PC fibre terminations can be used, where fibres have been attached to the laser facet during manufacture and hence avoid manual alignment. The FC/PC terminations enable the laser output to be coupled into the trapping fibre of the PDMS cartridge simply by screwing the FC/PC connectors together, and allows for rapid setup on any microscope, and for the cartridge to be easily exchanged if and when desired. Two separate laser sources can be used, or alternatively the power from one laser can be split into two, using a fibre 50/50 coupler in order to provide two beams of equal scattering force.

The next section looks at a specific application of a fibre trap; studying the interactions between light and multiple trapped particles in an optically bound configuration.

4.2 Optical Binding

Figure 4.1 shows a PDMS fibre trap chip, trapping (a) silica colloids and (b) HL60 cells, with the fluid channel running left to right and the two optical fibres coming from above and below. Both examples show optical trapping of two particles. At first consideration, one might expect that adding multiple particles to a dual-beam trap would generate a conglomerate at the centre of the trap, but it can clearly be seen that this is not the case. This phenomena is termed *optical binding* and was a direct application for the PDMS fibre trap chip.

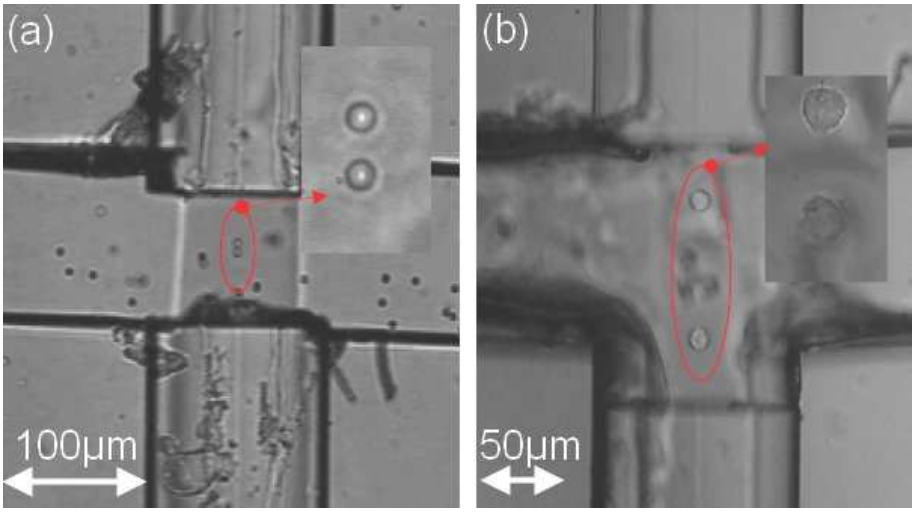

Figure 4.1: *Trapping of particles using counter-propagating dual beam trap in a PDMS microfluidic chip with a wavelength of 1064 nm, emitted from two single mode fibres. Fluid flow is from left to right. (a) Trapping of two 3 µm silica spheres. The inset image shows the magnified spheres at 100x magnification. (b) Trapping and optical binding of two HL60 cells. The inset image shows the magnified spheres at 50x at a smaller optical binding distance.*

Optical binding arises from the interplay between light and particles, the influence of these particles on the light field through refraction and reflection, and the resultant equilibrium trapping positions or self-organisation of the particles in response to this changed field. In the case of two spheres in a dual beam counter-propagating trap, the influence of the spheres on the two diverging beams is to focus the light, creating two focal positions, plus introducing some additional Fresnel reflection components [191]. The dynamic gradient and scattering forces then determine the movement and eventual equilibrium positions of the two particles after the introduction of an additional particle.

Interestingly, for two spheres trapped there is not one but two possible equilibrium states, with the particles sitting within or outside the two focal points in the axial direction [45, 197]. This simple system is therefore bistable and the particle positions between these two possible states exhibit hysteresis [45]. First reported in 1989 [198, 199], the field of optical binding has received increased momentum in recent years [200–204], due to interests in application to self organisation in crystallisation or the formation of photonic crystals, but also as it continually proves to be an excellent test model for our fundamental understandings of light-matter interactions [204].

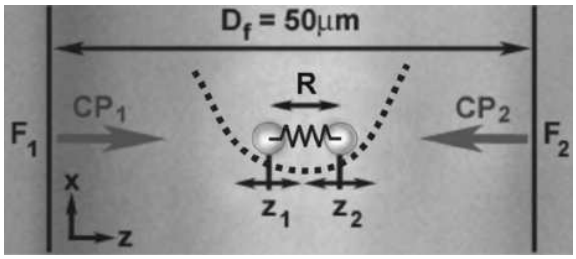

Figure 4.2: *Optical binding in a counter-propagating dual beam trap. Here two 3 μm silica spheres are trapped by two counter-propagating beams (CP_1 and CP_2) of wavelength 1070 nm and optical power 110 mW from each single mode fibre F_1 and F_2, separated by $D_f = 50$ μm. The equilibrium separation of the spheres, $R = 6.9\,\mu m$. The two spheres reside in an energy potential well generated by the optical field, as shown schematically by the dashed line, but that also influence each others relative positions $z_{1,2}$ due to the perturbations in the field due to Brownian fluctuations in the particle positions. Hence, the overall optical force is governed by the optically generated potential well and the cross interaction due to the relative motion of the two spheres, as indicated by the spring.* [5]

A study was conducted on the nature of the optical cross interaction between the two optically trapped spheres [5]. As mentioned in Section 1.2.3, it is possible to extract optical forces by the use of a fast camera. The positional information of two optically bound spheres was recorded at 384 frames per second for 26 seconds, enabling the trap stiffness and optical binding cross interaction forces to be extracted from the cross correlation of the two spheres, whilst driven by the Brownian fluctuations in their positions. As well as the optical cross interaction, a hydrodynamic cross interaction exists also, as the movement of one sphere displaces the fluid which in turn is felt as a Stokes drag force on the other sphere. This was taken account of in the model also, as in the previous studies [205, 206] on this hydrodynamic contribution.

Critically for this experiment, disturbances in the fluid had to be eliminated. Capillary tubes could not be used due to the requirement for close proximity of the fibres and so as not to introduce additional reflections from the capillary tube wall, hence the use of the PDMS chip for this purpose. After filling, the chip was completely sealed with epoxy, thus entirely isolating the system from pressure fluctuations. Two spheres were then loaded into the fibre trap using a single beam *helper* tweezers.

4.3 Optical Chromatography with Photonic Crystal Fibre

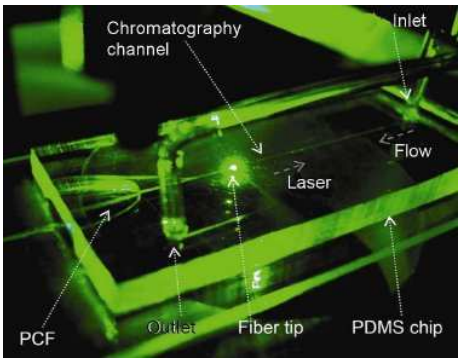

Figure 4.3: *Photograph of the PDMS optical chromatography chip with integrated PCF. The chip enables rapid alignment of the optical beam to a 5 mm long microfluidic channel, removing the requirement for time-consuming alignment of a freespace invisible IR beam to a microscopic fluid channel at the start of each experiment as in previously reported works* [127–129, 132, 135]. *The endlessly single mode property of LMA PCF allows the introduction of both 1070 nm for fractionation and 532 nm for on-chip fluorescence excitation.* [2]

Another application that the integrated fibre was applied to, and that offered superior capabilities and ease of integration was optical chromatography. As introduced in Section 1.4.4.2 optical chromatography is a passive method for fractionating particles, based on the differing relation between the Stokes fluid drag force and the optical scattering force. A slightly diverging beam is introduced counter-propagating into a fluid flow, such that equilibrium positions where the fluid and optical forces balance, the so called *retention distance*, z that can be shown [129] to have the

following dependence

$$z = \frac{n_{medium}\pi\omega_0^2}{\lambda}\sqrt{\frac{n_{medium}PQa}{3\pi\mu\nu c\omega_0^2} - 1} \tag{4.1}$$

where n_{medium} is the refractive index of the medium, ω_0 is the beam waist at the focus, λ is the laser wavelength, P is the optical power, Q is the conversion efficiency of optical power to exerted radiation pressure that depends on the particle refractive index, $n_{particle}$, μ is the fluid viscosity, ν is the fluid velocity experienced by the particle and c is the speed of light. This equation has been found to be appropriate down to radii, a of 100 nm [9] despite the fact it is a Mie ($a > \lambda$) scattering and ray optics derivation [129]. The use of a near-collimated beam, means a slight difference in the optical properties produces a large change in the resulting equilibrium position, therefore the technique is highly sensitive to both refractive index and size. The Q value can be calculated from the angle dependent Fresnel equations revealing the difference between polymer ($n_{particle} = 1.59$) and silica ($n_{particle} = 1.43$) to be 33%, and it has readily been shown that retention distances can differ in the order of hundreds of micrometres for a change of a few micrometres in particle diameter [126].

It was realised that a number of photonic crystal fibres (PCF) could be capable of producing a lightly diverging beam as required to maximise the sensitivity of the technique, whilst maintaining a beam of the order of micrometres. Several commercially-available PCFs were modelled and large mode area LMA-25 and LMA-20 (NKT Photonics) were settled on for application to optical chromatography. These fibres provided 25 μm and 10 μm output mode areas respectively, could deliver 1070 nm (and 532 nm for LMA-20) laser light with low attenuation, and had NAs of 0.04 and 0.055 respectively (compared to 0.14 for single mode fibre). Using these fibres, equation 4.1 was verified and found to be in excellent agreement with the experimentally obtained retention distances using PCF.

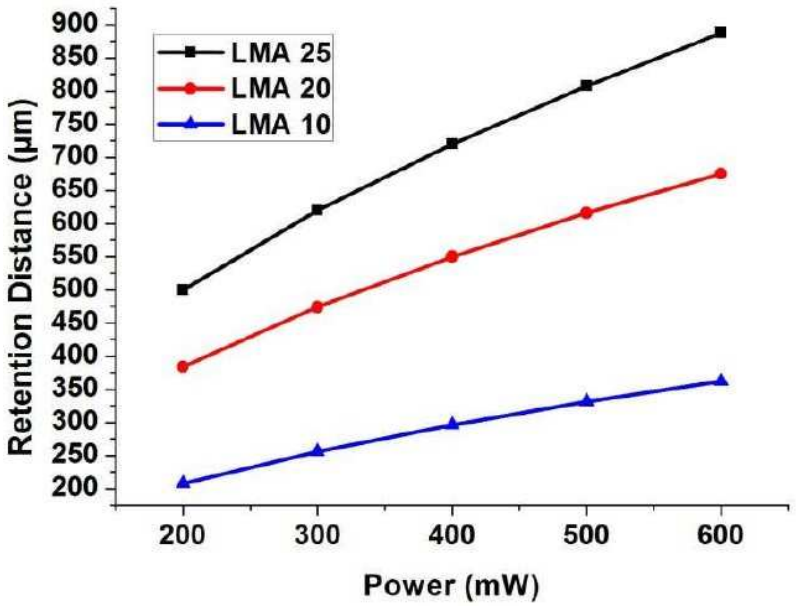

Figure 4.4: *Comparison of the theoretical retention distances for a 2 μm polystyrene bead in a 50 μms^{-1} fluid flow towards 500 mW of 1070 nm laser light emerging from one of three different LMA PCFs, exhibiting respective mode field diameter of 25, 20 and 10 μm.* [9]

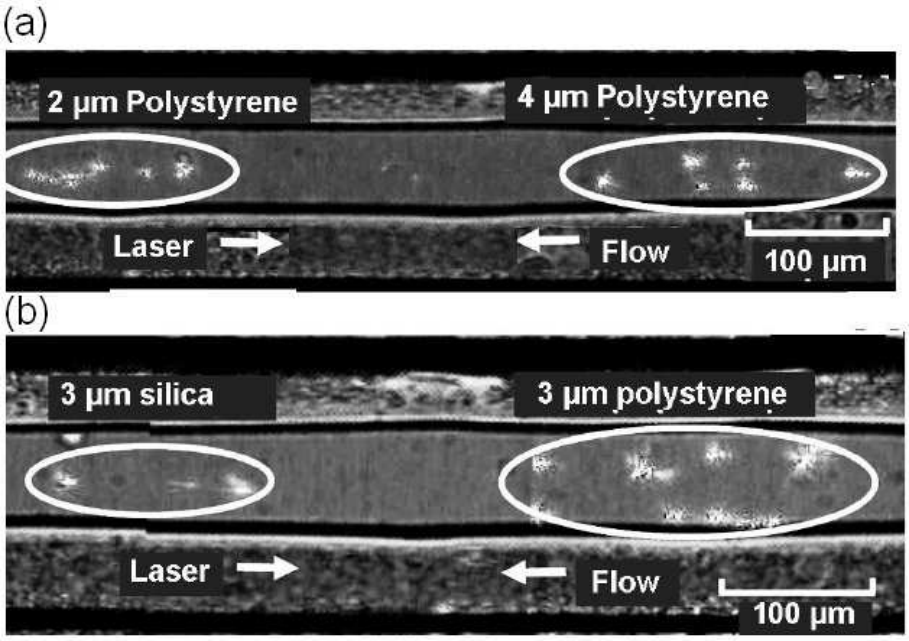

Figure 4.5: *Optical chromatography of polystyrene and silica beads using PCF in a PDMS chip (a) 2 and 4 μm diameter polystyrene beads separated by a distance 420 μm using 520 mW of laser power and a flow rate of 35 μms^{-1}. (b) Silica and polystyrene beads both of 3 μm diameter separated by 360 μm for a laser power of 1.0 W and 39 μms^{-1}, due to their differences in refractive index.* [2]

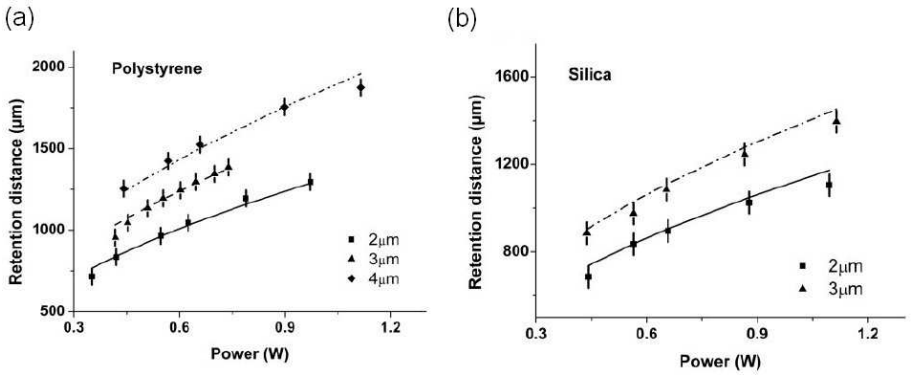

Figure 4.6: *(a) Retention distance as a function of power for three sizes of polystyrene spheres. (b) Retention distance as a function of power for two sizes of silica spheres. The dots show the experimental values of retention distance and the lines show the corresponding values obtained by theoretical calculation based on Equation 4.1. The error bars show the maximum spread of a single species when ~10 particles were held at the retention distance, due to perturbations to the optical field. This data shows the high sensitivity of the retention distance in optical chromatography, to both the size and refractive index of the captured particles.* [2]

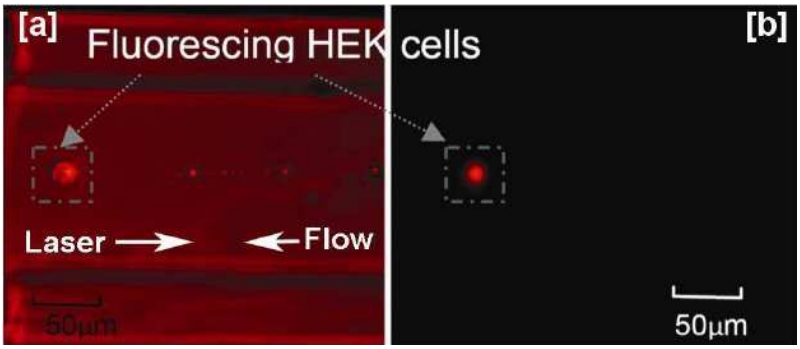

Figure 4.7: *Fluorescence excitation of DsRed-transfected HEK293 cells in the PDMS optical chromatography chip. The balance of Stokes fluid drag force and the optical radiation pressure give rise to size and refractive index dependent equilibrium positions at different retention distances. (a) Bright field image cell of a fractionated cell using 1070 nm, with simultaneous red fluorescence excitation using 532 nm, both of which are coupled into the endlessly single mode LMA PCF. (b) On-chip fluorescence of the same HEK293 cell.* [2]

Optical chromatography poses the practical challenge of accurately delivering the beam to within a confined fluid channel; having alignment along several millimetres; and most critically but more subtly, that the peak in the Poiseuille parabolic flow profile matches the peak of the optical Gaussian profile such to maintain a co-linear balance in the two forces. The fabrication process listed above was utilised to fabricate chips to perform optical chromatography meeting these requirements [2]. The last point was trivial for this method as a single section of PCF on the mould was

used to form both the alignment channel for the insertion of PCF into the chip and for the microfluidic channel, such that the cross-section profile of the fluid channel was determined by the diameter of the PCF. Figure 4.5 shows the fractionation of two sizes of polystyrene beads with a 420 μm separation distance, and a 350 μm separation of polystyrene ($n_{particle} = 1.59$) and silica ($n_{particle} = 1.43$) of the same size, and plotted in Figure 4.6.

Another property of LMA PCF is that it is endlessly single-mode, allowing multiple wavelengths to be coupled into the chip via the fibre [30]. This was utilised for fluorescence generation of two types of biological cells. The first were photoporated (see Chapter 6 for details on photoporation) HEK293 cells transfected with DsRed DNA. The second were HEK293 cells that through phagocytosis [105] had uptake of red fluorescing dielectric beads, that served both the purpose of increasing the effective refractive index of the cells and of being fluorescent such that the successful fractionation of these cells could be verified.

4.4 Conclusion

Two applications of PDMS microfluidic chips with integrated optical fibres were demonstrated. The first was a fibre trap chip, where the PDMS chip provided rapid alignment of the optical fibres and a microfluidic sample delivery channel. Details of an optical binding experiment that utilised the chip were presented, which was strongly reliant on the PDMS chip to provide an enclosed, isolated and sealed chamber for measuring noise sensitive Brownian dynamics of microscopic particles. By recording the Brownian-driven positional variations in two optically bound particles, the correlation between the particle displacements was determined and used to extract the influence of the optical binding and hydrodynamic contributions.

A second experiment utilised a single PCF co-aligned to a long microfluidic channel for conducting optical chromatographic fractionation. The influence of the mode output area from various commercially available PCFs, on the optical chromatography retention distance was calculated, using a ray optics model. Two of these fibres were then utilised in the fractionation of polymer and silica beads and valida-

ted against the model. On-chip fluorescence generation was demonstrated utilising the endlessly single-mode property of the PCF, and its application to fractionating biological cells tagged with dielectric beads was detailed.

A full fabrication procedure is detailed in the proceeding Appendix, with step by step instructions and hints for successful fabrication of PDMS microfluidic chips, and with the optional integration of optical fibres into the chip. A second microfluidic optical sorting technique is demonstrated in the following chapter, utilising evanescent fields inserted using only the objective lens of a total internal reflection fluorescent microscope.

Contribution

R. Marchington developed the fabrication procedure for PDMS microfluidic chip fabrication in the St Andrews Physics & Astronomy Department, initially supervised by P. Reece and S. Neale. He worked closely with N. Metzger on the optical binding experiment, fabricating the chips, and assisting with the optical fibre work in the laboratory. R. Marchington conducted initial trials with PCF for optical trapping work with D. Gherardi, and designed a photomask for utilising PCF in optical chromatography. He assisted P. Ashok in learning chip fabrication, the setting up of the optics and the running of the experiment, as well as upgrading the microfluidic equipment as required for the slow, stable flow for that experiment.

4.A Appendix: Full Fabrication Protocol

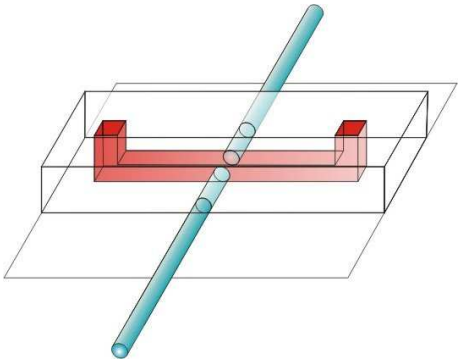

Figure 4.A.1: *Design of the PDMS fibre trap chip, showing the fluid channel in red and the optical fibres in blue. The PDMS block containing fibre alignment channels and a microfluidic channel for sample injection is sealed to a microscope coverslip, enabling the use of high-NA optics if required. This chip provides an enclosed fluid environment, isolated from surrounding air fluctuations, and has intrinsically-aligned and self-sealing channels for the optical fibres, which may be placed with a separation according to the specific application.*

This appendix demonstrates how the use of standard soft-lithography techniques can be utilised to create a simple fibre optics aligner platform using PDMS such that a counter-propagating dual-beam scattering force trap can be easily implemented on an inverted optical microscope. The platform provides two mutually aligned fibre channels in which the optical fibres can be inserted, separated by a microfluidic flow channel where a sample can be flowed into the chip and through the trapping region. PDMS is optically transparent and biologically safe thus the integration of the microfluidic flow channel with a dual beam optical scattering force trap provides a stable, sealed and biology-compatible environment. The chip is sealed onto a coverslip allowing the channel contents and trapping region to be clearly imaged or interrogated using a high NA objective.

A step by step guide to successfully fabricating a PDMS fibre trap chip is provided, for use on any microscope. The procedure is however applicable to fabricating any single layered chip in PDMS containing a 2D microfluidic circuit and optical fibres, or without the fibres by omitting Section 4.A.2.3. Fabrication of the microfluidic alignment cartridge consists of three main steps: designing the microfluidic flow channels and forming a monolithic photomask; constructing a master mould;

and moulding any number of replicas from this mould in PDMS. By using a single optical fibre as part of the mould for the fibre trap, a channel can be formed in the PDMS to align and hold the two trapping fibres. Perpendicularly-intersecting SU8 ridges are added to the mould which form flow channels in the final device for the insertion of the desired sample fluid into the trapping region.

In this design, a single mode fibre itself is used in the mould and in doing so provides an exact fit for the two optical trapping fibres, producing inherent pre-alignment and a perfect fluid seal.

4.A.1 Design of the Photomask

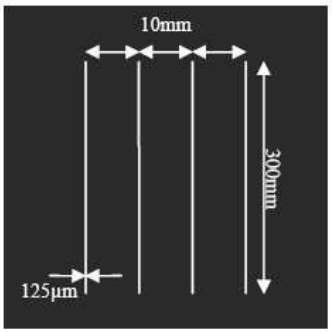

Figure 4.A.2: *Photomask for use in mask aligner to selectively expose SU8 to form ridges on the mould from which flow channels will be defined in PDMS. This mask will produce a mould for fabricating four chips with every PDMS casting.*

The first step in any soft lithographic process is the formation of a suitable photomask, which defines the design of the flow channels. This consists of a transparent flat material, such as glass or a sheet of acetate, which has been imprinted with a monochromatic plan view of the desired flow channel layout. During the fabrication of the mould, the photomask is used to selectively expose an epoxy (SU8) to UV light, allowing the constituent molecules to cross-link and form a permanent insoluble structure. A photomask can be rapidly formed by printing a CAD design to an acetate sheet with a high resolution printer, or can be commercially obtained (for instance Circuit Graphics Ltd, UK). The design can be as simple as four parallel lines, of length 800 mm, width of 125 µm and separated by 10 mm, as shown in Figure 4.A.2, which would form a mould to produce four optical trap chips from each PDMS cast.

4.A.2 Fabrication of the Master Mould

This section details step by step the fabrication procedure for producing a mould for soft lithography, with recommendations, timings, tips and troubleshooting points. The inclusion of an optical fibre on the mould is optional. It is recommended that the process is conducted in a cleanroom environment, that powder-free (e.g. nitrile) gloves are worn, and a good set of mechanical tweezers are used.

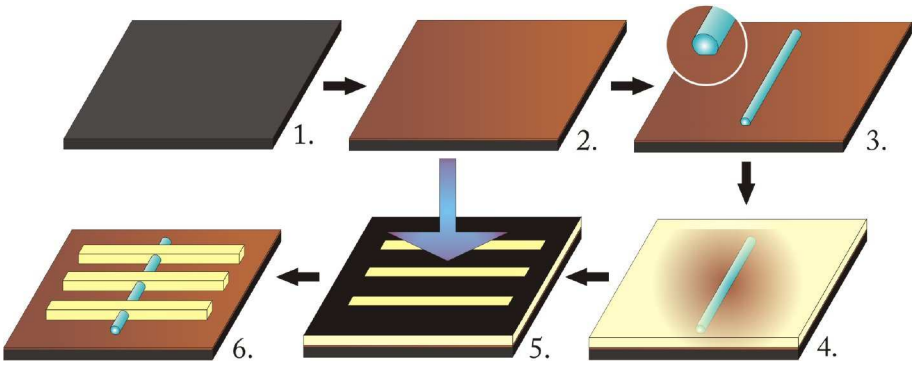

Figure 4.A.3: *Fabrication steps of mould for casting PDMS fibre-trap microscopy cartridges. 1) Cleave silicon substrate 2) Spin 5 µm thick SU8 layer 3) Position optical fibre and cure SU8 to adhere fibre to mould 4) Spin 165 µm thick SU8 layer to cover fibre 5) Define microfluidic flow channels through UV exposure of photomask 6) Cure and develop to finalise mould.*

4.A.2.1 Preparation

Timing 30 mins

1. Weigh and mix 15 g of SU8 2000.5 and 5 g of SU8 2050 photoresists to produce SU8 3:1 mixture. Use a stir plate and magnetic bar to obtain homogeneity. Do not use until the mixture is free of bubbles.

2. Soak 5 cm of optical fibre in ACE for 10 minutes before peeling away jacket and buffer layers from the cladding. Rinse in IPA.

3. Place probe of radiometer in mask aligner and expose to UV light. Record exposure energy at 365 nm for calculation of SU8 exposure times in later steps.

4.A.2.2 Prepare substrate

Timing 1.5 hr

1. Cleave silicon wafer to 4 x 6 cm using diamond tip.

2. Clear wafer of cleaving fragments using N_2 gun.

3. Immerse wafer in acetone and place in sonic bath for 10 minutes.

4. Rinse in IPA, followed by DIH_2O.

5. Bake in oven or hotplate at 200°C for 1 hr to dehydrate wafer. Allow to cool before continuing.

TROUBLESHOOTING If continued problems arise in the adhesion of SU8 to the substrate, a stronger cleaning procedure can be implemented using piranha solution (see Section 3.3.3 for details).

4.A.2.3 Producing mould: Fixing of the optical fibre

Timing 1 hr

1. Place wafer on photoresist spinner and cover surface in SU8 3:1 mixture using a pipette. Spin at 500 rpm for 10 s, 2500 rpm for 10 s and 5000 rpm for 60 s to produce a ~10 µm thick SU8 layer to serve as glue for the optical fibre. This layer also prevents the PDMS from getting caught beneath the fibre and tearing during replica molding. CRITICAL STEP Ensure that the chuck is not much smaller than the wafer used and sufficiently held by the vacuum before spinning. TROUBLESHOOTING The SU8 layer will contain streaks if the substrate was not sufficiently cleaned. If this is the case, immerse wafer in EC Solvent and place in sonic bath for 10 minutes, rinse in DIH_2O and continue from step 4.A.2.2.3.

2. Gently place optical fibre onto wafer using a pair of tweezers, so as not to allow it to slide or disturb the SU8 layer and such that it parallel to the wafer's longest side and in the centre. Very carefully press fibre into SU8 at a few points along its length.

3. Pre-expose bake: 3 minutes at 65°C immediately followed by 12 minutes at 95°C to evaporate the SU8 solvent. This can be done using two hotplates or

better still using one hotplate and ramping the temperature over time to reach 95°C at the end of the third minute. PAUSE POINT Allow to cool gently so as not to induce thermal shock and on a flat surface. TROUBLESHOOTING Once the wafer has cooled, touching the surface softly on one corner with a pair of tweezers should not leave a mark or penetrate the SU8 layer. Re-ramp the wafer back to 95°C for a few minutes longer and recheck before proceeding to the next step if this is not the case.

4. Expose entire wafer to 400 $mJcm^{-2}$ of UV in mask aligner (i.e. if bulb was measured to emit 4 $mWcm^{-2}$ in step 4.A.2.1.3 then expose wafer for 100 s). Note that the photomask is not required in this exposure.

5. Post-expose bake: 3 minutes at 65°C immediately followed by 9 minutes at 95°C. PAUSE POINT Allow to cool gently so as not to induce thermal shock.

4.A.2.4 Producing mould: Defining flow channels

Timing 2.5 hr

1. Place wafer on horizontal surface and pour on enough SU8 2050 to cover ~90 % of the wafer. Avoid SU8 flowing over the wafer edge and as this will cause it to stick to the spinner, hotplates etc. Pouring the SU8 as apprise to using a pipette minimises the number of air bubbles, and a zig-zag pouring approach is also helpful. The majority of bubbles that do form should be removed before spinning, many of which can be done so using a pipette. PAUSE POINT Let the wafer stand for 15 mins to allow the remaining bubbles to rise to the surface.

2. Spin the wafer at 500 rpm for 30 s and 1000 rpm for 60 s to produce a 165 µm thick layer.

3. Pre-expose bake: 6 mins at 65°C and 45 mins at 95°C. PAUSE POINT Allow to cool gently after the bake so as not to induce thermal shock. TROUBLESHOOTING Once the wafer has cooled, touching the surface softly on one corner with a pair of tweezers should not leave a mark or penetrate the SU8

layer. Re-ramp the wafer back to 95°C for 10 minutes longer and recheck before proceeding to the next step if this is not the case.

4. Expose wafer to flow channel photomask in mask aligner with 600 $mJcm^{-2}$.

5. Post-expose bake: 5 mins at 65°C and 30 mins at 95°C. PAUSE POINT Allow to cool gently so as not to induce thermal shock. TROUBLESHOOTING: SU8 may become patchy if the pre- and post-exposure baking temperatures are different from those suggested or the hotplates do not produce a constant temperature across the entire sample.

4.A.2.5 Producing mould: Development

Timing 15 mins

1. Immerse wafer in EC solvent and gently agitate for 9 mins or until the majority of unexposed SU8 2050 has been dissolved.

2. Replace EC solvent and agitate for 30 seconds.

3. Rinse wafer in IPA and dry with nitrogen gun.

TROUBLESHOOTING If mould has white powdery film then SU8 has not been fully dissolved and should be re-immersed in EC solvent for 30 seconds or until clear.

TROUBLESHOOTING If the SU8 channels are wider than those in the photomask then the mold has been over-exposed. This should not normally be a problem but can be avoided by reducing the exposure time to the photomask in a future attempt.

TROUBLESHOOTING Under-exposing the photomask will result in lack of adhesion of the SU8 flow channel ridges. If this occurs the process must be repeated, with a longer exposure time. A short post-bake will also reduce adhesion. Persisting problems could indicate organic contaminants on the silicon wafer, see Section 3.3.3 for details.

4.A.2.6 Strengthening steps

Timing 3 hr

1. The use of NOA can be very beneficial in ensuring the fibre remains attached to the mould during use. Place a small amount of adhesive in small areas between the channels as indicated in Figure 4.A.4, such to connect the fibre and substrate, before immediate exposure to 4000 $mJcm^{-2}$ or until set.

2. A hard bake at 180^oC for a few hours will improve the overall strength of the mould. The mould should be warmed via 3 mins at 65^oC and 10 mins 95^oC using the hotplates to avoid thermal shock.

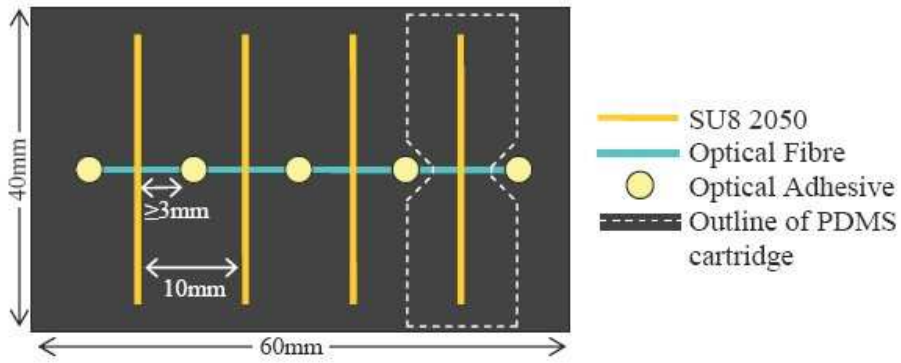

Figure 4.A.4: *Plan view layout of finished fibre trap aligner mold, including outline of one of four PDMS cartridges molded with each use*

4.A.2.7 Silanisation of the mould

Timing 1 hr

1. Place two small drops of trichlorosilane (see Section 3.2.3.4 for details) onto a filter paper using a pipette and place in the desiccator.

2. Place mould in the desiccator and evacuate for 1 hr.

4.A.3 Moulding and bonding of the PDMS Chip

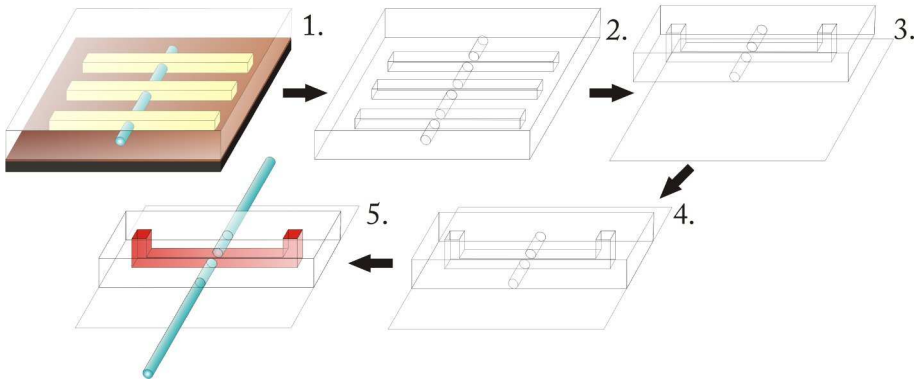

Figure 4.A.5: *Fabrication steps for rapid replication of PDMS fibre trap alignment cartridge from mould – 1) Cover mould in PDMS and cure in oven 2) Peel cured PDMS away from mold 3) Cut PDMS into individual devices and cut fluid inlets/outlets 4) Expose PDMS and coverslip to oxygen plasma and bring surfaces into contact to permanently bond 5) Insert optical fibres and add fluid inlet/outlets pipes*

Timing 3 hr

1. Mix 20 ml of PDMS (Sylgard 184) pre-polymer base and 2.6 ml of curer and mix thoroughly.

2. Degas under a vacuum for 20 mins or until clear. Any bubbles remaining should be removed by drawing into a pipette.

3. Place mould in a 10 cm diameter plastic Petri dish.

4. Pour PDMS over mould. The introduction of bubbles should be minimised and can be removed using a pipette.

5. Cure at 65°C for 2 hr.

6. Carefully peel PDMS from mold and cut into four devices with shape indicated in Figure 4.A.4 using a scalpel blade. CRITICAL STEP One should pay attention to keep the channel side of the PDMS clean.

7. Punch 1.2 mm inlet holes through the PDMS for fluid insertion at the end of the flow channels using a Harris Micropunch. For tubing sizes other than 1.59 mm (1/16 inches) one should use a different punch size, and a fraction smaller than the tubing diameter such to from a good seal.

8. Place PDMS chip channel-side up on an insulating surface (such as the Petri dish lid) along with a suitably sized coverglass. Evenly expose both the PDMS channel-side surface and the coverslip to ~10 sec of plasma using a hand-held corona treater.

9. Immediately rinse both surfaces in methanol, place into conformal contact such that the PDMS chip is placed channel-side down onto the coverglass. Place in the oven to bond for 4 hr or overnight.

4.A.3.1 Insertion of the optical fibre

Once fully bonded, the chip ready for use and may be autoclaved if required. For the insertion of optical fibre, the chip should be positioned on the microscope stage. Alternatively, a stereo inspection scope can be used for this process. Coupling of the laser into the fibres should be conducted prior to insertion into the chip. Place a few drops of methanol on the fibre inlet and gently slide a cleaved fibre into the channel to the desired fibre separation location. This can then be repeated with the second fibre. A few sections of sticky tape will prevent the fibres from sliding out whilst the methanol is drying. One should wait at least 1 hour before use to ensure the methanol has fully evaporated, which is essential in forming a seal with the surrounding PDMS to prevent leaks.

Chapter 5

Optical Sorting of Microparticles using Evanescent Fields Generated by a Total Internal Reflection Objective Lens

An array of techniques for fractionating microscopic particles such as cells were reviewed in Section 1.4 and the details of another were given in the last chapter. In this chapter, a new technique for optically deflecting and passively sorting micron-sized particles in a near-field optical geometry is studied theoretically and demonstrated experimentally. By focusing a small collimated laser beam, positioned off-axis at the back aperture of a total internal reflection fluorescence (TIR) microscope objective lens, an evanescent field is generated at the glass/water interface of a sample chamber. Asymmetrical gradient and scattering forces from this light field are seen to deflect microparticles along the interface, and with velocities dependent upon their intrinsic optical properties.

The chapter starts by reviewing the physical phenomena of total internal reflection and the subsequent generation of an evanescent field in the near-field. Several techniques for generating evanescent waves for the purpose of optical manipulation are reviewed, including the use of a TIR objective lens, as used here. The optical setup that was used is detailed, before making some theoretical predictions from

Figure 5.1: *An image of this diver is visible on the surface of the water due to total internal reflection (TIR). Light rays incident at steep angles on the air-water boundary are unable to propagate across the boundary and instead bounce off due to TIR.* [207]

a finite element method model which was used to calculate the optical forces on dielectric microspheres within the vicinity of the evanescent waves. The experimental guiding velocities of polymer and silica microparticles was then measured and characterised. Based on the model and the experimental observations, the technique was applied to optical sorting in a microfluidic chip, where the evanescent optical field was used to passively sort particles according to their intrinsic optical properties.

5.1 Total Internal Reflection

Upon incidence on an interface between two dielectrics of differing refractive indices, an optical ray will be refracted, reflected or normally a combination of the two depending on the angle of incidence, as shown schematically in Figure 5.2.

For a ray encountering a material of differing refractive index, the ray will be split into a refracted and a reflected beam, whose intensities can be determined by

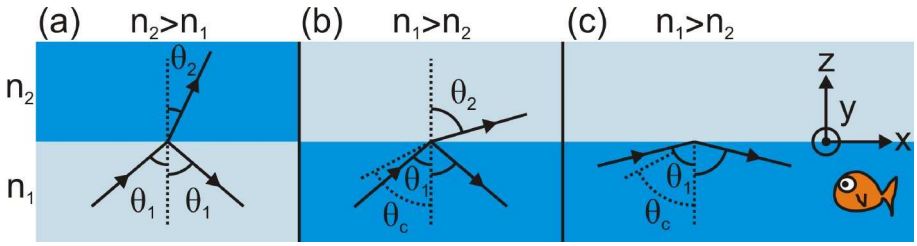

Figure 5.2: *Reflection and refraction of a light ray incident upon a boundary of higher (a) and lower (b, c) refractive index. The ray is refracted towards and away from the plane normal in (a) and (b) respectively. For (c) the angle is greater than the critical angle θ_c for total internal reflection and thus a refracted ray does not penetrate into n_2.*

the Fresnel equations and the angles by Snell's law [22]:

$$n_1 sin\theta_1 = n_2 sin\theta_2 \tag{5.1}$$

where n_1 and n_2 are the refractive indices in the two materials, θ_1 and θ_2 the angles of propagation before and after incidence respectively with respect to the surface normal. Hence, for a ray starting in the less refractive material, the refracted ray is bent towards the normal as it crosses the interface ($\theta_2 < \theta_1$) and the reflected ray is unchanged in angle. However, the situation becomes more interesting when the ray starts in the higher refracting index, where the ray is refracted away from the normal. As one increases the angle of incidence a *critical angle* θ_c is reached, at the point where the ray has refracted so far that it becomes parallel to the interface.

$$\theta_1 = sin^{-1}\left(\frac{n_2}{n_1}\right) \equiv \theta_c \tag{5.2}$$

Any further increase above this critical angle results in the ray being entirely reflected and as such is prevented from propagating across the boundary, known as total internal reflection (TIR). Figure 5.3 shows a laser beam confined to a high index material (PMMA, $n_1 = 1.49$) in a lower index surrounding (air, $n_2 = 1.00$) due to TIR.

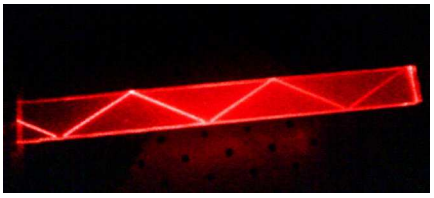

Figure 5.3: *Total internal reflection is commonly used for confining light to a waveguide, such as in optical fibres that contain a high index core surrounded by a lower index cladding. Here a helium neon (HeNe) laser beam at 633 nm is confined to the block of PMMA due to the angle of incidence at the walls being above the critical angle for total internal reflection, forcing the light to continue bouncing along the waveguide.* [208]

5.2 Evanescent Waves

There exists a subtlety with total internal reflection. The optical field cannot simply be the full intensity of the incident ray at one side of the interface (n_1), whilst being simultaneously zero on the other (n_2). This requirement for continuity is satisfied by the suitably termed *evanescent* or boundary field, which is a portion of light that exponentially decays with increasing distance z into the medium of lower refractive index [209]

$$I(z) = I_0 e^{-z/z_p} \tag{5.3}$$

and in effect represents the partial emergence of the incident beam into the less refracting medium. Over an optical cycle however, there is zero net energy flux across the boundary. The penetration depth, z_p of this field away from the boundary (defined by the 1/e electric field amplitude) is a function of the incident angle

$$z_p = \frac{\lambda}{2\pi\sqrt{n_1^2 sin^2\theta_1 - n_2^2}} \tag{5.4}$$

where λ is the wavelength in a vacuum [210] and is plotted as a function of angle in Figure 5.4, for the experimental parameters of $n_1 = 1.515$, $n_2 = 1.33$ and $\lambda = 1070$ nm, showing a critical angle of $\theta_c = 61.4^o$. Below the critical angle the penetration depth is infinite as a refracted ray propagates across the boundary. The value becomes finite and maximal exactly on the critical angle, and it decreases exponentially as the angle is increased beyond θ_c. Therefore for maximum interaction of the evanescent field with particles in the second medium, it is desirable to operate at or

close to θ_c.

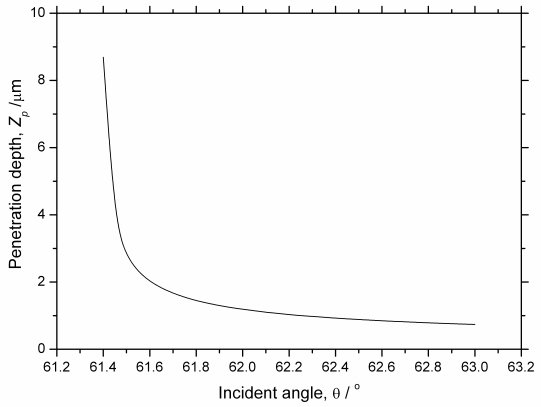

Figure 5.4: *Penetration depth of the evanescent field as a function of incident angle at the interface between glass* $n_1 = 1.515$ *and water* $n_2 = 1.33$ *for* $\lambda = 1070$ *nm. Below the critical angle of* 61.4^o *the field propagates across the boundary. Maximum overlap of the evanescent field with the lower index medium occurs on the critical angle.*

The intensity of the evanescent field at the boundary can be shown to also be a function of the incident angle [211]. The p (TE) and s (TM) polarised electric fields may respectively be expressed as

$$\mathbf{E}_p = E_x\mathbf{e}_x + E_z\mathbf{e}_z \qquad and \qquad \mathbf{E}_s = E_y\mathbf{e}_y \tag{5.5}$$

where $E_{x,y,z}$ is the amplitude in the $\mathbf{e}_{x,y,z}$ directions as defined in Figure 5.2. Omitting the x and time dependence [210], the $z = 0$ electric field amplitudes are [211]

$$E_x = \frac{2cos\theta\sqrt{sin^2\theta - n^2}}{n^4cos^2\theta + sin^2\theta - n^2}\, E_p^i\, e^{-j(\delta_p+\pi/2)} \tag{5.6}$$

$$E_y = \frac{2cos\theta}{\sqrt{1-n^2}}\, E_s^i\, e^{-j\delta_s} \tag{5.7}$$

$$E_z = \frac{2cos\theta sin^2\theta}{n^4cos^2\theta + sin^2\theta - n^2}\, E_p^i\, e^{-j\delta_p} \tag{5.8}$$

where $j = \sqrt{-1}$, $n = n_2/n_1$, $E_{p,s}^i$are the incident plane wave amplitudes and the

phase factors δ_p and δ_s are solutions to

$$tan\delta_p = \frac{\sqrt{sin^2\theta - n^2}}{n^2 cos\theta} \qquad and \qquad tan\delta_s = \frac{\sqrt{sin^2\theta - n^2}}{cos\theta} \tag{5.9}$$

The field intensity $I_0 \propto (E_{p,s})^2$can be calculated for the two polarisations, and is plotted in Figure 5.5 for the experimental parameters. Interesting, a five-fold enhancement in the intensity occurs at the critical angle, and notably also a dependence on the polarisation state of the incident field can be observed. It is also interesting to note that for the s polarised field, the electric field is transverse to the propagation direction $(+x)$ and that for the p polarised field, the x and z components are $\pi/2$ out of phase causing the electric field vector to "cartwheel" along in the direction of propagation (see Figure 5.6).

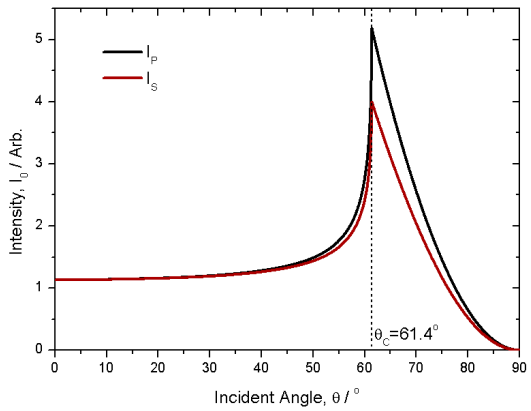

Figure 5.5: *Intensity I_0 at the interface between media of $n_1 = 1.515$ and $n_2 = 1.33$ as a function of incident angle θ for p and s polarisations. A clear enhancement of the field I_0 occurs at and surrounding the critical angle θ_c.*

The phase factors $\delta_{p,s}$ give rise to a lateral shift between the incident and reflected beams known as the Goos-Hänchen shift. Effectively, the incident beam partially emerges in the lower refracting medium, travels some finite distance (the Goos-Hänchen shift), before re-entering the first medium. The size of the Goos-Hänchen shift ranges from a fraction of a wavelength at $\theta = 90^o$, to an infinite distance at θ_c at the point the refracted beam emerges parallel to the interface [211]. The result of the Goos-Hänchen shift is that the reflected beam is displaced with respect to the incident beam, despite the apparent fact that total reflection of the beam has

occured.

The evanescent field carries momentum in the $+x$ direction of propagation and as shall be seen in Section 5.5, can be transferred to microparticles residing in the field, for optical trapping or guiding.

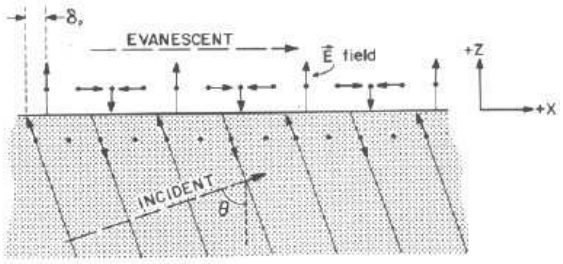

Figure 5.6: *Electric field vectors at $z = 0$ of an incident p-polarised plane wave and the associated evanescent wave. The phase lag δ_p gives rise to the Goos-Hänchen shift and is dependent upon the angle of incidence. For the p-polarised wave, the electric field "cartwheels" along the boundary interface* [211].

5.3 TIR Microscope Objective Lens for Evanescent Wave Generation

As detailed in Section 1.3.2, there are several methods for generating evanescent fields within microfluidic environments, including through TIR in prisms in the Kretschmann geometry and on the surface of optical waveguides. In the work in this chapter however, a TIR microscope objective lens was utilised, for simultaneous generation of focused evanescent waves and imaging of the microparticles within these fields.

The traditional use of TIR microscope objective lenses is in fluorescence imaging applications, where the objective is used to focus an excitation beam to generate fluorescence within a very confined region (typically sub-micron) above the coverslip [212]. This functionality is of course in addition to it fully functioning as a standard brightfield lens. Figure 5.7a-b shows a comparison of epi- and TIR-fluorescence microscopy, clearly demonstrating how the fluorescence generation can be limited to a small region. By eliminating fluorescence generation from the bulk sample, excellent signal-to-noise ratios can be obtained, proving highly advantageous in many

Objective lens	Nikon CFI Apo TIRF 100x Oil
Numerical aperture, NA	1.49
Working distance, WD	0.12 mm
Immersion oil refractive index, n_1	1.515
Back aperture diameter, BA	7.9 mm
Maximum obtainable angle at sample, θ_{max}	79.6^o (Eq. 5.10)
Focal length, f	4.02 mm (Eq. 5.12)
Critical TIR back aperture radius, r_c	3.53 mm (Eq. 5.11)
Maximum back aperture beam diameter	$\frac{BA}{2} - r_c = 0.42\,mm$

Table 5.1: *Parameters for evanescent generation with a TIR objective lens*

applications including exciting single molecules [213], individual quantum dots [214], and the visualisation of key trafficking events across the cellular membrane [215]. Evanescent illumination has the added advantages of minimising photodamage in biological samples and reducing photobleaching [213].

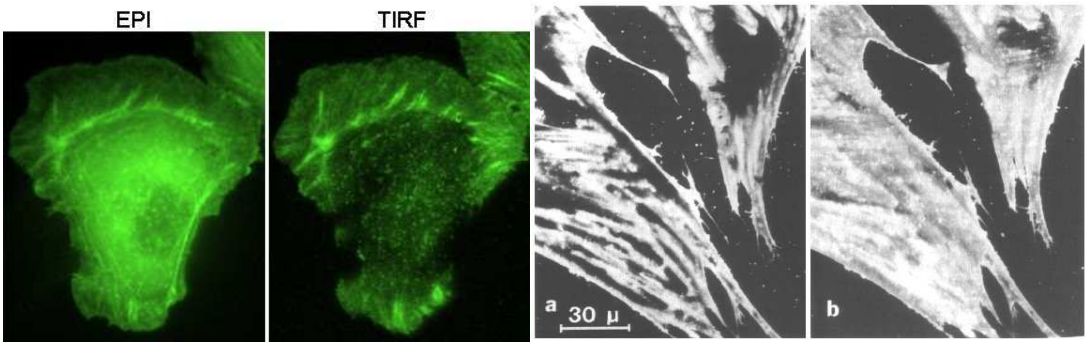

Figure 5.7: *(a-b)* [216] *Comparison of the excitation of GFP in MTLn3 cells using standard epi-fluorescence and TIRF. TIRF microscopy (a) enables the structure within the first 100 nm of the cell to be imaged without exciting background fluorescence in the rest of the cell, such as in epi-fluorescence (b). (c-d)* [211] *The angle of incidence determines the depth of excitation in TIRF microscopy. Here, labelled human skin fibroblasts are illuminated at two difference angles, of (c)* $\theta = 74.3^o$, $d = 105nm$ *and (d)* $\theta = 67.9^o$, $d = 406nm$ *for a setup of* $\theta_c = 67.5^o$.

A TIR lens exhibits the largest of all numerical apertures (NA) commercially available, such as the Nikon CFI Apo TIRF 100x (see Table 5.1) used in the following experimental section that has an exceptionally high NA of 1.49. For an immersion oil and coverslip refractive index $n_1 = 1.515$, the maximum obtainable angle θ_{max} can be found through

$$NA = n_1\, sin\theta_{max} \tag{5.10}$$

yielding $\theta_{max} = 79.6^o$ that is well in excess of the critical angle $\theta_c = 61.4^o$ for a glass-water interface and thus fully capable of generating evanescent fields through TIR in such a sample. It is interesting to note that the minimum NA required to reach the critical angle is $NA_c = 1.33$ for these refractive indices.

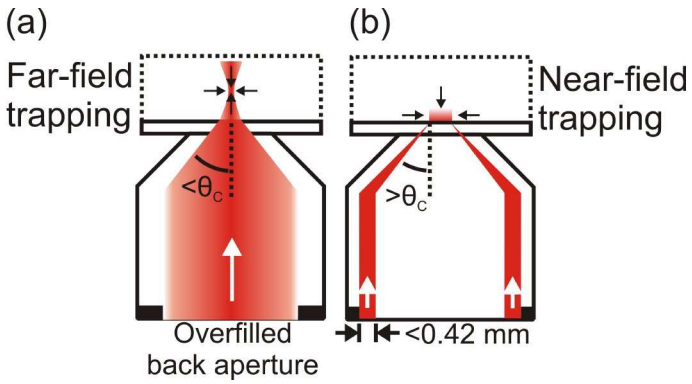

Figure 5.8: *Back aperture illuminations of an objective lens for far-field and near-field optical trapping. (a) Standard optical tweezers setup, where the NA is high ($NA > 1.2$) but is not capable of obtaining evanescent excitation ($NA < NA_c$). The back aperture is overfilled, generating the smallest possible near-diffraction-limited focal spot in the far field. (b) A TIRF objective is employed with larger NA (e.g. $NA = 1.49$) allowing evanescent excitation.*

The minimum size of the back aperture obstruction can be calculated by assuming the Sine condition [217] that relates the radial distance, r from the centre of the back aperture to the angle of incidence, θ at the sample plane

$$r = f\, sin\theta \tag{5.11}$$

where f is the focal length of the objective lens (i.e. distance from the back aperture to the focal point in the sample plane) [218]. Using 5.10, the focal length for a given objective with a known back aperture diameter, BA and NA can be found from

$$f = \frac{(BA/2)\, n_1}{NA} \tag{5.12}$$

Thus, the critical back aperture radius for TIR at the sample, r_c can be calculated for a given θ_c, yielding 3.53 mm for the Nikon NA 1.49 TIRF. This leaves a 0.42 mm wide ring around the outer edge of the back aperture that can be utilised for evanescent illumination. For evanescent trapping the entirety of this ring is illuminated to produce a uniform confined near-field focal spot. In the following

section, a 0.41±0.01 *mm* diameter ($1/e^2$) Gaussian beam is positioned within this ring producing an evanescent field in the focal plane, and its use for guiding microparticles across the coverslip surface is demonstrated, characterised and employed for passive optical sorting.

5.4 Experimental Setup

5.4.1 Optical Setup

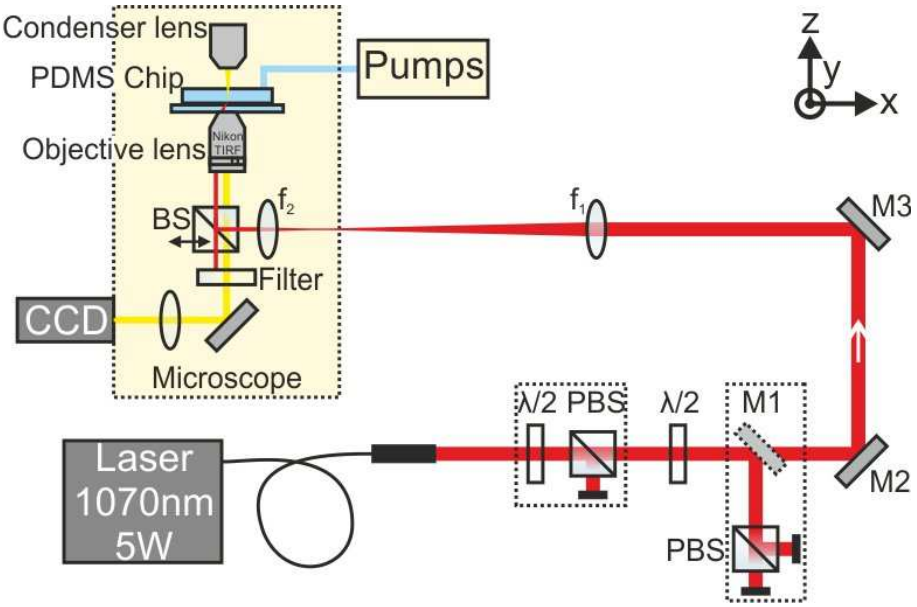

Figure 5.9: *Optical setup for generation of evanescent guiding using TIRF objective lens in Nikon TE2000-E microscope. The setup incorporated a halfwave plate ($\lambda/2$) and polarising beamsplitter (PBS) for attenuating the beam, a $\lambda/2$ for selecting the polarisation at the sample and a flip-mirror (M1) and PBS to verify the polarisation. A periscope (mirrors M2 and M3) sent the beam into the microscope, which was demagnified to 0.4 mm using positive lenses f_1 and f_2. The beamsplitter (BS) was mounted on a translation stage, allowing the beam to be moved across the back aperture of the TIRF objective lens whilst maintaining a normal angle of incidence. The evanescent focused beam was formed in the PDMS microfluidic chip as shown, or in sample chamber. The sample was imaged using the TIRF objective onto a CCD camera with bright-field illumination from above the sample.*

The optical setup used is shown in Figure 5.9. In order to obtain a purely evanescent illumination at the sample focus using a TIRF objective, one ensures that only the outer extremity of the back aperture is illuminated, such that all rays at the sample plane exhibit $\theta > \theta_c$. To obtain the maximum control over the beam

illuminating the back aperture, an adapted optical tweezers setup was constructed to include a telescope to relay a steering mirror, enabling the angle of the beam at the back aperture to be controlled. A commercial Nikon TE2000-E microscope was used for the experiments, with the filter wheel removed and replaced with a beamsplitter (50:50). The beamsplitter was mounted on an *xyz* positioning stage, allowing the reflected beam to be precisely positioned anywhere on the back aperture, without adjusting its angle. Figure 5.10 shows schematically the effect at the sample of translating the beam across the back aperture.

The relay telescope ($f_1 = +750\ mm$, $f_2 = +160\ mm$) also demagnified the beam from the laser output size of 1.6 mm to a $1/e^2$ diameter of $0.41 \pm 0.01\ mm$, which was measured using a beam profile. The collimation at the back aperture was also verified using a beam profiler. The size of this "beamlet" is within the constraints put forward in Table 5.1 for purely evanescent illumination.

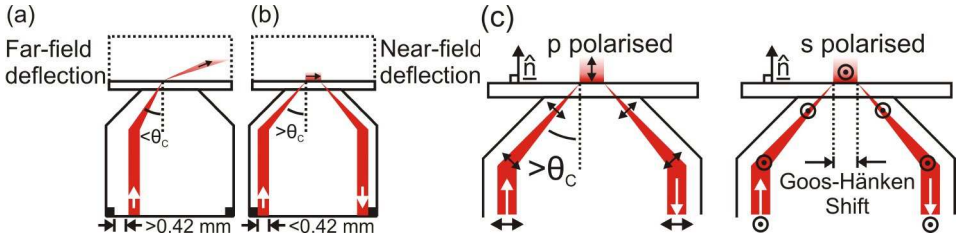

Figure 5.10: *Schematic of the back aperture beam position on obtaining far-field (a) and near-field (b) illumination in the sample plane by translating the position of the collimated "beamlet" across the back aperture of the TIR objective lens. (c) Definitions of p- and s-polarised evanescent illuminations for the optical setup.*

The laser source was an IPG Photonics, $\lambda = 1070\ nm$, 5 W output power, fibre laser with a collimating head and optical isolator. The sample was illuminated with incoherent light through a high-NA condenser, imaged using the TIR objective and captured by a high frame-rate camera on one of the camera ports of the microscope. The alignment procedure consisted of first centring the beam in the back aperture and adjusting the steering mirrors to couple the beam into the high-NA condenser above the TIRF. The beam was then focused onto a glass slide and the steering mirrors M2 and M3 were adjusted to make the Airy pattern fully symmetric. The beamsplitter BS was then translated in the y-direction (see Figure 5.9), the one of three possible directions that should not translate the beam. The tilt of the BS was

adjusted until the beam as observed on the CCD was unaffected by the translation of the BS in the y-direction. The beamlet was then translated in the -x-direction to position it at the edge of the back aperture.

5.4.2 Sample Preparation

Colloidal samples were prepared immediately before measurement taking. The sample chamber in shown schematically in Figure 5.11. A common problem was the colloids attaching themselves to the coverslip, preventing them from being guiding by the evanescent field. The was largely evaded by mixing in a trace amount of sodium dodecyl sulphate (SDS) surfactant and subjecting the colloid solution to a sonic bath prior to use. In work post this experiment it has been noted that subjecting the coverslips to an oxygen plasma immediately before preparation is useful in ensuring that the colloids do not stick to the glass surface, but it is unknown as to the effect on glass-colloid separation and thus the effect on evanescent guiding of this technique.

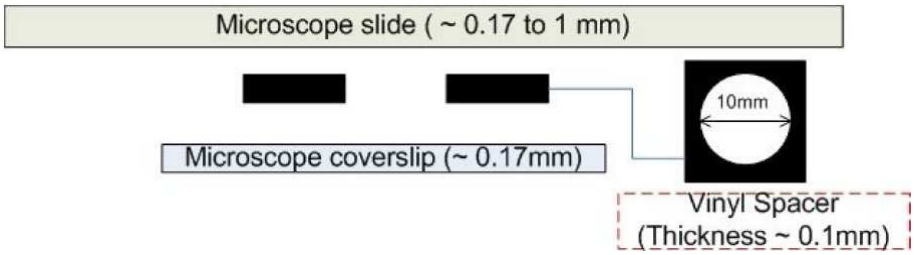

Figure 5.11: *Side and top view of a sample chamber containing colloids suspended in water, consisting of a glass coverslip, a vinyl spacer and a glass slide or coverslip. The vinyl spacer was attached to the glass slide, a sample volume of* 20 μl *was pipetted into the centre of the spacer and the coverslip was placed on top to complete the chamber. The edges of the chamber were sealed in nail varnish to prevent evaporation or leakage of the sample.* [4]

5.4.3 Transmission Measurement of the Objective

In order to ascertain the available power for forming an evanescent wave for a given back aperture illumination, it was necessary to measure the transmission of the objective lens. Ideally, a dual objective measurement would have been conducted, where two identical objectives are used and the optical field focused by one into a

sample is collected by the other. The square root of the overall power loss gives the transmission of a single objective which encompasses the transmission of the lens, the immersion oil and the Fresnel losses into the sample. This standard method had to be adapted as only a single lens was available.

The 50:50 beamsplitter (see Figure 5.9) beneath the objective split the beam into two, one half that was incident upon the back aperture, and the other half giving a location for measurement of the power at the back aperture. A dielectric high reflecting mirror was placed on top of the objective and index matched with immersion oil. The beamsplitter was positioned to place the beamlet close to the edge of the back aperture, which passed through the objective, reflected off the mirror, made a second pass of the objective re-emerging on the opposite side of the back aperture, and was again split into two by the beam splitter. Therefore, the power emerging from beneath the beamsplitter, compared to that incident on the back aperture, gave a transmission measurement of two passes of the objective.

Separately, the reflectivity of the mirror as a function of angle was verified, and the beamsplitter was characterised to ensure a 50:50 split. The objective's transmission was measured for several positions close to the extremity of the back aperture and was found to be $77 \pm 1\%$ for 1070 nm laser irradiation.

5.4.4 Measurement of the Incident Angle

Four methods were used to correctly position the beamlet at the back aperture for optimum evanescent guiding. First, the position of the beamlet on the back aperture was observed with a handheld IR viewer to allow crude positioning of the beamlet. Secondly, the intensity of the reflected beam from a colloidal sample was observed with the IR viewer and maximised, thus ensuring TIR at the sample. Thirdly, the movement of the colloids in the beam was observed and the beamlet positioned so as to maximise the velocity of the colloids but without any lift of the colloids from the surface (indicating the presence of far-field components). Finally, the image of the now elliptical beam was captured by CCD camera (as shown in Figure 5.12) and the lengths of the two axes measured, enabling the incident angle to be calculated. As the incident angle θ is increased for a beam of radius w_0, it stretches along the

angled axis to form an ellipse at the interface. The stretched axis will have a radius of [61]

$$w_0' = w_0 \, cos\theta \tag{5.13}$$

which allows the angle θ to be calculated for a given captured beam profile. The beam profile was also captured at different heights (as measured using the readout on the microscope digital display for the objective height), causing the beam to traverse across the field of view. This gave another calculation method for the incident angle, thus verifying equation 5.13.

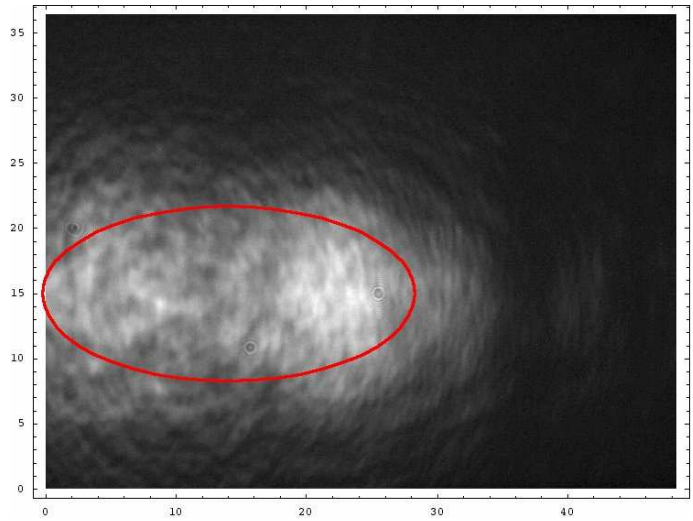

Figure 5.12: *Comparison between the experimentally observed beam profile and the* $1/e^2$ *beam waist (in red) of a Gaussian beam incident at* 61^o*. The units on the* $x-$ *and* $y-$*axis are* μm *and in normal incidence the Gaussian beam has a diameter of 13.4* μm*.* [3]

5.5 Theoretical Model

The interaction of the evanescent field with microparticles within the field was modelled numerically using Comsol software. Firstly, the experimentally observed beam profile was used to generate an expression for the optical field. The optical force on a microparticle in the evanescent field was then calculated using the Maxwell stress tensor formalism and its associated force density [219, 220]. A value for the particle velocity due to the field was then calculated, and the microfluidic effects were treated using a wall corrected Stokes drag coefficient. The numerical simulation uses a

fully vectorial finite element method which is validated against existing literature.

5.5.1 Modelling the Optical Field

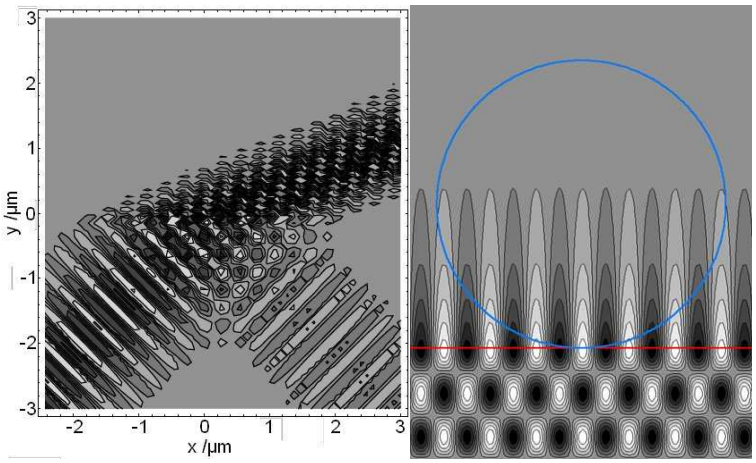

Figure 5.13: *(a) Electric field map of the combined decomposed incident fields, at* 45^o *in the* $+x$ *direction on the glass-water interface at* $x = y = 0$*, undergoing refraction and reflection. (b) Electric field for* $\theta = 61^o$ *with the boundary shown in red and the position of a 5* μm *sphere placed on* $x = y = 0$ *marked in blue. The interaction between the sphere and the optical field is not considered for this Figure.* [3]

The beam considered in the simulation was a fully vectorial linearly polarised Gaussian beam in the first order of development [221]. By capturing the back reflection of the beam, as the height of the water glass interface was changed, the angle of incidence was estimated to be approximately 61^o, as depicted in Figure 5.12. Unfortunately, due to optical distortions and multiple reflections the intensity profile lost its perfect Gaussian shape. The beam was therefore decomposed into a minimal set of plane waves for which analytically the complex transmission and reflection coefficients at the water glass interface were calculated. The superposition of these plane waves enabled a single incident field to be treated analytically that included the incoming, the reflected and the evanescent parts (see Figure 5.13). The beam was modeled as the minimal angular spectral decomposition of the incoming beam and the unit angle between two plane waves, within this spread, is given by the far-field divergence angle of the Gaussian beam. Thus, calculations were conducted for each of the plane waves individually and summed to produce the overall result. The angle of incidence herein is the median angle for the angular spread of the nine

plane waves required to produce the beam profile observed in Figure 5.12. The Goos-Hänchen shift was observed to be a function of incident angle and is plotted in Figure 5.14.

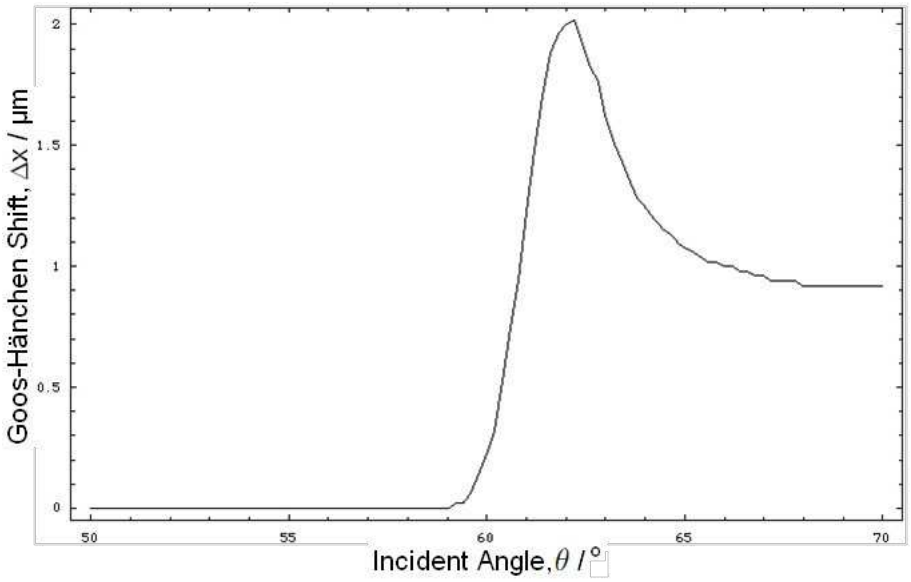

Figure 5.14: *Magnitude of the Goos-Hänchen shift as a function of incident angle for the decomposed beam used in the model. Here, the x position relative to the beam incident at $x = 0$, of the Gaussian-shaped intensity maximum is plotted.*

5.5.2 Optical Forces on Particles in the Field

A finite element method software package *Comsol* was used to calculate the scattered electric and magnetic fields. For simplicity, a negligible power loss was assumed for the optical system after emerging from the objective lens. Additionally, it was assumed that the water–glass interface corresponded to the focal plane of the Gaussian beam. Figure 5.15 shows the electric field distribution incident on a sphere placed on the interface at two angles of incidence.

5.5.2.1 Maxwell Stress Tensor

To evaluate the optical force acting on particles in the optical field, the Maxwell stress tensor was calculated and integrated across the surface of the particle. In a

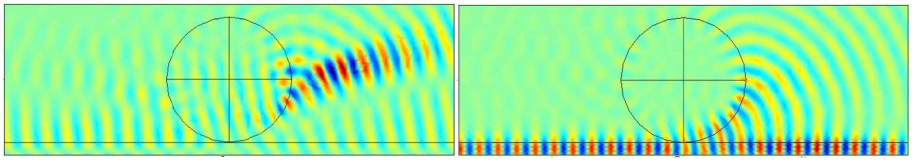

Figure 5.15: [3] *Electric field distribution incident on a 5 μm polystyrene sphere in water, for angles of incidence of* 61^o *and* 70^o *respectively. At the critical angle the large portion is coupled out of the evanescent field into a propagating beam into the fluid medium and thus exerts a large gradient force on the sphere towards the substrate. The incidence angle of* 70^o *is interesting as the field is close to forming a whispering gallery mode and could indeed be possible by suitable choice of wavelength and sphere size, as utilised by Kuriakose* et al. [78].

host material the stress-tensor $\overline{\overline{T}}$ is given by [219, 220]

$$\overline{\overline{T}} = \vec{D} \times \vec{E}^* + \vec{B} \times \vec{H}^* - \frac{1}{2}\left(\vec{D} \cdot \vec{E}^* + \vec{B} \cdot \vec{H}^*\right) \tag{5.14}$$

with $\overrightarrow{E}$, $\overrightarrow{D}$, $\overrightarrow{H}$ and $\overrightarrow{B}$ denoting the electric field, the electric displacement, the magnetic field and magnetic flux respectively, and * is the complex conjugate. Applying the constitutive relations $\vec{D} = \varepsilon_r \varepsilon_0 \overrightarrow{E}$ and $\vec{B} = \mu_r \mu_0 \overrightarrow{H}$, where ε_r, ε_0, μ_r and μ_0 are the relative and vacuum permittivity and permeability respectively, the tensor components in SI units are

$$T_{ij} = \varepsilon_r \varepsilon_0 E_i E_j^* + \mu_r \mu_0 H_i H_j^* - \frac{1}{2}\left(\varepsilon_r \varepsilon_0 E_k E_k^* + \mu_r \mu_0 H_k H_k^*\right) \tag{5.15}$$

which is summed over the identical indices k. The optical average force acting on the particle is

$$\left\langle \vec{F} \right\rangle = \frac{1}{2} Re\left(\int_S \overline{\overline{T}} \cdot \vec{n}\, ds\right) \tag{5.16}$$

where n is the normal vector pointing outward to the surface S of the particle. The force was averaged over one optical cycle. Note that, due to the jump in the index of refraction, the normal fields at the surface of the particles have a discontinuity. To calculate the total optical force the external fields were used. In this case, the total force includes not only the optical force on the particle but also the optical force acting on the water interface, which is completely transmitted to the sphere due to the hydrodynamic non-slip boundary conditions at this interface. To

validate the integrated stress tensor approach, it was compared with the integrated force density

$$\left\langle \vec{F} \right\rangle = -\frac{\varepsilon_0}{4} Re \left(\int_V E_k^* E_k \nabla \varepsilon_r \, dv \right) \tag{5.17}$$

where the integral is taken over the volume V of the particle [219]. The permittivity ε_r is constant in the volume of the particle, hence the integrand is only non-zero on the surface of the sphere and the above integral simplifies to a surface integral. Even though analytically both force calculation methods should give identical results, it was observed that this was only the case when the numerical discretisation of the problem has sufficient resolution. This important consideration allowed the validity of the numerical simulation to be verified.

5.5.2.2 Gradient and Guiding Forces

It is beneficial to consider the forces acting on a particle in an evanescent field as two components, a vertical force acting to pull (gradient force) or push (deflection/guiding force) the particle to or from the substrate, and a horizontal force which guides particles along the substrate in the direction of propagation of the evanescent field. The Maxwell stress tensor can be used to calculate the forces acting on an illuminated micro-particle and predict its behaviour; indeed as a function of particle size, refractive indices, and on the effect of polarisation state of the incident field.

To test the robustness of the numerical model, the illustrative example of Almaas and Brevik [222] was chosen for comparative purposes. Their model parameters correspond to a 2 μm glass sphere (n = 1.5) submerged in water (n = 1.33) above a sapphire substrate (n = 1.75) . In this configuration, the critical angle is 51^o and the beam has a power of 150 mW and a 100 μm diameter. This corresponds to a power density of 19 MWm^{-2} and a force coefficient of $\varepsilon_0 E^2 a^2 = 130\, fN$ where a is the radius of the particle. Using these parameters in the model detailed above predicts horizontal guiding forces of $F_{xp} = 11\, fN$ for p-polarisation and $F_{xs} = 8.1\, fN$ for s-polarisation, which compare respectively to 10 fN and 8.1 fN as obtained in [222]. Similarly, the calculation implies particles are pulled towards the substrate with $F_{zp} = -44\, fN$ (p-pol.) and $F_{zs} = -27\, fN$ (s-pol.) which is in good agreement with

the data of Almaas *et al.* (-44 fN and -29 fN) [222].

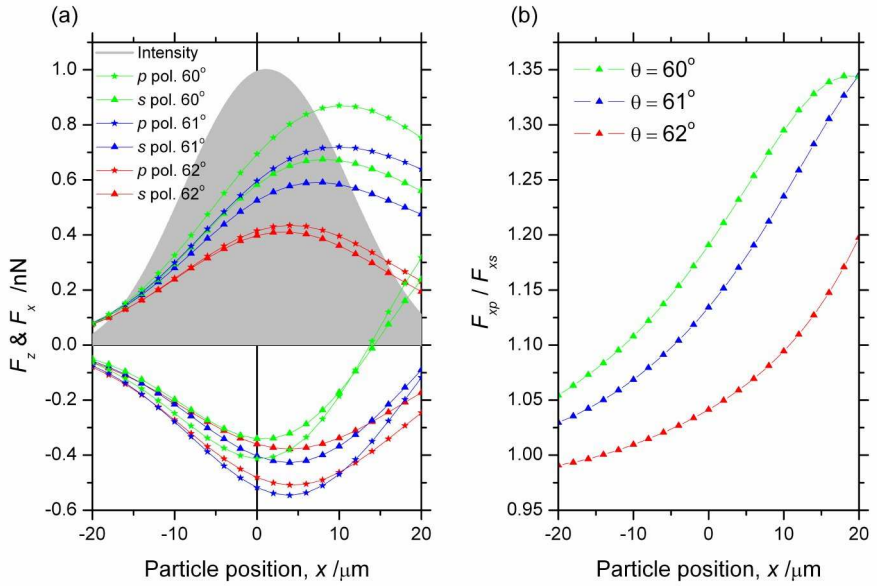

Figure 5.16: *(a) Horizontal (positive range) and vertical (negative range) forces as a function of the particle position with respect to the incoming beam, for different angles of incidence. The greyed region corresponds to the intensity profile of the beam on the interface. Note that its maximum is shifted with respect to the centre of the incident beam due to the Goos-Hänchen shift. (b) Ratio between the horizontal optical forces of the p and s polarisations as a function of the particle position for different angles of incidence.* [3]

Figure 5.16 shows the main result of the simulation for the proceeding experimental section, showing the horizontal and vertical optical forces acting on the particle at different positions along the middle of the TIR beam profile. The same particle size of 5 μm in diameter, in contact with the substrate and for 1 W of optical power was used for comparison with Almaas *et al.* [222]. The spot size using the TIRF is reduced to 13.4 μm (see Figure 5.12) leading to a power density of 10 GWm^{-2} . This system produces a force coefficient $\varepsilon_0 E^2 a^2 = 420\, pN$ which is three thousand times larger than the Almaas *et al.* case. The positive part of the graph shows the horizontal, i.e. guiding forces, while the negative part shows the vertical forces, i.e. the pull/push towards the substrate. The greyed region shows intensity of the TIR beam together with the Goos-Hänchen shift. Further, depending on the angle of incidence, position in the beam and distance from the substrate, a variable ratio between the s and p polarisations can be observed (see Fig. 5.16b).

First of all, using this graph, one can observe a clear shift between the maximum

beam intensity and the maximum force amplitude. This shift, similar to the Goos-Hänchen shift but more pronounced, starts before the critical angle and decreases for angles far beyond the critical angle. A further point of note is the difference in the gradient force profile between the propagation case (green curve, $\theta < \theta_c$) and the evanescent cases (red and blue curves, $\theta > \theta_c$). Indeed, when the beam is mostly propagating, an inversion in the vertical force occurs, which at first pulls and later pushes the particle away from the interface.

The difference in force magnitudes as a function of angle can be observed in Figure 5.17 where the vertical and horizontal forces in the centre of the incident beam as a function of the angle of incidence are plotted. As seen in Figure 5.16, close to the critical angle the propagating beams still attract a particle towards the water glass interface while guiding it very efficiently. In this case the particle acts like a small micro-lens that bends the light away from the interface (see field distribution in 5.15). This in turn, pulls the particle towards the interface, due to momentum conservation, thus enhancing the gradient force already present.

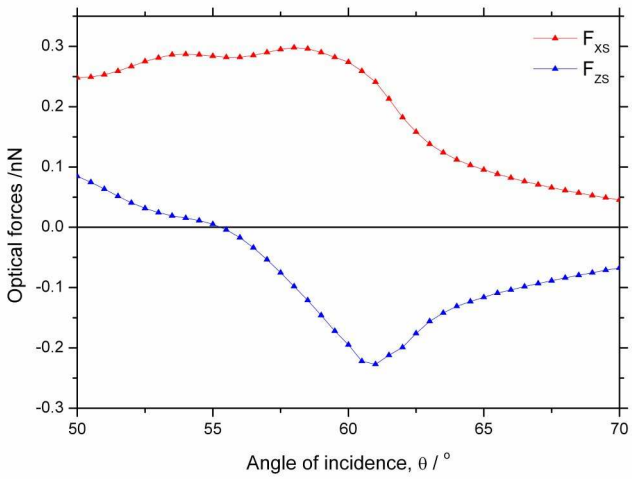

Figure 5.17: *Horizontal and vertical forces as a function of the angle of incidence for a 5 μm particles and an s polarised beam.*

The horizontal guiding forces were also calculated as a function of particle size in the 1 - 5 μm region. Interestingly, the force was found to linearly depend on the size of the particle, as shown in Figure 5.18. This linear relationship has its origin in the relatively large particles considered here and the small refractive index diffe-

rence between the water, the particle and the substrate. Indeed, for high contrast small particles one would expect a complex relationship between guiding forces and particle size [222]. It is on this basis of a predicted linear relationship between the size of a particle and the guiding force that it experiences, for the sizes considered here, that the sorting experiments are conducted in Sections 5.6.2 and 5.6.3

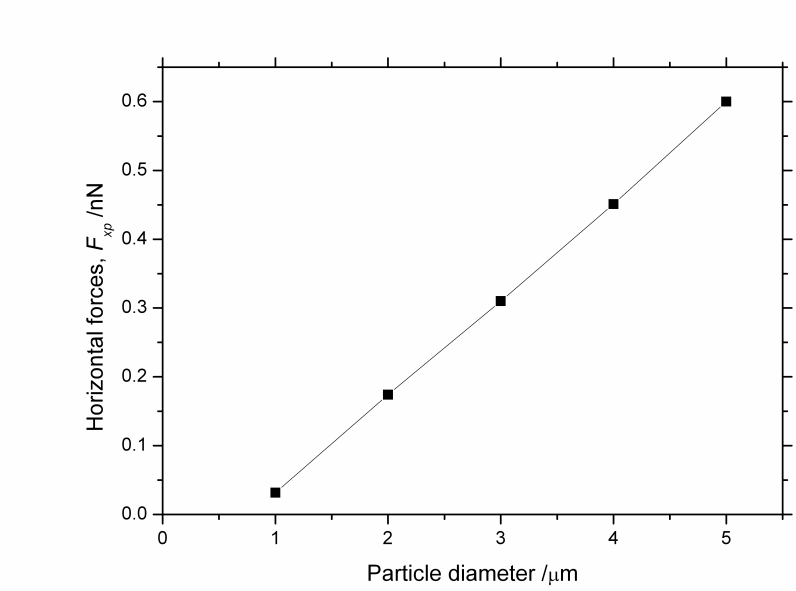

Figure 5.18: *Linear dependence of the horizontal forces for p-polarised centred beam at* $x = 0$ *incident at* $\theta = 61^o$ *as a function of the particle diameter.* [3]

5.5.3 Stokes Drag in Close Proximity to a Boundary

When considering the movement of a particle through a fluid, but in close proximity to a boundary, one cannot simply use the standard bulk Stokes drag force $F = 6\pi\mu av$, where μ is the viscosity, ν the particle velocity and a its radius, but a correction factor has to be implemented. These hydrodynamic corrections were reviewed in Section 2.5.

For large distances ($h > 1.04a$, where h is the distance from the centre of the particle) Goldman *et al.*, [162] showed that the Faxén correction factor (Equation 2.12) deviates less than 10%. Yang *et al.*, [223] have used this correction factor for small particles but for the 2.5 μm particle size, that is considered here, this corresponds to a distance of at least 100 nm. Below this distance or when the

particle is in contact with the substrate one can use the lubrication values of this correction (Equation 2.13) [163] where it is assumed that the particle did not rotate.

Table 5.2 exemplifies these corrections on a centred, 5 μm particle in water with a viscosity $\mu = 8.9 \cdot 10^{-4}\ Pa\,s$. For the particle in contact with the substrate, the hydrodynamic predicted velocities were calculated to be 160 times larger than those experimentally observed and presented in Section 5.6. The origin of this discrepancy could be the various surface effects as described by Brevik *et al.* [224], or the particle floating at a considerable distance from the substrate. When considering angle or distance variations one needs to take into account the variations of the ratio between the *p*- and *s*-polarisation and the shift between the maximal force and maximal intensity. Indeed, these characteristics of the evanescent force change as the particle is moved or the angle of incidence changed. A more complete microfluidic approach would include the particle angular rotation, its surface roughness [225], the buoyancy force, the optical torque, surface friction and the hydrodynamic lift force. The surface roughness could be of particular importance for sorting some cell types, where Hart *et al.* [128] have seen large differences in particles of similar size due to hydrodynamic effects in optical chromatography geometries.

5.6 Experimental Results

In this section, the experimental observations of the behaviour of microparticles in the presence of an evanescent field generated by an off-axis beamlet focused by a TIR objective lens are reported. Particle trajectories were plotted using particle tracking software, velocities calculated and the results compared to theoretical predictions. The velocity was found to be functions of the refractive index and size of the particle, which was characterised for silica and polymer spheres of diameters 1 to 5 μm. Finally, these particle-dependent forces were employed in a microfluidic chip for passive optical sorting of the particles by size in a cross-type chromatography geometry [226] in conjunction with hydrodynamic focusing. Unlike the sorting geometry used by Hart and Terray [127] where particles are separated to points of equilibrium between the opposing optical scattering and fluid flow Stokes force, the

Angle θ / ^{o}	Height h / μm	Vert. force F_z / pN	Horiz. force F_x / pN	Correction factor	Particle velocity V_x / $\mu m s^{-1}$
61	2.51	-400	600	Stokes	14000
				Faxén	4600
				Krishnan	3600
	5.5	-1.0	6.0	Stokes	143
				Faxén	107
70	2.51	-67	45	Stokes	1100
				Faxén	352
				Krishnan	275
	3	-7.5	5.1	Stokes	121
				Faxén	91

Table 5.2: *The effect of the hydrodynamic correction factor on the guiding velocity for a 2.5 μm particle in the evanescent field. The vertical (gradient) and horizontal (guiding) forces are calculated for two angles of incidence and for two heights (interface to centre of particle) of the particle above the substrate. The first is for the particle 100 nm from the substrate, giving a guiding velocity approximately 160 times that experimentally observed. The second height is for one that gives a guiding velocity more closely matched to that observed experimentally. The Faxén and Krishnan correction factors are employed here to take into account the increased Stokes fluid drag close to the substrate, but it is found that a more complete model would be required to fully match the experimental and predicted velocities.*

beam provides an optical force orthogonal to the direction of fluid flow. This is desirable as particles can be continuously separated whilst remaining in continuous flow, allowing different species to be passively flowed into separated fluid channels downstream in the chip.

5.6.1 Evanescent Trapping and Guiding of Particles

Particles in the vicinity of the evanescent field were observed to be attracted to the focal spot and subsequently pulled towards the surface, and guided along in the direction of the wave propagation. Figure 5.19 shows the effect of the field on a sample of red blood cells (RBCs), where they were seen to be pulled into the field and guided along the surface. The biconcave shape of these cells caused them also to rotate onto their sides such to maximise the volume of cell in the field.

A high concentration of microparticles in the sample chamber would cause microparticles to continuously traverse along similar paths, outlining the deflective force vectors and the position of the evanescent field. The dynamic behaviour of colloidal

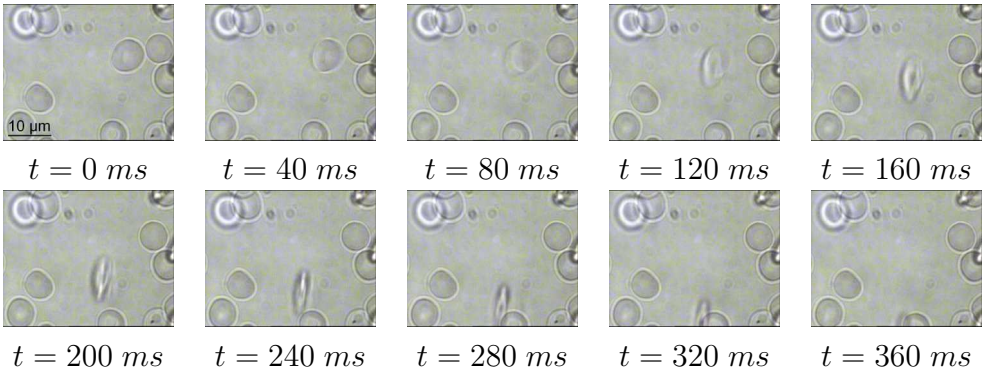

Figure 5.19: *Evanescent guiding of mammalian erythrocytes cells using a TIR objective lens with 1 W illumination at the back aperture. Cells were observed to rotate such that they would align with the direction of propagation their long axis would be perpendicular to the surface.*

particles in the presence of the evanescent field were tracked using LabView particle tracking software [51], an example of which can be seen in Figure 5.20).

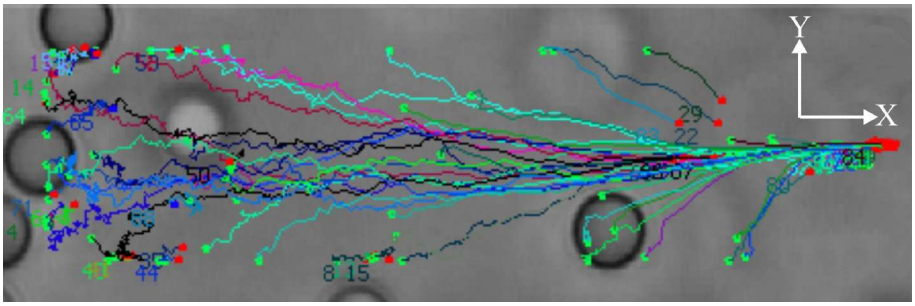

Figure 5.20: *Plotted frame by frame position of 2 µm polymer particles, as calculated over the full duration of a 60 second video using particle tracking software, in the presence of an evanescent field, generated by a TIR objective lens illuminated by an off-axis beamlet. A single frame from the video is shown in the background for reference. The initial position of a single tracked microparticle is indicated by a green spot, the lines show the tracked position over time and the red spot indicates the point at which the particle is lost by the tracking software. Particles are guided by the evanescent wave in the $+x$ direction. By tracking the position of many guided particles, the deflective force vectors of the evanescent field can be visualised.* [3]

5.6.1.1 Particle Tracking Software

To measure the velocities of guided particles, it was necessary to use particle tracking software. An in-house tracker was used, the workings of which are explained in detail in [47] and the software is freely available [51]. Briefly, pattern-matching algorithms in the proprietary NI-Vision plug-in (National Instruments) are utilised in a LabView

program for identifying and tracking the position of an image feature (in this case the brightfield image of a colloidal particle) between frames in a captured video sequence. The software outputs a series of files each corresponding to an individual identified particle and its tracked location in pixels on the camera over the duration of the video. By knowing the conversion of pixels to physical distance (e.g. recording a graticule image) and the video frame rate, the particle positions can be easily converted to velocity. A LabView program was written to convert the tracker files to velocity values, also allowing mean velocities and associated standard error to be calculated as a function of distance across the evanescent spot. An optional region of interest function was included allowing only data for particles that passed directly down the centre of the evanescent spot to be taken into account in the mean calculation.

5.6.1.2 Guiding Velocities of Particles in the Evanescent Field

Figure 5.21 displays the velocity of 5 μm polystyrene spheres as they are guided along the evanescent spot for a range of optical powers and both s and p polarisations. The velocities were divided by the back aperture optical power to normalise the multiple data sets, revealing the associated linear relationship between guiding velocity and optical power. Only spheres that passed directly down the centre of the elliptical evanescent spot ($y = 0$) were taken into account, isolating the guiding purely to the x direction.

In order to average over multiple particles, the velocity measurements were binned into unit microns, with each point being the mean velocity recorded at that location for 6 individual particles. The linearity of velocity with power is verified in Figure 5.22b, showing excellent agreement.

In the region $x < 0$ the microparticles exhibit Brownian motion until trapped against the surface near $x = 0$ due to the gradient forces and accelerated in the positive x direction due to the evanescent field. The particles reach a peak guiding velocity at $x = 21\ \mu m$ before proceeding to decelerate over the remaining 25-30 μm. Interestingly the deceleration is non-uniform with two brief accelerations, seen throughout the data set. Considering the beam profile in Figure 5.12 this is perhaps

(a) (b)

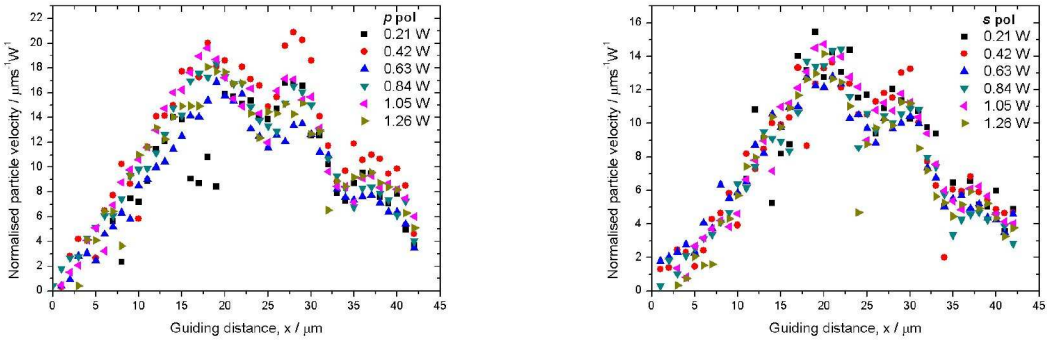

Figure 5.21: *The guiding velocity of 5 μm polystyrene spheres as a function of distance along the evanescent field propagation direction, normalised per unit optical power at the back aperture, for (a) p and (b) s polarised light. The* x*-axis here corresponds to that in Figure 5.12. Points are the average velocity recorded at each unit micron position for 6 individual particles. Standard errors in the mean were calculated and contribute to those in Figure 5.22(a), but are excluded here for clarity purposes.*

not unexpected. The non-Gaussian velocity profile seen here could be attributed to multiple reflections in the coverslip and/or aberrations from the TIR objective lens. The standard error of each point in Figure 5.21 (not shown) was combined to produce those in Figure 5.22.

After traversing the evanescent field the microparticles were found to be lifted up and subsequently lost by the tracking software ($x = 42\,\mu m$). This would be caused by a small fraction of transmitted (far-field) light passing through the glass/water interface due to the lower than critical angle of incidence (see Figure 5.16a). It was found not possible to entirely remove this effect. Due to the illumination of the edge of the back aperture, the focal spot is highly sensitive to diffraction and aberrations, which could give rise to rays propagating below the critical angle for TIR and generate a propagating component in the sample chamber.

The largest guiding velocity observed was for 5 μm particles in p polarised light, with a back aperture power of 1.3 W and was measured to reach $23 \pm 0.5\ \mu ms^{-1}$. It should be noted that the velocity can be increased by an order of magnitude by a small translation of the beamlet to increase the propagating component whilst still maintaining a reasonable guiding distance before leaving the surface.

The p polarised evanescent wave was seen to impart a higher guiding force to

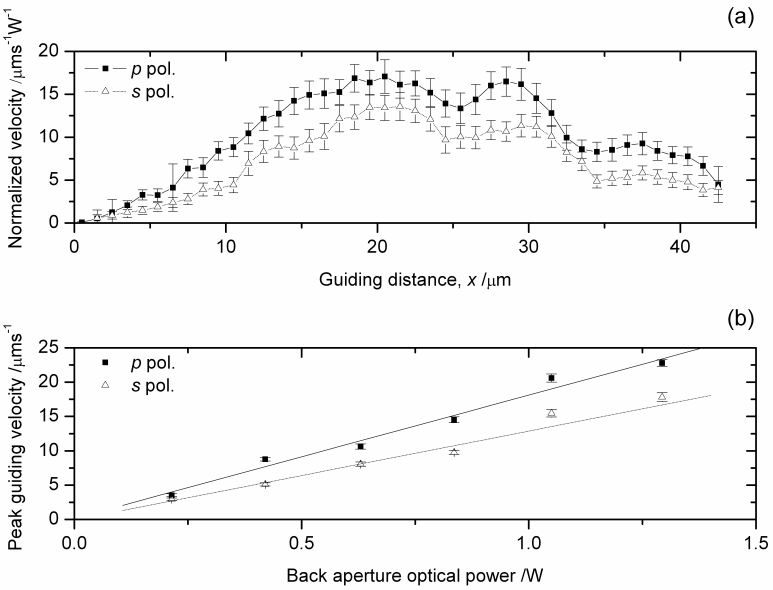

Figure 5.22: *Velocities of 5 μm polystyrene particles guided by an evanescent field generated using a TIR objective lens, illuminated with p and s polarised laser light at the edge of the back aperture. (a) Mean guiding velocity normalised per unit power, as a function of distance travelled along the evanescent field. Each data point is the mean velocity of 36 particles (6 particles at 6 different powers) divided by the back aperture optical power, with the associated standard error. (b) Linear dependence of maximum guiding velocity verses the optical power at the back aperture of the TIR microscope objective lens. Each data point represents the mean peak velocity of 6 particles with the associated standard error in the mean.* [3]

the particles than *s* polarised light. It should be noted that many factors play a role in deciding the dominant polarisation state, including sphere size and polarisability, as well as the laser wavelength and incident wave vector [61, 65, 224]. As predicted by the model and from previous work [61, 72], the velocity of the microparticles in the evanescent field increased linearly with incident laser power, as seen from the experimental results in Figure 5.22b. Gradients of 18.0 ± 0.4 $\mu ms^{-1}W^{-1}$ and 13.0 ± 0.4 $\mu ms^{-1}W^{-1}$ were found for *p* and *s* polarised light respectively, for 5 μm polystyrene spheres in the evanescent field. The experimental measurements were found to be in good qualitative agreement with the predictions from the theoretical model. In particular, both the experiment and theory show a shift between the maximum beam intensity and maximal guiding force/velocity. A similar ratio was observed between the optical forces in *s* and *p* polarisation as predicted theoretically for an incident angle of 61^o (ratio of *p* and *s* peak guiding velocities were 1.2 ±

0.2 experimentally, compared to F_{xp}/F_{xs}= 1.22 for the theoretically obtained peak guiding forces). Further, the lift of the particle, at the end of its trajectory, can also be understood when considering the simulations for incidence angles very close to the critical angle such as 60^o.

The use of a high magnification TIR objective lens in this work produces a higher evanescent field power density (500 times greater than Almaas *et al.*, [222]) compared to previous works using prism-generated evanescent waves. Guiding velocities are an order of magnitude higher than in the work by Oetama and Walz [61] (prism-generated evanescent waves) for equivalent optical powers, particle size and material (refractive index). Guiding velocities are comparable to studies where particles are guided in the evanescent field of a waveguide, such as Grujic *et al.* [71]. The high guiding velocity using a TIR objective facilitates the manipulation of microparticles against a fluid flow and Section 5.6.3 this near-field technique is applied to optical sorting in the presence of fluid flow.

5.6.2 Particle-Dependent Effects

To explore the possibilities for using the TIRF-generated evanescent field for passive optical sorting, the dependence of the evanescent guiding on particle size and refractive index for this geometry was characterised. As the guiding velocity is proportional to the induced evanescent force on particles in the optical field, a comparison of guiding velocities for a range of particle sizes and refractive indices provides a good indication of the sensitivity of this geometry. The guiding of polystyrene and silica particles, of refractive index of 1.59 and 1.37 respectively, was recorded and analysed for sphere diameters of 1, 3 and 5 μm. The peak guiding velocities were calculated and are plotted in Figure 5.23a, for a fixed back aperture optical power of 1.05 W.

The guiding velocity of polystyrene spheres was found to be on average 2.9 $\pm$ 0.7 greater than for silica spheres of the same diameter. The peak guiding velocity increases by 3.0 $\pm$ 0.5 $\mu m s^{-1}$ per μm increase in diameter for polystyrene spheres and 0.7 $\pm$ 0.2 $\mu m s^{-1}$ per μm for silica, over the size range considered here. Size dependence is expected, since as the particle size increases, the area of overlap

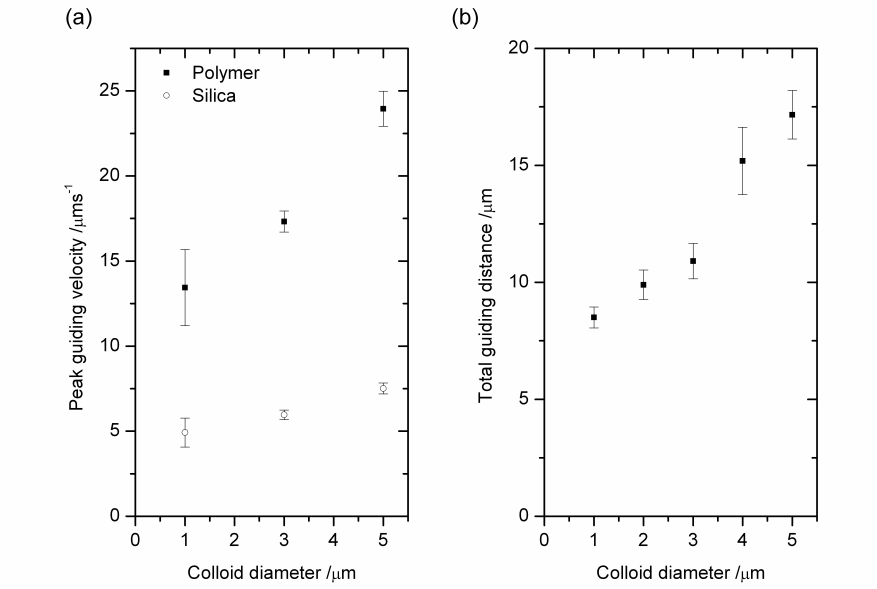

Figure 5.23: *Size and refractive index discrimination of microparticles in an evanescent field generated using a TIR objective lens. (a) Dependence of guiding velocity on particle diameter for refractive indices 1.59 and 1.37, namely polystyrene and silica respectively, for a power of 1.05 W at the back aperture. (b) Separation of microparticles in a 20 μms^{-1} fluid flow using an optical power of 1.3 W at the back aperture. The guiding distance is that travelled by a particle entering the evanescent field at a pre-defined position, travelling some distance orthogonal to fluid flow due to the optical field, before leaving the field with the bulk fluid flow. Data points are the mean distance travelled for a minimum of 5 particles that enter the field within ± 2 μm of a pre-determined position of maximum evanescent guiding velocity.* [3]

between the particle and the evanescent field increases, which results in a stronger radiation force being exerted on the particle [76]. For the size range considered here, the model also predicted the optical force to scale linearly with the particle diameter (see Figure 5.18).

To evaluate the possibilities for using evanescent guiding for passive optical sorting within not just a static geometry, as demonstrated thus far, but within a fluid flow, a second characterisation configuration was employed that closely resembled the microfluidic cross-type chromatography geometry detailed in the next section. This was conducted in a sample chamber, using a motorised microscope stage that translated the sample across the beam at 20 μms^{-1} to emulate fluid flow. Particles entered the field orthogonal to the evanescent guiding direction, and at the pre-determined point in the evanescent field that provided the largest evanescent guiding force (i.e. $x = 21$ μm in Figure 5.22a). As the particles flowed into the

field, they were perturbed along the field in a direction orthogonal to the flow direction, and a distance dependent upon the particle diameter, the optical power and stage/flow speed.

Figure 5.23b shows a linear dependence between the guided distance and the particle size for polystyrene spheres of 1 μm to 5 μm in diameter. For this size range of particles, the guiding distance was found to increase by 2.0 $\pm$ 0.2 μm per unit μm increase in particle diameter, for polystyrene particles passing through the evanescent field at 20 $\mu m s^{-1}$ and with 1.3 W back aperture optical power. The difference in guiding distance for the 1 μm and 5 μm particles is 8 μm, therefore in a fluid flow stream one would expect the particles to be displaced 8 μm with respect to one another after passing through an evanescent focal spot. In a low Reynolds laminar flow environment, a simple branch in the fluid channel should and does suffice in physically separating the two particle sizes into different fluid channels, as will be seen in the next section.

5.6.3 Microfluidic Evanescent Sorting

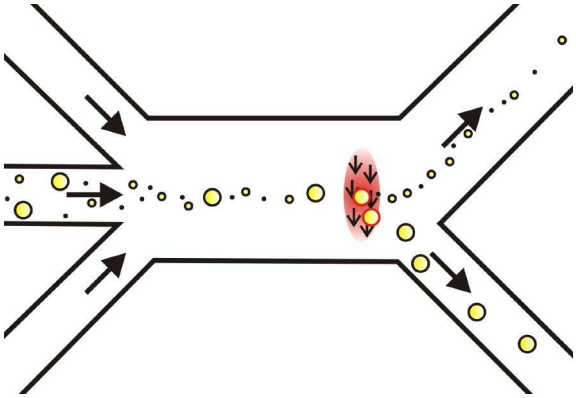

Figure 5.24: *Microfluidic geometry for conducting near-field passive optical sorting, where a TIRF-generated evanescent focal spot is positioned orthogonal to the flow of particles (cross-type optical chromatography). Particles are shunted by the evanescent field by an amount dependent upon their size, allowing fractionation to take place into different outlet channels. Hydrodynamic focusing is employed to ensure all particles pass over the evanescent focal spot.*

The microfluidic sorting geometry is shown in Figure 5.24, where the TIRF-generated evanescent field characterised in the preceding sections is positioned within a microfluidic chip to perform continuous separation of micro-sized particles.

Hydrodynamic focusing (as detailed in Section 2.3) was implemented to restrict the particles to the central region of the channel so as to pass all particles over the evanescent field. The dimensions of the input channels were 50 μm-wide, the central sorting channel was 150 μm-wide, 300 μm-long and the two output channels widths were mismatched, such that all microparticles passed into a wider 100 μm-wide channel unless optically-deflected into a narrower 50 μm-wide channel by the evanescent field. The heights of the channels were 70 μm throughout. Spheres typically flowed along the bottom of the channel due to the density difference between the microparticles and the surrounding medium, allowing them to interact with the evanescent field on the base of the channel.

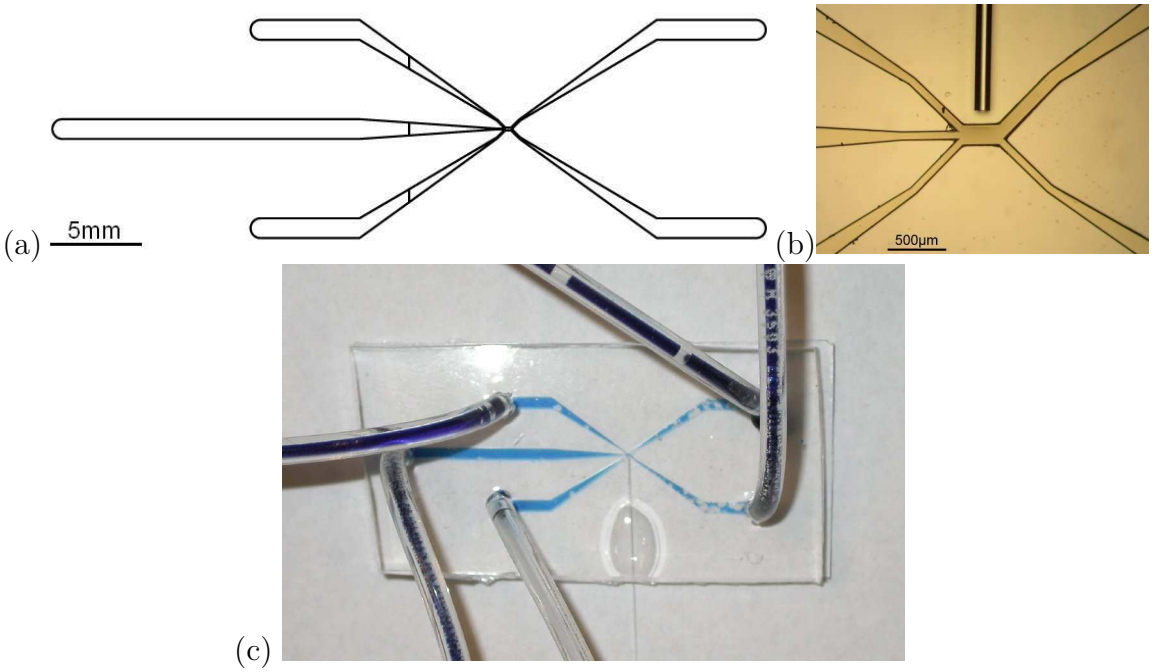

Figure 5.25: *(a) Design of the hydrodynamic focusing chip with the inlets on the left and outlets on the right. A robust method for interfacing piping to the PDMS chips had not been realised in time for these experiments, and is reflected in the chip design. Channels start with dimensions of 1 mm, to match the piping diameter and minimise pressure build-up at the interface with the chip. The channels then taper down until eventually reaching 50 µm in the sorting region. The design did minimise leaks, but was very prone to air bubble formation in the 1 mm channel regions which were near-impossible to remove. (b) The sorting region of the chip, here shown on the SU8 on silicon mould. An optical fibre can be seen attached to the mould in this image, which was included for a different experiment and is not further discussed here. (c) PDMS chip, with channels filled with a blue dye for easy visualisation.*

The microfluidic chip was fabricated in PDMS using the soft lithography pro-

cesses detailed in Section 4.A. The photomask design is shown in Figure 5.25a and the master mould in 5.25b. The PDMS chip was sealed to a coverslip to allow the evanescent field to be directly coupled into the base of the channel. To drive the microfluidic chip, the fluidic setup in Figure 5.26 was used, which provided the three fluid flows required to generate hydrodynamic focusing, with a fixed ratio between the buffer and sample streams of 5:1 respectively. The performance of this fluidic setup left much to be desired and was developed upon in later experiments to provide improved flow stability, sample delivery options and abilities to flush the chip with multiple reagents. For this experiment however, the setup was sufficient in demonstrating rudimentary optical sorting.

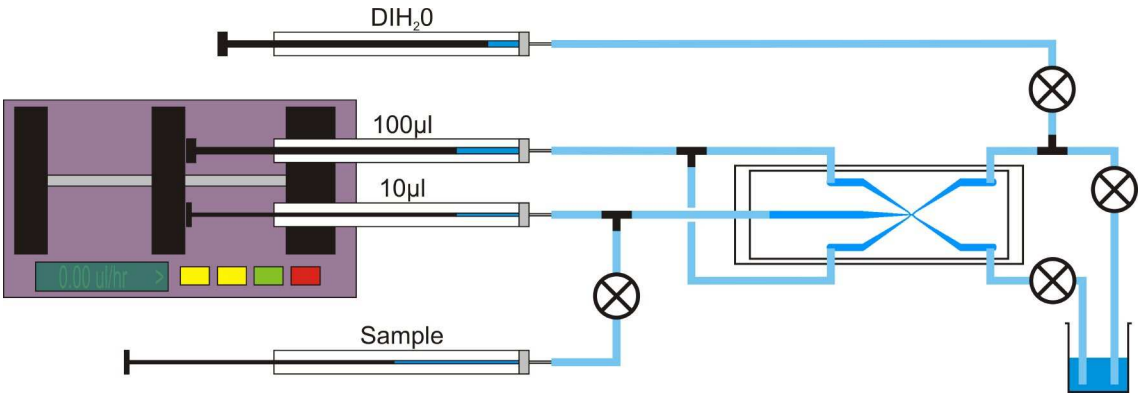

Figure 5.26: *Fluidic setup used for running the microfluidic chip, consisting of a Harvard Apparatus Pico Plus syringe pump and barbed piping connectors, Hamilton syringes, Tygon R3603 (OD 2.4 mm, ID 0.8 mm). This is the simplest possible system for generating hydrodynamic focusing, where a single syringe pump is used but with two syringes of different sizes to give the flow ratio between the buffer and sample flows as required for focusing. The flow circuit is back filled from a single outlet to displace all air, which is absolutely essential in obtaining stable fluid flow. With all taps (circles with crosses) open and syringe plungers removed, filtered deionised water is gently squeezed using the upper syringe in through the outlet and the entire system is filled. The system is then progressively sealed using taps and plungers as appropriate until fully filled and sealed. The sample syringe (containing the colloidal sample) is added at the end, by ensuring that fluid is at the end of the tubing and at the syringe before mating the two. The two outlet taps are then opened, a volume of sample injected into the chip, its tap closed and then the syringe pump is run. This system was adequate is demonstrating hydrodynamic focusing for short periods of time, but was highly unstable, sensitive to surrounding air currents, did not provide flushing capabilities and could only provide a fixed ratio between the buffer streams. A much improved fluidic setup was implemented for later experiments and can be found in Section 6.2.1.*

The sorting capability of this technique was realised on a poly-disperse mixture of 1, 3 and 5 μm polystyrene spheres within a PDMS microfluidic chip, for particle

velocities of ~50 μms^{-1}. The evanescent field (1.3 W at the back aperture) was sufficient in deflecting 5 μm particles up to 25 μm (in a direction orthogonal to the flow) from the main particle stream, thus allowing them to exit via the smaller output channel of the chip. The smaller 1 and 3 μm particles were barely deflected and continued to exit the chip via the larger output channel. An increase in flow rate, optical power and particle density could potentially increase the throughput of sorting from the order of one particle per second that was obtainable here, to tens or hundreds of particles per second.

Figure 5.27 shows a series of still images of successful optical sorting, the video for which is available online [3]. Figure 5.28 shows particle trajectories, as tracked using the particle tracking software, for a series of 5 μm spheres with and without deflection into the lower channel by the evanescent field.

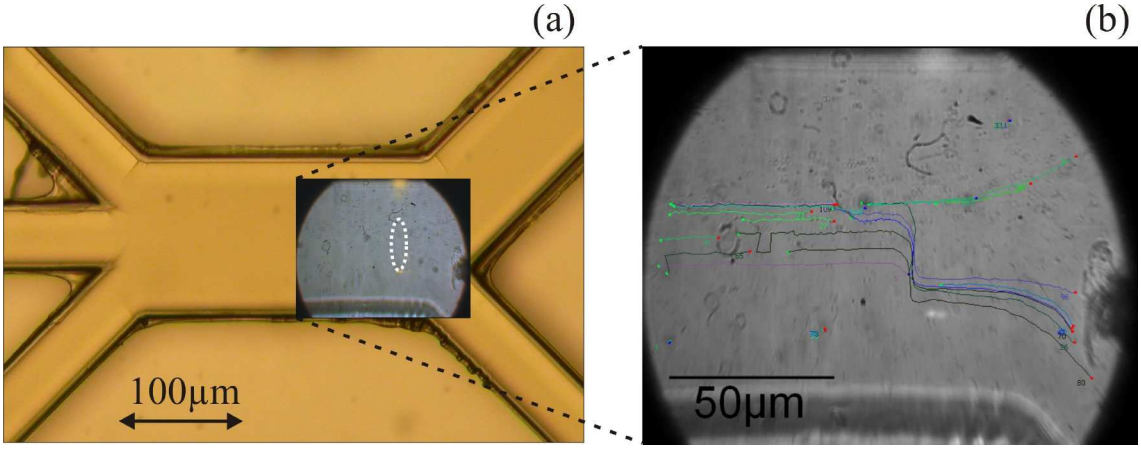

Figure 5.28: *(a) Close up of the mould showing location of video acquisition. (b) Particle tracking of 5 µm spheres with and without deflection by the evanescent field. The width of the hydrodynamic focusing stream observed here is 18 µm, which is in close agreement with 19 µm as predicted by Equation 2.8. Evanescent guiding distances were found to be between 16 and 25 µm depending upon the particle velocity and entrance point as the particle comes into contact with the evanescent field.* [3]

5.7 Conclusion

In this work, an original geometry for optically deflecting and sorting micro-objects is reported employing a total internal reflection microscope (TIRFM) system. A small beam of laser light is delivered off-axis through a total internal reflection (TIR) objective which creates an elongated evanescent illumination of light at a

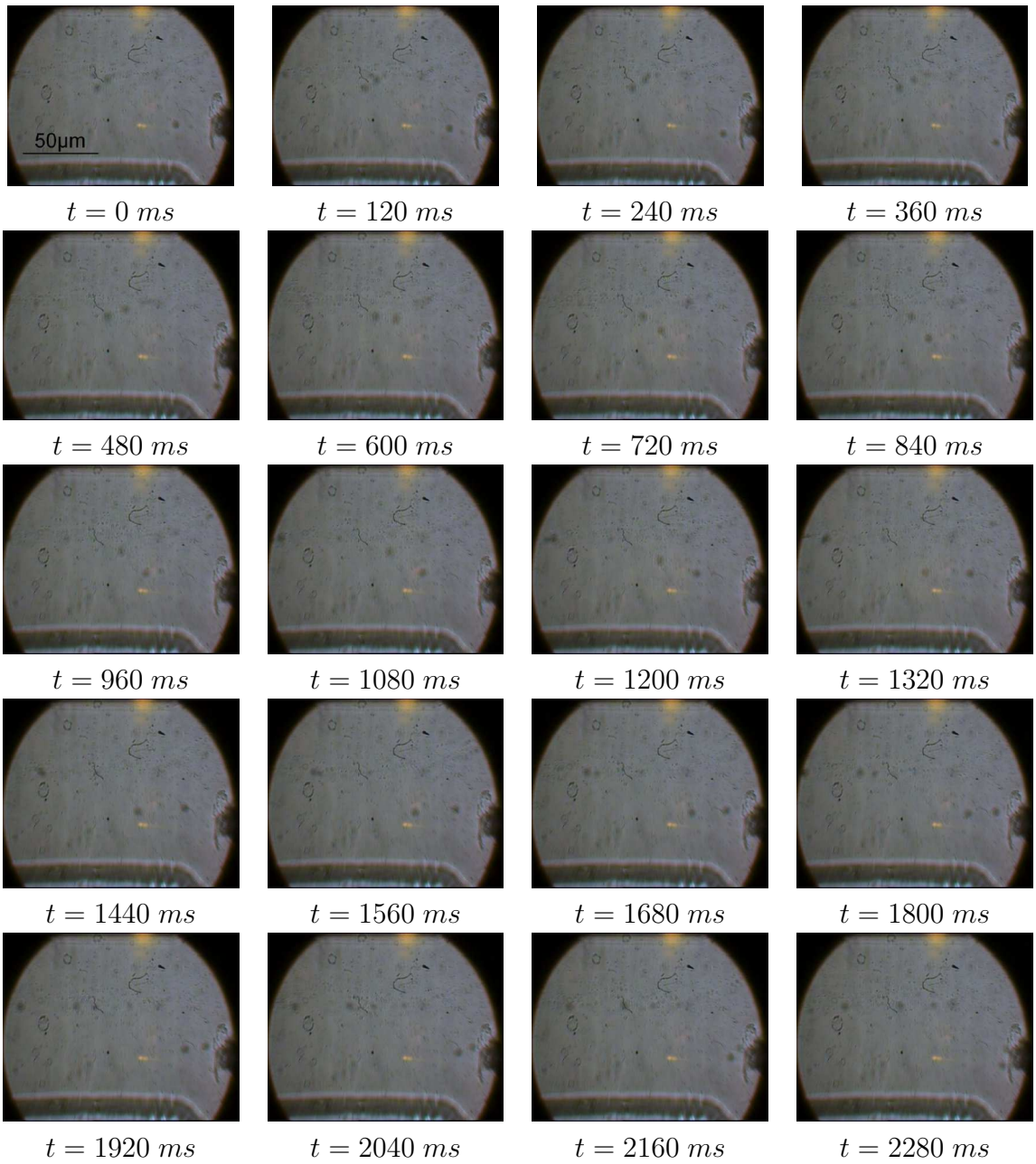

Figure 5.27: *Video stills of the separation of 5 µm spheres from a poly-disperse mixture of 1, 3 and 5 µm polystyrene spheres, using a TIRF-generated evanescent field in a PDMS microfluidic chip. Hydrodynamic focusing deliveries a stream of particles to the beam, where the largest ones most strongly deflected and separated from the main particle stream into a different output channel (lowermost in the figures). The flow of 1 and 3 µm spheres is more easily visible in the supplementary video to the paper* [3]*. Fluid flow is from left to right, and the evanescent field is orthogonal to this, deflecting particles downwards in these figures. The image from the camera port of the microscope was demagnified by 2.5x to widen the field of view.*

glass/water interface. The high magnification of the TIR objective lens allows a higher optical power density to be obtained and increased guiding velocity compared to previous prism-generated TIR techniques. The speed of the deflected objects was found to be dependent upon their intrinsic optical properties. The optical forces are sufficiently large to move particles during fluid flow, thus allowing the evanescent fields to deflect particles within a fluid flow and be applied to passive sorting of microparticles according to their intrinsic properties, based on their interaction with the optical field.

A fully vectorial finite element method for this geometry was presented. The optical force profile predictions for the evanescent field were found to agree qualitatively with experimental observations, but improvements are required for quantitative agreement. In this new geometry, p polarised light was found to induce a greater guiding force on the microparticles than s polarised light and that the maximum force is shifted with respect to the illumination intensity maxima. Experimentally, the maximum guiding velocity due to the evanescent force was found to increase by 3.0 $\pm$ 0.5 $\mu m s^{-1}$ per μm increase in diameter for polystyrene spheres and 0.7 $\pm$ 0.2 $\mu m s^{-1}$ per μm for silica over the diameter range of 1 μm to 5 μm. This was employed for optical sorting of microparticles in a PDMS microfluidic chip. By exploiting the linear dependence of the evanescent guiding force on particle size, entirely passive sorting of 5 μm spheres from a poly-disperse mixture of 1 μm, 3 μm and 5 μm polystyrene spheres was characterised and accomplished. This method may readily be extended to initiate large area optical sorting within microfluidic devices and the potential for decoupling the light field that initiates the sorting from the observation optics (which could be implemented from above).

Hydrodynamic focusing was employed to constrain the flow of particles to pass over the evanescent focal spot. This did however produce problems in flow stability. The use of three input flows, and the interplay between any small pressure fluctuations in the flows, due to external environmental influences such as air movements in the room, thermal expansion of various fluidic components, or trapped air bubbles within the channels, caused major instabilities in fluid flow. Proof of principle demonstration of the technique were entirely possible, but a sustained ex-

periment for collecting statistical information on the efficiency of the system were not. This would clearly have to be corrected if the system was to be utilised for actual sorting applications.

The next chapter significantly improves on the fluidic setup implemented in this experiment, which progressively leads to the complete replacement of all of the fluid components including the syringes, tubing and connectors. A push-pull geometry is implemented to form a completely sealed system and an improvement to sample injection is made.

Contribution

R. Marchington built the optical setup, conducted all of the experimental work, analysed the particle tracking data and fabricated the microfluidic chips. At early stages in the project he was supervised by P. Reece and V. Garcés-Chávez. M. Mazilu and S. Kurikose (Swinburne University of Technology, Australia) jointly developed the theoretical model. G. Milne developed the particle tracking software. L. Paterson conducted the RBC preparation.

Chapter 6

Femtosecond Photoporation of Mammalian Cells within a Microfluidic Chip

The use of optical beams for generating forces for trapping and guiding is just one avenue of application to microscopic objects. In this chapter, the use of focused femtosecond (fs) light is explored in the realms of nano-surgery. A high throughput, automated photoporation system within a microfluidic environment is presented, for the optical injection of agents into living mammalian cells. This is shown schematically in Figure 6.1. The use of a focused laser beam to create a sub-micron hole in the plasma membrane of a cell (photoporation), for the selective introduction of membrane impermeable substances (optical injection) including nucleic acids (optical transfection), is a powerful technique most commonly applied to treat single cells. However, particularly for fs photoporation, these studies have been limited to low throughput, small-scale studies, because they require sequential dosing of individual cells. Hydrodynamic focusing is employed to direct a flow of single-file cells through a focused fs laser beam for photoporation. Upon traversing the beam, a number of transient pores potentially open across the extracellular membrane, which allows the uptake of the surrounding fluid media into the cytoplasm, also containing the chosen injection agent. The process is entirely automated and a rate of 1 cell/sec may readily be obtained, enabling several thousand cells to be injected

per hour using this system.

The chapter starts by introducing the field of photoporation and optical injection, before describing the advancements in the microfluidics from earlier chapters to make possible the insertion, and more critically, the collection of cells after laser treatment. The cell preparation is detailed for suspending adherent cells prior to fluid flow, and the optical setup is described. Finally results for optically injecting human embryonic kidney cells (HEK293) mammalian cells with propidium iodide is presented along with viability tests using Calcein AM to quantify the efficiency in producing viable injected cells using this method.

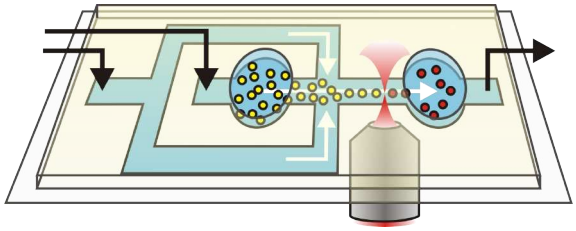

Figure 6.1: *Schematic of the microfluidic chip for photoporation. The cells are first inserted directly into chip via left-most reservoir. Syringe pumps then drive the fluid as indicated by the arrows. Cells pass into the hydrodynamic focusing junction, forcing them to flow one at a time through a fs laser beam (as focused into the chip via the objective lens), where optical injection occurs. Cells enter the second reservoir, ready for collection with a pipette for culture and/or analysis. Photoporation rates of 1 cell per second could readily be obtained using this approach.*

6.1 Introduction

6.1.1 Permeablisation of the Cellular Membrane

All multi-cellular organisms (eukaryotic), including animals, plants and fungi consist of cells containing three basic constituents: a nucleus, in a cytoplasm (containing other organelles), encapsulated within a plasma membrane. The role of the membrane is to contain the contents of the cell, and to control the flux of select molecules and ions into and out of the cell, thus maintaining the nutritional requirements, concentration gradients, and cell potential, as well as allowing larger molecules for more complex tasks such as signalling. The membrane consists of a double layer (or bilayer) of phospholipids, a long chain molecule with a hydrophobic head and a hy-

drophobic tail [35]. The lipids are arranged such that all the tails all point inwards towards each other, leaving the hydrophilic heads pointing out to form the outer and inside surfaces of a 4-5 nm thick membrane. Plant cells also have a surrounding cell wall for structural rigidity.

The membrane for a healthy cell is impenetrable to large polar molecules, such as DNA, which is hydrophilic [227]. The facility to overcome this barrier and inject a foreign material into a living biological cell without damaging the integrity of the cell is of utmost interest, with a wide range of exciting applications in biology and medicine. As well as the possibilities for delivering stains and dyes to individual cells (for flow cytometry, or for imaging for example), one of the most interesting application is in delivering drugs or foreign DNA to within a cell whilst preserving its viability. Examples include agricultural biotechnology, where new genes are being incorporated into crops for increased yields, nutritional value, disease resistance and wider growing conditions; in a medical setting, delivery of DNA for genetic therapy has the potential to cure diseases through the incorporation of extra or missing genetic material to promote or halt particular cell functions; in the pharmaceutical industry, the delivery of drugs and subsequent single cell monitoring [228] could progress understanding and cures to diseases; and the widely applied genetic tagging of cells with a fluorescent protein marker, such as jellyfish-derived GFP (green fluorescent protein), for sub-cellular spatial location or proof of concept transfection [229].

A diverse range of methods exist [230] for permeablising the membrane of a cell for the insertion of foreign material including: the insertion of micron-sized pipettes (microinjection) [231]; application of electric fields (electroporation) [232]; ballistic insertion of coated nanoparticles (gene gun) [233]; transportation of therapeutic agents encapsulated in lipid- (lipofection) or polymer-based particles [234]; viral delivery [235]; pore formation or permeabilisation using acoustic waves (sonoporation) [58, 236]; or as utilised here, using laser fields to open a transient pore in the membrane (photoporation) [237]. These techniques all have their pros and cons, applicability *in vitro* or *vivo*, rate of cell treatment, associated efficiency of injection and cell death rates or toxicology concerns [230, 238–240].

6.1.2 Membrane Perforation using Optical Techniques

Optical injection is a promising technique for transiently perforating the membrane of living biological cells, using a tightly focused laser beam to allow impermeable molecules, such as drugs, dyes or nucleic acids (including plasmid DNA), to pass into the cytoplasm. First demonstrated by Tsukakoshi *et al.* in 1984 [237], a wide spectrum of laser sources have since been successfully implemented, including continuous wave (CW) at 405 nm [241,242] and 488 nm [243–245] as well as pulsed laser sources of nano-, pico- [237,246–248], and most notably femto-second pulse durations in the near infrared [41,53,239,249–259], and 2080 nm (Ho:YAG) sources [247,260].

Femtosecond optical injection is a non-invasive and sterile technique, with recent studies in delivering plasmid DNA for subsequent transfection of the cells with efficiencies of up to 80% [251] and demonstrating excellent cell viability. Photoporation has successfully been performed on in excess of 35 cell types to date [261], from plant cells such as tobacco protoplast [248] and Egyptian wheat embryos [262], to a large number of mammalian cell lines, including mammalian neurons [249] and a number of human stem cells [256]. Indeed, it has recently been reported that optical injection can be utilised to differentiate mouse embryonic stem cell colonies into the extraembryonic endoderm [251].

Nano- and picosecond optical injection can be used to treat many dozens of cells simultaneously [237,246–248], but is associated with a large "zone of destruction," with viable cell permeation only occurring on the periphery of a laser-induced acoustic shockwave [261]. Femtosecond and CW sources facilitate the treatment of single cells, resulting in improved efficiency and viability. The most widely used laser source is the Kerr lens mode-locked fs Titanium:Sapphire laser, which when focused through a high numerical aperture lens will produce a sub-micron diffraction-limited laser spot, with peak powers of the order of kWs at the focus. When delivered to the cell membrane [254], this will generate multi-photon absorption and ionisation that forms a low-density free-electron plasma within the lipid bilayer [263]. The transient interaction invokes the cell to uptake femtolitre volumes of the extra-cellular fluid, containing the nanoparticles [41], charged molecules (such as DNA) or other reagents, for insertion into the cell. Importantly, the power levels used are below

the threshold for optical breakdown [263]; thus minimising collateral damage and maintaining the viability of the cell. Cells are targeted one at a time and as such fs optical injection is an excellent tool for single cell analysis, or for porating small populations of a few tens of cells.

Typical experimental parameters for fs optical transfection are one [259] to three 16-100 ms doses [253, 255, 264] of 780-800 nm, 100 fs pulses (stretched to 120-200 fs [238] in the sample due to group velocity dispersion through the optics) at a 80 MHz repetition frequency, with an average power of 40-100 mW at the focus of a 1-2 μm focal spot positioned on the cell membrane [53, 229, 251, 254, 255, 259, 261]. Cells are targeted one at a time, with a tiny (sub-micron) region of its plasma membrane perforated ("photoporation") using a diffraction limited laser spot and as such is an excellent tool for single cells, or small populations of a few 10's of cells. Photoporation is a non-invasive, sterile technique, obtaining transfection efficiencies of up to 80% [251] for fs-based optical transfection and with excellent cell viabilities.

6.1.3 Cell Throughputs in Photoporation Systems

The ability to localise the photoporation effect to a precise region on a single cell has been both advantageous and limiting. Whilst this methodology is suitable for single cell analysis, dosing more than ~100 cells is time consuming. This limitation has prohibited larger studies on cell populations. To improve the throughput of fs photoporation, there are several possible approaches.

One method for improving the throughput of fs optical injection is to remove the necessity for manually locating the beam focus on each cell. This has previously been demonstrated using a conical lens (axicon) to generate a "diffraction-free" Bessel beam [53], and later using a spatial light modulator (SLM) controlled by a "click and shoot" computer interface, allowing a user to select cells at will on the screen for injection, without the need for careful positioning of the beam focus [265]. One could alternatively envisage an automated microscope stage to scan the Petri dish of cells back and forth across the beam.

The method addressed in this chapter is to introduce a cell delivery method that streams continually cells through the beam for automated injection. Indeed,

cell delivery systems for other injection techniques have previously been demonstrated, including microinjection and electroporation with good success, making use of microfluidic chips for this process. In microinjection, a microfluidic flow has been utilised to "spear" cells onto a stationary microneedle for microinjection [266], and another approach uses a deformable chip with an embedded microneedle allowing cells to be "jabbed" as they flow past [267].

Contrary to the use of microfluidics in microinjection where throughputs have been scaled up through automation, in electroporation microfluidics has been utilised to scale down electroporation from dosing bulk samples to allow treatment of single cells. Several versions of electroporation chips have been demonstrated including simple flow-by electroporation Ziv *et al.* [268] or Bao *et al.*'s [269] study where cells are characterised based on their deformablity in response to the poration. Wang *et al.* use a PDMS deformable valve to generate the electrical pulse required to permeate the membrane of cells, within a fluidic channel [270]. More recently, Zhen *et al.* [271] demonstrated electroporation in microdroplets, where cells and plasmid DNA were first encapsulated within droplets, before being flowed across a pair of electrodes invoking electroporation of the contents. Zhu *et al.* [272] utilised hydrodynamic focusing to squeeze cells between two buffer fluids of opposing charge that in fact form the electric field gradient for poration, in parallel to localising the cells in the centre of the channel.

6.2 Microfluidics for Optical Injection

Optical transfection posed the interesting requirement to not only allow the insertion of cells into a microfluidic chip, but to also to allow retrieval of the treated cells after poration for analysis and/or culture. Culturing the cells on chip was a possibility, but was not considered a practical option at the first stages. It is apparent that cells are in fact quite dense, and sink fairly rapidly to the base of a fluid channel. Section 2.6 details the expected behaviour of particles denser than their surrounding medium and in a microfluidic environment, finding that as a rough approximation, cells could be expected to drop out of suspension at around 10 μms^{-1}. This had

some advantages and some disadvantages, and this effect strongly influenced the design of the microfluidic system; ultimately enabling the placing of insertion and collection ports on the chip itself rather than interfacing the external tubing.

6.2.1 Cell Delivery & Collection

First iterations of the system consisted of a near identical setup to that in Section 5.6.3. This rapidly proved to be inadequate for dealing with cells. The 0.8 mm inside diameter of the flexible Tygon tubing meant that there was practically zero flow as far as suspended cells were concerned, causing them to come to rest within the tubing and adhering before ever reaching the chip, even after the insertion of many ml's of sample. It was noted however, that if the piping for the sample was made vertical, cells could be made to roll down the pipe into the chip due to gravity. This observation rapidly led to the idea of moving the section of vertical tubing for cell delivery, to a vertical sample reservoir on the chip. Behind the reservoir was placed a flow channel, which was connected to the standard tubing, and to the syringe pump. This allowed cells to be dropped directly into the chip, within a few hundred micrometres of a hydrodynamic focusing section. In the same manner, a second reservoir could be included on-chip further down stream, from which a portion of fluid could be collected. The smallest containers that could be found were 500 μl micro-centrifuge tubes, which with the bottom section removed, formed an open bottom reservoir. The click-top lid on the tube was found to massively disturb the flow when used, so laboratory Nescofilm was used with a rubber ring to seal the top of the tube after filling.

6.2.2 PDMS Chip

The microfluidic chips for this study were fabricated in polydimethylsiloxane (PDMS) using the soft lithography procedures described in Chapter 3 and detailed in Section 4.A. The PDMS chip was designed to have an inlet and outlet port for the insertion and collection of cells, and a hydrodynamic focusing region to force the cell sample into a thin (sub-cell sized) stream down the centre of the fluidic channel thereby

directing all cells through the photoporation beam. Briefly the fluidic design was composed in a CAD software package and printed to high resolution transparency (Circuit Graphics Ltd). Photolithography was used to form a mould in 70 μm thick SU8 (Microchem) resist on a silicon wafer and silanised with perfluorooctyltrichlorosilane (S13125, Flurochem). Two-part PDMS (Sylgard 184, Dow Corning) was mixed in a 1:10 weight ratio, degassed, poured on to the mould and partially cured at 65^{o}C for 45 minutes. To incorporate cell injection and collection ports, it was necessary to define a second section of PDMS on top of the first to provide sufficient support for the cell ports, as can be observed in Figure 6.2. This was formed by placing a pre-prepared PDMS template (a silanised rectangular block with 1 cm by 2 cm section removed from the centre) on top of the first layer, and infilling with PDMS 1:10 and further baking for 2 hours at 65^{o}C to fully cure the structure.

Once cured the PDMS was peeled from the mould, inlets punched (Harris Micropunch) and irreversibly sealed to a type-1 coverslip (VWR International) using a hand-held plasma treater [193]. The channel dimensions were 150 μm wide by 70 μm high throughout except at the pipe inlets and reservoirs, that were 1.2 mm and 3 mm respectively. Adapted 0.5 ml micro-centrifugation tubes (cap and base removed) were later inserted into the 3 mm punched holes to act as cell injection and collection reservoirs.

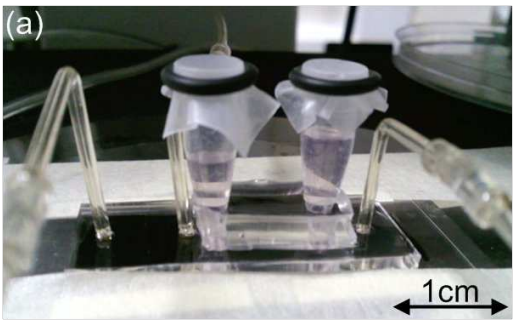

Figure 6.2: *Image of the PDMS chip showing micro-centrifuge tubes for cell insertion and collection, and the two inlet pipes on the left for buffer and sample flow and a single outlet pipe on the right.*

6.2.3 Fluidic Setup

Several features were incorporated into the fluidic setup to minimise fluctuations in the fluid flow in order to obtain a steady and reproducible flow of cells over the course of the experiment. Three syringe pumps (Harvard Apparatus, Pico Plus) were used in a "push-pull" configuration to generate stable hydrodynamic focusing: one to drive the sample stream, one for the buffer streams and a third as a suction pump on the outlet. Rigid Radel R (Upchurch) tubing was used to interface the chip to the syringe pumps (see Figure 6.3), providing significantly more stable flow than the Tygon R3603 flexible tubing, that was used purely for interfacing the peristaltic pump. Four-way L-junction switching valves (Upchurch) were used to connect the peristaltic and syringe pump fluid lines, allowing the chip and pipes to be flushed and filled as desired using the peristaltic pump, but also isolated to just the syringe pump lines when running the experiment. Gastight (Hamilton) 100 μl syringes were used with the syringe pumps.

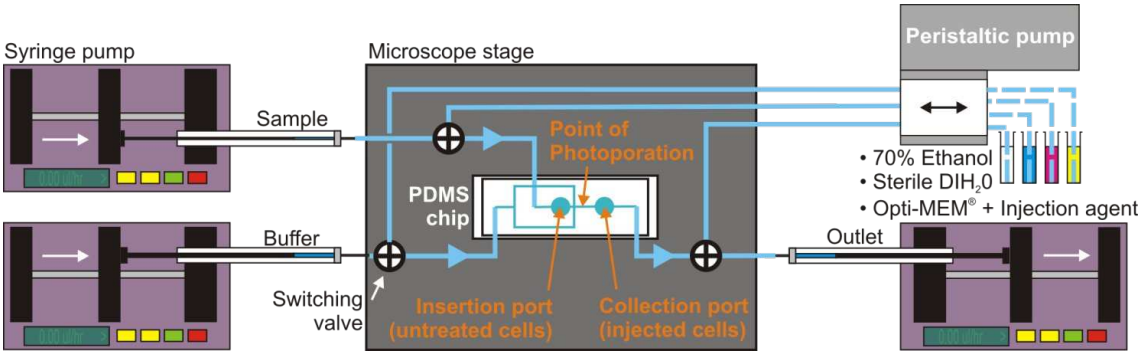

Figure 6.3: *Fluidic setup required for cleaning, sterilising and flowing cells. Cleaning, sterilising and filling of the fluidics with cell medium is conducted using the peristaltic pump. Syringe pumps are used for flowing of the cells for optical injection, and operate in a "push-pull" configuration to obtain stable fluid flow. Layout of the PDMS microfluidic chip is also shown, which matches with Figure 6.1. The injection agent (propidium iodide) is added to the Opti-MEM® before filling the chip and piping.* [1]

Flow rates were controlled via a Labview interface and set to 7 μlhr^{-1} and 70 μlhr^{-1} for sample and buffer pumps respectively which, depending on the confluency of the cell sample, gave a rate of 1 cell per second, and at a velocity of 1100 $\pm$ 100 μms^{-1}. It should be noted that the velocity of the cells is lower than the peak fluid velocity in the channel, because the cells were situated in the lower half of the channel due to gravity. As the cells are denser than the fluid medium, this allows

them to rest on the bottom of the injection reservoir at the start of the experiment. At the start of an experiment, there will be some lift of the cells due to Bernoulli lift in a parabolic flow profile, but at these flow rates it was not expected to contribute to an elevation of even 10 μm from the channel base. The sharpest brightfield image of the cells as they traversed the laser spot was at a position of 6 μm above the coverslip. Other evidence supporting this was that the cells were observed to flow at similar velocities, indicating similar positions in a parabolic shaped flow profile.

6.3 Cell Culture, Preparation & Collection

Propidium iodide (PI, Sigma-Aldrich) is a membrane impermeable stain commonly used in proof of principle cell injection studies. PI is only taken up by cells whose membranes have been compromised and will be excluded by living viable cells. It interacts with the DNA of the host cell by binding to specific nucleotides within the DNA strand. Once the binding occurs, and under the right excitation illumination, the PI molecules will exhibit intense fluorescence at 617 nm. In order to verify PI uptake and confirm cell viability, upon treatment, the cells were stained with the membrane permeable neutral vital dye Calcein-AM (CAM, Invitrogen), which is rapidly converted by cell esterases into calcein that fluoresces at 530 nm within a viable cell [273]. These two fluorescent dyes therefore work well in conjunction to identify viable and successfully optically injected cells.

Human embryonic kidney (HEK293) cells were cultured in Dulbecco's Modified Eagle's Medium (DMEM, Sigma-Aldrich) with 10 % foetal calf serum (FCS, Globepharm), 20 $\mu g ml^{-1}$ streptomycin (Sigma-Aldrich) and 20 $\mu g ml^{-1}$ penicillin (Sigma-Aldrich) in T25 flasks (Fisher Scientific) kept at 37^{o}C and 5 % CO_2 in an incubator. The cell population was expanded and brought to sub-confluency nominally three times per week using Trypsin-EDTA (Sigma-Aldrich). The process of trypsinising the cell stock defines the cell passage number, which throughout the experiments was kept between 15 and 30.

For the purposes of the experiment, HEK293 cells cultured in a T25 flask were suspended by adding 1 ml of Trypsin-EDTA and centrifuging at 0.2 g for 5 minutes

in a micro-centrifuge tube (1.5 ml). The Trypsin was carefully removed from the medium and cells were rinsed twice with filtered Opti-MEM® to remove residual Trypsin. Next, the cells were gently stirred in 1 ml of fresh filtered Opti-MEM® with 1.5 μM of the injection agent PI, and passed through a 40 μm filter (BD Falcon™ Cell Strainer, VWR) to remove any clumps of adhered cells. Finally, 200 μl of this cell suspension medium was aliquoted into a micro-centrifuge tube, and 20 μl of this was loaded into the microfluidic chip for an experiment.

The fluid medium used for filling the microfluidic chip and associated piping was also prepared immediately prior to the experiment. 3 ml of filtered Opti-MEM® in a T25 flask with a gas permeable cap was degassed by a vacuum pump for 10 minutes, which prevented the formation of gas bubbles within the microfluidic chip during experiments. 3 μl of 1 $mgml^{-1}$ water solution of PI was loaded into the flask to obtain a final PI concentration of 1.5 μM in degassed Opti-MEM®.

6.4 Optical Setup for Photoporation

The optical setup is shown in Figure 6.4. A mode-locked Titanium:Sapphire laser (MIRA, Coherent, emitting at 800 nm, repetition rate 80 MHz, 100 fs pulses, 2 W average output power) was used for optical injection. A set of two halfwave plates and polarising beam splitters were used to split and attenuate the beam to obtain the desired power at the focus of the objective, and to provide an output for a spectrum analyser to monitor the mode-locked output. The beam was expanded using a x6 telescope to overfill the back aperture of a x60 objective lens (Nikon) of 0.8 numerical aperture, to obtain a near-diffraction-limited sub-micron spot at the focus. The beam was directed into a microscope (Eclipse Ti, Nikon), with a high reflecting mirror for 800 nm as shown, to direct the beam to the objective and split the laser beam from the image for viewing on the CCD camera (DFK41BU02, The Imaging Source). The transmission of the objective lens was measured using a 'dual objective' method [4], allowing the optical power at the focus to be calculated from the power measured at the back aperture, which was set to 90 mW at the focus for the data presented in the results section. This power was chosen as a physical response

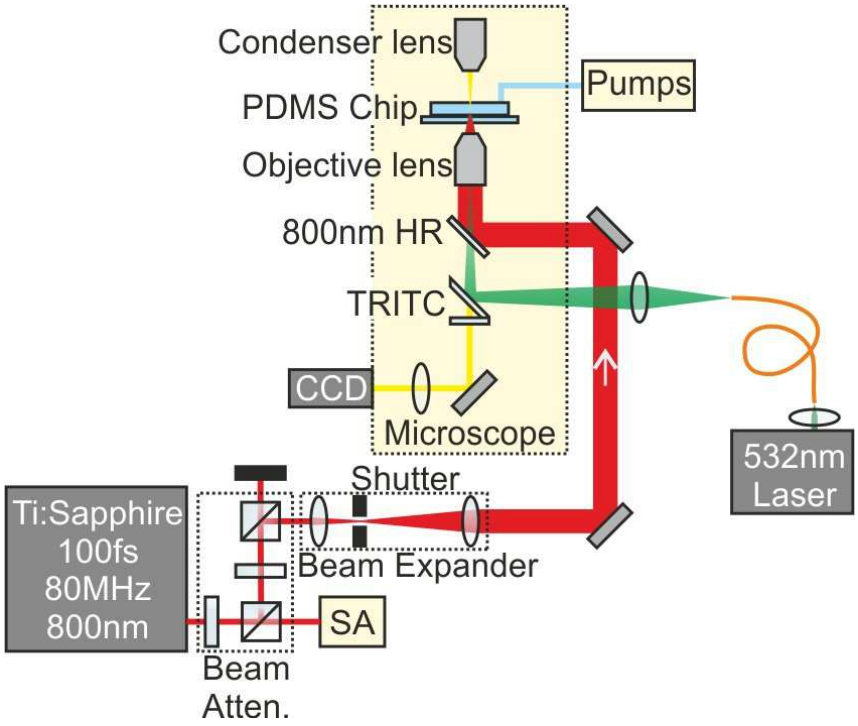

Figure 6.4: *Schematic of the optical setup, consisting of a photoporation setup and a 532 nm laser for excitation of red-fluorescing PI, both coupled into a Nikon Eclipse Ti microscope. The optical components comprised of a Ti:Sapphire laser, power attenuators (2x halfwave plates and polarising beamsplitters), spectrum analyser (SA), beam expanding telescope, fast shutter and within the microscope a 800 nm high-reflecting dichroic filter cube. The excitation 532 nm laser (Photonics Innovation Centre, St Andrews) was coupled into a multimode fibre, whose exit facet was relayed using a 100 mm lens to the back aperture of the objective lens to provide uniform excitation across the sample field of view.*

(bubble formation, followed by cell "blebbing") could be observed at higher powers, which is typically associated with permanent membrane damage and subsequent cell death. Due to group velocity dispersion through the optics, one expects some broadening in the pulse duration by the time it reaches the sample, which was previously measured for the exact laser used and a near-identical photoporation setup, and found to be an insignificant increase of 10-20 fs [238].

A shutter was incorporated into the beam path in order to resemble as closely as possible the situation of stationary cells in a Petri dish, where typically between one and three 40 ms laser doses would be delivered for generating optical injection. In this microfluidic experiment, the shutter (LST200-IR, nmLaser Products) was used to pulse continually the beam, delivering a stream of 4 ms (125 Hz square wave trigger signal) doses to the cells as they traversed the beam. A typical cell of 20 μm

diameter travelling at 1100 μms^{-1} would therefore receive two or three 4 ms laser doses as it flowed through the focal spot, depending on its relative phase with the shutter.

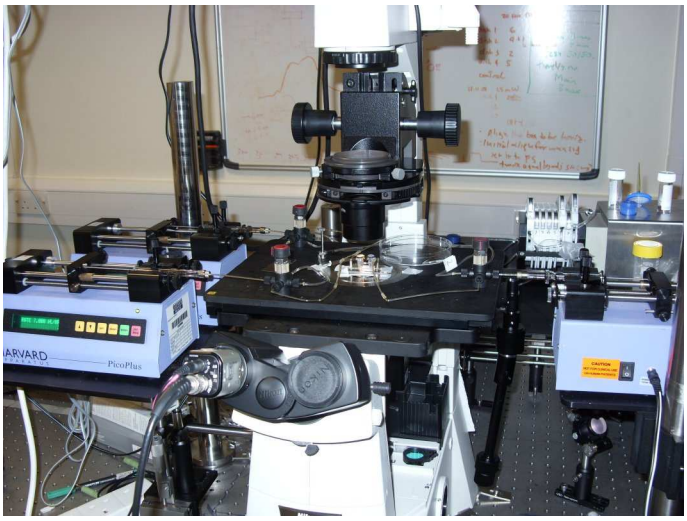

Figure 6.5: *Photograph of the experimental setup, showing the syringe pumps and peristaltic pumps, the fluid piping, and the microfluidic chip in the centre on the microscope stage.*

6.5 Experimental Procedure

The chip and fluidics were sterilised before each experiment, with the PDMS chip being used once only and autoclaved before use. The piping, syringes and connects were flushed with 70 % ethanol, rinsed with filter-sterilised deionised water and finally dried with filtered air using the peristaltic pump. The chip, piping and syringes were then filled, from the outlet end to minimise bubble formation, with filtered Opti-MEM® solution also containing the PI to be injected optically. The cell injection ports were sealed during the filling procedure using Nescofilm (a self-sealing elastic membrane, VWR) such that the outlet port had a higher fluid level than the inlet. This ensured that when inserting the cell sample, a back flow occurred to ensure the cells did not flow to the collection port before the system was stabilised and beam turned on. Once filled, the fluid switching valves were used to isolate the fluid pipes necessary for hydrodynamic focusing from the peristaltic pump and associated cleaning pipes, producing a closed fluid system.

HEK293 cells were inserted into the chip via the micro-centrifuge tube 'insertion port'. A 20 μl cell sample was pipetted into the port and allowed several minutes for it to settle onto the coverslip (base of the channel), as monitored on the CCD camera. Once settled, the syringe pumps were turned on, generating a stable hydrodynamic focused flow of cells, close to the bottom of the channel. In effect, the system is close to 2D hydrodynamic focusing, where the combination of gravity and 1D hydrodynamic focusing confines the cells in both vertical and horizontal positions in the channel. The focused laser beam was positioned approximately two channel widths (300 μm) downstream from the focusing junction, in the centre of the cell stream and raised 6 μm from the base of the channel (coverslip), which was found to be most optimal for hitting the cells. Cells would then come to rest under the 'collection port,' due to the considerably larger cross section and hence slower flow channel in this region.

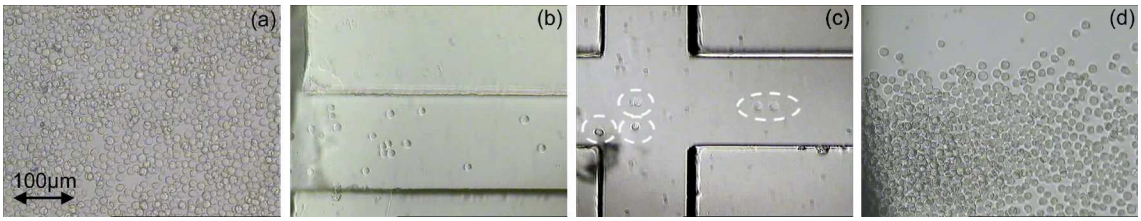

Figure 6.6: *Images from within PDMS microfluidic chip, as shown schematically in Figure 6.1. (a) Sample injection port after insertion of cells and an initial waiting period of 5 minutes for cells to reach the base (coverslip) of the channel. (b) Cells flowing from left to right out of the injection reservoir and towards (c) the hydrodynamic focusing junction, where cells (circled) can be seen flowing single file down the centre of the channel after the junction. The focused fs laser beam for optical injection was situated 300 µm downstream of the junction. (d) Cell collection port after 10 minutes showing several hundred optically injected cells that have come to rest due to the drop in flow velocity in this region of the chip.* [1]

After flowing the cells for typically 10 minutes, or once approximately 500 cells had passed through the beam, the syringe pumps were stopped, the collection port opened, and the cells beneath this port removed from the chip using a pipette. It was estimated that approximately 80 % of the cells could be successfully removed and collected using this method, losses mainly being due to cells remaining in the pipette tip rather than in the chip itself. The contamination from unporated cells coming from the rest of the chip is negligible during the collection process. Upon

collection, the chip was removed, the piping rinsed and sterilised, and the system was ready for a new chip and cell sample. Following the removal of the optically injected cells, the control samples were collected from the injection port. The contamination from optically injected cells was observed to be negligible.

6.6 Efficiency of Injection & Cell Viability Results

Following laser treatment, cells were collected from the chip collection port (for treated cells) and loading port (for untreated cells) into two separate micro-centrifuge tubes both containing 1 μM of CAM in 250 μl of conditioned DMEM. Cells were incubated (37^{o}C, 5% CO_2) in two separated wells of 96-well Cell Culture Insert Plates (Millipore) for 15 minutes to stain cells with CAM, as well as allowing time for the cells to settle to the bottom of the wells. Next, 200 μl of the surrounding solution was gently removed from both the wells. During this process, extra care was taken in order not to remove any of the cells deposited at the bottom of the plates. Following this, 200 μl of conditioned DMEM was added so as to dilute the CAM to negligible levels and halt the uptake by the cells. The cells were incubated for a further 1 hour before examining PI (uptake due to optical injection and/or cell death) and CAM (indicating the viable cells) fluorescence of both the treated and untreated (control) cells under a fluorescent microscope. Counts of typically 150 cells per experimental run were conducted for the two fluorophores. The cell samples were checked for: a) total number of cells; b) number of PI fluorescing cells; c) number of cells exhibiting both PI and CAM fluorescence. A typical image of the HEK293 cells is shown in Figure 6.7, showing the brightfield, PI and CAM fluorescence images. These images were obtained 24 hours post optical injection, with cells exhibiting healthy growth, division, continued viability and PI fluorescence.

Cell counts were conducted on the collected samples after 1.5 hours in the incubator. Figure 6.8 shows the success rate of optically injecting HEK293 cells using this microfluidic approach. Uptake of purely PI was found to be 42 $\pm$ 8 % compared to a control of 4 $\pm$ 2 %. Taking into account CAM, the proportion of cells that ex-

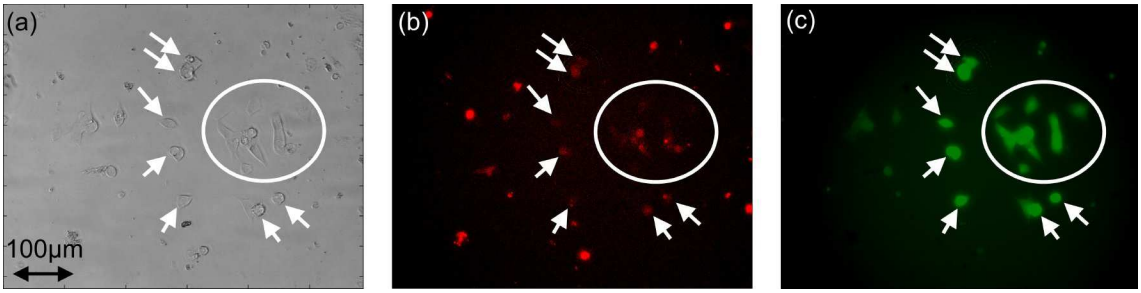

Figure 6.7: *Collected cells 24 hours after microfluidic photoporation, including viable optically injected cells (arrowed and circled). (a) Bright field microscope image showing cell attachment to the base of the well plate. (b) The same cells exhibiting varying levels of PI fluorescence. Strongly red fluorescing cells have uptaken large quantities of PI indicating permanently compromised dead or dying cells. Weakly fluorescing red cells are optically injected. (c) Fluorescence of CAM showing the viable cells in this field of view. The combination of PI fluorescence in (b) and CAM indicates a cell that has been optically injected with PI and has remained viable (arrowed and circled).* [1]

hibited both fluorescence of PI and a strong CAM signal, i.e. cells that are optically injected and viable was 28 ± 4 %, compared to a negligible control. These values are comparable to those obtained in Petri dish experiments, demonstrating that the technique is successful in optically injecting cells with an order of magnitude increase in throughput compared to a manual approach.

6.7 Conclusion

A high throughput photoporation system has been presented, where a microfluidic chip is utilised to deliver cells to a focused fs laser, producing continuous and automated optical injection of a membrane impermeable substance to the cytoplasm of the cell. Throughputs of the order of 1 cell per second were obtained, enabling several thousand viable injected cells per hour, and as such, was the first demonstration of fs-enabled optical injection on this scale. The injection efficiency and viability of the HEK293 mammalian cell line was confirmed using propidium iodide and calcein AM respectively. The injection efficiency using this technique was 42 ± 8 % compared to a control of 4 ± 2 % at a laser power at the focus of 90 mW. Taking into account the requirement for viable cells after injection, the viable injection efficiency was found to be 28 ± 4 %, for cells exhibited both propidium iodide and calcein AM fluorescence. It could be expected that these numbers would increase

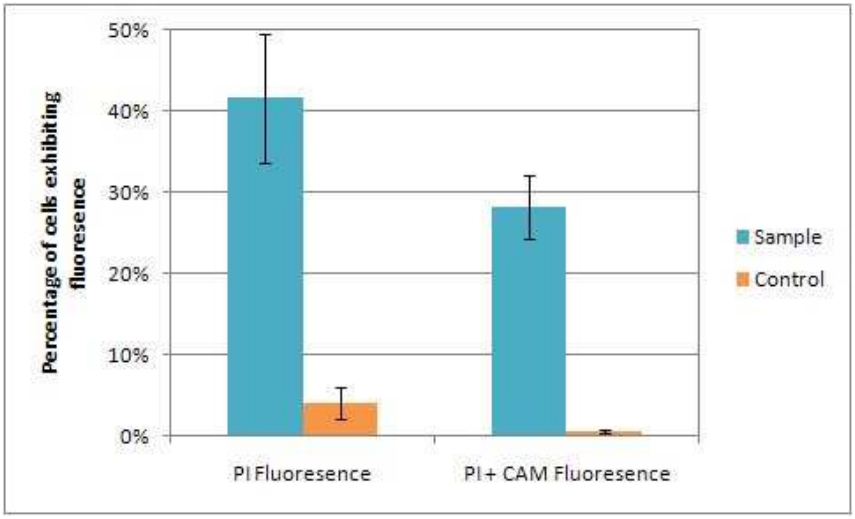

Figure 6.8: *Optical injection efficiencies for HEK293 cells in a microfluidic flow. The percentage of cells exhibiting fluorescence of PI and those that exhibit both PI and CAM is plotted here against those observed in the control samples. Cells exhibiting both PI and CAM are viable after optical injection of PI. Data was obtained 1.5 hours after collection from the chip and error bars are the standard error in the mean of three experimental runs.* [1]

with better positioning of the height of cells through two dimensional hydrodynamic focusing [158] and thus improved targeting of the membrane, or by means of a "diffraction-free" Bessel beam [53]. Flow velocities of $1100 \pm 100\ \mu m s^{-1}$ were used, which in combination with a continuous stream of 4 ms femtosecond laser doses, potentially led to the creation of an array of two to three "photopores" across the cell as it traversed the beam, thus allowing uptake of the surrounding medium.

The work presented here, highlights the possibilities for optical injection as a realistic alternative to other injection techniques such as electroporation [232], microinjection [231], ballistic particle insertion (gene gun) [233], or chemical [234] or viral [235] mediated methods. For the first time, the advantages of microfluidics and fs optical injection [41,53,239,249–259] are combined, to provide a cell injection system with high throughput, high injection efficiencies, and high viability, with cheap, disposable, sterile microfluidic chips for a low (10s μl) sample consumption. Future developments could include the combination with on-chip functionality or other optical techniques, such as Raman [107] or fluorescence spectroscopy [18], or optical landscapes for active or passive sorting [6], before and/or after photoporation. Viability or injection efficiency measurements could be made on the chip and

the sample purified, or by using multiple laser powers, cells could be injected or terminated in a sorting device. The combination of optical injection with on-chip cell culture could also be of particular interest.

The most immediate application of this work will be to cell transfection. Initial tests with inserting plasmid DNA have been attempted but have thus far not yet been successful. This is believed to be down to slow division of the cells for 48 hours immediately after collection from the chip, significantly reducing the likelihood of the plasmid DNA remaining intact, for subsequent uptake into the nucleus during division and eventual expression. In later experiments with PI, the cells were incubated in conditioned medium (media in which cells have previously been cultured, containing secreted growth factors) to counter the low confluency of the collected cells, to encourage them to take to the new environment and progress through their cell cycles. In these samples, cells were seen to be adhered and to have divided after 24 hours, suggesting the cells had fully overcome the experimental procedure and is an encouraging indication to reattempt microfluidic optical transfection.

Contribution

R. Marchington entirely developed the microfluidic chip and fluidic setup. R. Marchington was involved in all data acquisition and analysis, conducted the vast majority of the optical alignment and maintained the Ti:Sapphire laser with X. Tsampoula. The running of the experiment was a two-person effort due to the synchronicity required between cell preparations and fluidic setup. Y. Arita was involved throughout the project, primarily in cell preparations, but also helped fabricating chips, had the idea of the on-chip micro-centrifuge tubes, worked on the optical setup, conducted some preliminary studies into flowing cells, and together we ran the experiment. X. Tsampoula also assisted in the optics, generally helping in the laboratory, contributing to a large number of useful discussions, suggesting the incorporation of the fast shutter, and particularly in the maintenance of the Ti:Sapphire laser and in the cell preparations.

Chapter 7

Conclusions & Future Outlook

7.1 Summary of Thesis

This thesis began with an introduction to optical trapping and tweezers with focus on their use within microfluidic systems. Several examples of optical traps on-chip were detailed, with the dual-beam trap having been most applicable to integration into microfluidic systems, as demonstrated in Chapter 4. Applications of using external free-space optical tweezers within microfluidic environments were reviewed. As well as the interest in immobilising cell-sized objects, the topic of calibration and force measurement was detailed, where an optical trap or tweezers system can be utilised as a sensitive force transducer, as demonstrated using the dual-beam trap in Chapter 4 for studies into the nature of optical bound matter.

Advanced optical beams were explored, including mention of non-diffracting Bessel beams and parabolic Airy beams, and their use in microfluidics, before concentrating on near-field techniques. Three methods of introducing near-field optical fields into microfluidic chips were detailed, that allow the transportation of particles around chips, using externally-introduced light fields with sub-micron overlap with the particles. This is of particular interest for biological samples where exposure to the optical field should be minimised to prevent absorption-mediated photodamage. The use of a total internal reflection microscope objective lens was introduced, which thus far had been utilised for imaging and trapping [75, 77, 78] only, before the work in Chapter 5 was reported [3] on its use for microfluidic optical particle propul-

sion and sorting. The chapter moved on to discuss sorting, and the large array of optical and non-optical techniques available for fractionating microscopic particles. The case for using optical methods was made and both active and passive sorting methods were reviewed, serving as a background to optical chromatography work in Chapter 4 and evanescent optical sorting in Chapter 5.

Chapter 2 looked at the nature of fluid flow when restricted to the micrometre dimensions within microfluidic chips. The governing Navier-Stokes equations were given and with the concept of inertial irrelevance for these low Reynolds number systems, the topic of laminar flow was introduced. The parabolic shape of pressure-driven microfluidic flows was presented, and the technique of hydrodynamic focusing for restricting a sample to a narrow region down a channel was detailed, as utilised in Chapters 5 and 6. The direct influence of the parameters and their implications in the microfluidic chips used throughout this thesis were specified, with the Reynolds number, Péclet number, Poiseuille fluid flow profile and hydrodynamic focusing ratio being calculated for the chips utilised in the experimental chapters. The implications of the non-slip boundary condition to the Stokes fluid drag force for correcting trap stiffness and Q-value measurements in optical traps, and the measured forces of particles propelled by evanescent waves in Chapter 5. Finally, the settling velocity of cells in a chip was calculated, as utilised in chip design considerations for Chapter 6 where cell injection and collection ports are incorporated into the chip.

Chapter 3 introduced soft lithography as the technique for fabricating all the microfluidic chips used in this thesis. The physical and chemical properties of the chip constituent material, PDMS was reviewed in view of its appliance as a mouldable material for microfluidic applications. Methods for physically bonding PDMS to a variety of substrates were discussed, as well as the attachment of silanes to its peripheral surfaces for tailored surface chemistry. The topic of the chip mould was ventured, with the processing steps for SU8 photoepoxy being discussed and the considerations and techniques for successful fabrication being highlighted. Methods for integration of PDMS with optoelectronic components were mentioned and methods for interfacing the microfluidic channels in finalised chips were discussed.

With Chapter 3 as a grounding, Chapter 4 detailed a full protocol for the fa-

brication of PDMS chips. With many points of possible failure in the process, the step by step guide will aid a beginner or advance a novice in the process of soft lithography to produce robust, reproducible chips, which is not currently available in the published literature. The inclusion of some novel additional steps enables the integration of optical fibre onto the mould, allowing beam delivery to be integrated into the chip at the fabrication level and with the micrometre resolutions obtainable in photolithographic processes. This new approach offers alternatives to other methods [17, 21, 24, 25, 31, 32, 133, 191, 196] discussed in the Chapter, and its added flexibility was demonstrated in two applications of the technique. The first was a dual beam fibre trap, where the chip provides inherent alignment of the two optical fibres as necessary for producing a stable trap, and incorporated a microfluidic channel for the insertion of samples. Its use was demonstrated for trapping mammalian cells and for fundamental studies into the nature of light-matter interactions through the optical binding of two colloidal particles [5]. The understanding of the phenomena of optical binding demonstrated in previous works [45, 191, 197–200, 202] was furthered by the measurement of the optical cross interaction between two bound particles in a dual beam trap geometry. The second application utilised for the first time photonic crystal fibre for simultaneous on-chip fluorescence generation and optical chromatography; a sensitive passive sorting technique [125–130] that fractionates particles through the balance of Stokes drag and radiation pressures. Its use in separating dielectric-tagged mammalian cells was also displayed, as verified by on-chip fluoresence, and was the first time the tagging technique [105] had been applied to optical chromatography.

Chapter 5 recounted the first of two larger experimental works of the thesis. The use of an ultra-high numerical aperture microscope objective enabled the generation of evanescent waves through total internal reflection (TIR), and simultaneous imaging of microparticles in response to this optical field. Building on the trapping work utilising such a TIR lens by M. Gu *et al.* [75, 77, 78, 217], this was applied for the first time for the propulsion of particles, and within a microfluidic chip, with the passive separation of particles by size being demonstrated [3]. The phenomenon of TIR, the subsequent appearance of an evanescent field, and the nature of this field

with respect to the incidence angle and polarisation were reviewed. The properties of the TIR microscope lens that make it a suitable choice for near-field trapping and propulsion were analysed, as well as for its more conventional use in fluorescence imaging.

The experimental setup was detailed, along with some practical techniques for measuring the objective transmission and the incident angle after focusing. A theoretical model for the interaction of microparticles with the evanescent field, used a captured image from the experimental setup to generate an expression for the optical field, which in turn was utilised to calculate the optical forces using the Maxwell stress tensor, and predicting qualitatively the nature of the observed light-particle interactions, and was found to be in agreement with a previous model by Almaas *et al.* [222]. The guiding of colloids and cells was demonstrated and using particle tracking software, the velocities as a function of distance and optical power were determined, before exploring the relationship between particle diameter and refractive index.

In the final section of Chapter 5, the fabrication methods of Chapters 3 and 4 were employed to produce a chip to continually deliver particles to the beam through hydrodynamically focusing and passive optical separation of 5 μm polymer spheres were separated from a polydisperse mixture also containing 1 and 3 μm spheres. Although much of the recently published literature in near-field particle propulsion eludes to particle sorting [71, 72, 274, 275], this was the first demonstration of a working example and in a microfluidic format. The chapter placed the work in context with other evanescent guiding methods such as prism geometries [60–62, 64] and waveguides [68, 70–74], particularly in terms of improvements in guiding velocity of the trapped particles using this technique, along with the ease and flexibility of deployment on any microscope system.

In the final experimental chapter, the advantages of microfluidics were combined for the first time with photoporation, to provide a cell injection system with high throughput, high injection efficiencies, and high viability, utilising cheap, disposable, sterile microfluidic chips and an associated low (10s μl) sample consumption. High throughput continuous optical injection of mammalian cells is demonstrated using

the system. The increase in throughput for this automated technique, compared to previous fs photoporation studies [41,53,239,249–259], potentially makes it a realistic alternative to other cell injection techniques, such as electroporation, microinjection, lipofection and viral-mediated methods [231–235], due to the favourable injection efficiencies and post-treatment cell viabilities.

Non-optical techniques for inserting membrane-impermeable agents into the cytoplasm of living cells were reviewed, with a focus on a number of microfluidic systems using electroporation [268–272] and microinjection [266, 267]. The field of photoporation is briefly surveyed, in view of the optical parameters and capabilities of recent examples, including successful cell types and obtained efficiencies to date. The microfluidic system for the experiment was detailed, the most advanced used in the thesis work, employing a number of improvements on that used in the previous chapters. The culture of HEK293 cells and their preparation for the experiment was detailed, before describing the photoporation optical setup and the experimental procedure. Injection results were presented, where several thousand cells could be injected with a dye at a rate of 1 cell/sec, with a Calcein AM test confirming the viabilities after treatment.

7.2 Future Work

7.2.1 Evanescent Guiding and Sorting of Microparticles

In the geometry explored in this thesis, the evanescent guiding direction was fixed, but by changing the position of the illumination spot on the back aperture it is possible to deflect particles in any direction parallel to the substrate (or indeed anywhere in the hemisphere above the focal spot by also employing far-field optical fields). This could enable for instance, particles to be selectively directed into different regions (or microfluidic outlet channels) in an active sorting setup, based on a previously obtained criterion (fluorescence, scattering intensity, Raman spectra etc.). The use of an AOD or SLM to appropriately tailor the optical field at the back aperture could be utilised here.

Another avenue for further studies could be to make use of whispering gallery

modes for enhanced optical guiding velocities and size selectivity. Ng and Chan [274] predict that the optical guiding force is increased up to three orders of magnitude when on resonance. Such an enhancement could yield very specific size selection from a poly-disperse mixture (typical size selectivity of 2.5 nm in the 2.3-2.4 μm range for polymer particles).

Outside of sorting applications, evanescent guiding has applications in optical clearing, where all particles within an area of interest can be guided away. By scanning the sample stage, it was possible to clear several square mm's in a few minutes. This could have applications where a particle of interest is to be isolated from a number of others particles, and could definitely be of use in force measurements using a QPD and optical tweezers, where often a second particle will become trapped mid-measurement, voiding the data acquisition. This could also be utilised in separating rare cells from a larger population in a sample chamber.

The fluidics used for this experiment were still in relatively early stages of development, with flow stability being a huge problem. Short demonstrations of optical sorting were possible and as such were perfectly sufficient in demonstrating a proof of principle sorting concept. For the full capabilities to be assessed however, a large number of trials would need to be conducted and the sorting efficiencies evaluated. The use of push-pull pumping as utilised in Chapter 6 would be a large improvement here.

7.2.1.1 Biological Applications

It would be of utmost interest to apply evanescent sorting to biological samples. The low penetration depth of the evanescent field minimises photodamage compared to far-field approaches. With the large size variance and refractive index ranges in biological samples it could indeed be possible to conduct passive optical sorting using this approach. Rudimentary guiding of red blood cells was demonstrated and exhibited rotation due to their bi-concave shape, possibly indicating that cell dependent guiding and fractionation could be achieved. The separation of blood cells from plasma using this method is definitely a possibility, as large sample areas can be cleared, offering a method for on-chip separation. The use of evanescent waves in

optical-guided neuronal growth [40] is something that could also be explored, which could most readily be applied using a TIR objective.

7.2.2 Photoporation of Cells within Microfluidic Flow

This experiment would greatly benefit from advancements in fabrication techniques. The capabilities to form 3D structures would facilitate 2D hydrodynamic focusing, allowing improved delivery of the particles to the laser beam, all located within similar heights within the parabolic flow profile for a closer range of velocities and thus photoporation doses. Also, the use of a Bessel beam (Section 1.3.1) could be utilised for the improved targeting of the cell membrane. With the use of a Gaussian beam in the work presented, the inefficiencies of correctly hitting all of the cells are encapsulated within the overall "injection efficiency" value. The central core of the Bessel beam, is nearly non-diffracting over a few hundred micrometres, so effectively acts as a rod of light [265]. This removes the requirement of locating the focus of a Gaussian beam within a few micrometres of the membrane, as required for the multi-photon effects. A Bessel beam has been utilised for photoporation in a Petri dish with excellent results [53], and could bring the same benefits to microfluidic methods.

The Bessel beam has also been demonstrated in photoporation using an axicon-tipped fibre for beam delivery [255], which clearly could be encompassed into the chip using the fabrication techniques developed. As the beam would no longer be needed to be manually positioned and focused (as it is done during chip fabrication), this would entirely remove the requirement for the microscope, turning the system into an entirely automated hands-free technique. With the compact fs sources available, the entire system could be miniaturised to the size of a shoebox, which with cartridge-type microfluidic chips, could potentially be an excellent benchtop unit for a bio-laboratory.

7.2.2.1 Biological Applications

Immediate applications for this new technique will be to apply the technique to cell transfection, through the replacement of the injection agent PI used here with a

plasmid DNA, to encode for a fluorescent protein such as DsRed. This increases the reliance on the cells not being hugely disrupted by the experimental procedure, as the time for transport to the nucleus, replication, transcription and expression of the fluorescence is of the order of days (typically 48 hours) compared to minutes with inserted dyes. A number of cell types could be tried, including primary neuronal cells, stem cells, fungi (such as yeast), and bacteria. There is also much interest in using photoporation for injecting pathogenic cell types. Due to the dangers involved, precautionary measures prevent the use of many other transfection techniques and the use of sharps (such as microinjection needles) are prohibited. Live micro-organisms could also be attempted, such as the model organism *C. elegans* roundworm, which has previously been manipulated on-chip [276], but not photoporated. The large and accessible neurons of the C. *elegans* could allow photoporation of these cells within a species *in vivo* for the first time. Microfluidics could add absolute control of the fluid surroundings for on-chip culture. Photoporating tissue is also of interest, and another step towards *in vivo* application.

As the cells do not need to be adhered to the base of a glass-bottomed (i.e. coverslip) Petri dish, the approach of microfluidic delivery opens up the possibilities for photoporating non-adherent cell types. Typically in static photoporation, a region of interest is marked and adhered cells are photoporated in this region only, allowing the user to check the exact same cells hours or days later to monitor their progress and/or fluorescence. Non-adherent cells in this situation pose a problem as they are entirely free to move around, so without dosing a very large proportion of cells in the entire dish, working with a very small and isolated sample volume, or a very under-confluent sample (all of which normally prove quite impractical), it is not entirely possible. The microfluidic approach is in fact easier for non-adherent cells as the preparations before the experiment become much faster and less stressful on the cells (no need for trypsinisation). A number of cell types could be attempted, potentially including non-adherent stem cells.

As observed when the laser power was increased by even 20%, focused femtosecond light is capable of opening more permanent holes in the membrane. Cells were observed to split open and empty their contents, obviously leading to subsequent

death. This could be utilised in controlled lysis of cells [277], possibly in some microfluidic format for subsequent on-chip PCR [278]. On-chip cell culture could also be incorporated [279] for long term studies without the removal of the cells from the chip. Combining photoporation with optical sorting could also be fruitful; allowing the separation of specific cells for treatment from a clinical sample, fractionating successful cells after treatment, or as part of a larger process of injecting multiple agents.

Bibliography

[1] R. F. Marchington, Y. Arita, X. Tsampoula, F. Gunn-Moore, and K. Dholakia, "High throughput optical injection of mammalian cells using a microfluidic platform," *Biomedical Optics Express* **1**(2), pp. 527–536, 2010.

[2] P. C. Ashok, R. F. Marchington, P. Mthunzi, T. F. Krauss, and K. Dholakia, "Optical chromatography using a photonic crystal fiber with on-chip fluorescence excitation," *Optics Express* **18**(6), pp. 6396–6407, 2010.

[3] R. F. Marchington, M. Mazilu, S. Kuriakose, V. Garcés-Chávez, P. J. Reece, T. F. Krauss, M. Gu, and K. Dholakia, "Optical deflection and sorting of microparticles in a near-field optical geometry," *Optics Express* **16**(6), pp. 3712–3726, 2008.

[4] W. M. Lee, P. J. Reece, R. F. Marchington, N. K. Metzger, and K. Dholakia, "Construction and calibration of an optical trap on a fluorescence optical microscope.," *Nature Protocols* **2**(12), pp. 3226–3238, 2007.

[5] N. K. Metzger, R. F. Marchington, M. Mazilu, R. L. Smith, K. Dholakia, and E. M. Wright, "Measurement of the restoring forces acting on two optically bound particles from normal mode dorrelations," *Physical Review Letters* **98**(6), p. 068102, 2007.

[6] K. Dholakia, W. M. Lee, L. Paterson, M. P. Macdonald, R. Mcdonald, I. Andreev, P. Mthunzi, C. T. A. Brown, R. F. Marchington, and A. C. Riches, "Optical separation of cells on potential energy landscapes: enhancement with dielectric tagging," *IEEE Journal of Selected Topics in Quantum Electronics* **13**(6), pp. 1646–1654, 2007.

[7] R. F. Marchington, Y. Arita, D. Stevenson, F. Gunn-Moore, and K. Dholakia, "High throughput photoporation of mammalian cells using microfluidic cell delivery," in *CLEO, San Jose*, (JMC6), 2010.

[8] Y. Arita, R. Marchington, D. Stevenson, F. Gunn-Moore, and K. Dholakia, "High Throughput Photoporation of Mammalian Cells using Microfluidic Cell Delivery," in *Biomedical Optics*, (BTuD92), OSA, (Miami, Florida, USA), 2010.

[9] P. C. Ashok, R. F. Marchington, M. Mazilu, T. F. Krauss, and K. Dholakia, "Towards integrated optical chromatography using photonic crystal fiber," in *Proceedings of SPIE*, **44**(74000R), SPIE, (San Diego, CA, USA), 2009.

[10] D. M. Gherardi, A. E. Carruthers, T. Cizmar, R. F. Marchington, and K. Dholakia, "Novel dual beam fiber traps using endlessly single-mode photonic crystal fiber," in *Proceedings of SPIE*, (703828), SPIE, (San Diego, CA, USA), 2008.

[11] The University of St Andrews, R. Marchington, P. Ashok, and K. Dholakia, "Optical trap," Marks & Clerk, Glasgow, G2 7JS, UK, Applied 2010.

[12] A. Ashkin, "Acceleration and trapping of particles by radiation pressure," *Physical Review Letters* **24**, pp. 156–159, Jan 1970.

[13] C. Monat, P. Domachuk, and B. J. Eggleton, "Integrated optofluidics: A new river of light," *Nature Photonics* **1**, pp. 106–114, Feb. 2007.

[14] P. R. T. Jess, V. Garcés-Chávez, A. C. Riches, C. S. Herrington, and K. Dholakia, "Simultaneous raman micro-spectroscopy of optically trapped and stacked cells," *Journal of Raman Spectroscopy* **38**(9), pp. 1082–1088, 2007.

[15] E. Eriksson, J. Enger, B. Nordlander, N. Erjavec, K. Ramser, M. Goksör, S. Hohmann, T. Nyström, and D. Hanstorp, "A microfluidic system in combination with optical tweezers for analyzing rapid and reversible cytological alterations in single cells upon environmental changes.," *Lab on a Chip* **7**, pp. 71–76, January 2007.

[16] S. J. Cran-McGreehin, T. F. Krauss, and K. Dholakia, "Integrated monolithic optical manipulation," *Lab on a Chip* **6**(9), pp. 1122–1124, 2006.

[17] P. Domachuk, M. Cronin-golomb, B. J. Eggleton, S. Mutzenich, G. Rosengarten, and A. Mitchell, "Application of optical trapping to beam manipulation in optofluidics," *Optics Express* **13**(19), pp. 7265–7275, 2006.

[18] M. M. Wang, E. Tu, D. E. Raymond, J. M. Yang, H. C. Zhang, N. Hagen, B. Dees, E. M. Mercer, A. H. Forster, I. Kariv, P. J. Marchand, and W. F. Butler, "Microfluidic sorting of mammalian cells by optical force switching," *Nature Biotechnology* **23**(1), pp. 83–87, 2005.

[19] M. L. Cordero, D. R. Burnham, C. N. Baroud, and D. McGloin, "Thermocapillary manipulation of droplets using holographic beam shaping: Microfluidic pin ball," *Applied Physics Letters* **93**(3), p. 034107, 2008.

[20] M. R. de Saint Vincent, R. Wunenburger, and J.-P. Delville, "Laser switching and sorting for high speed digital microfluidics," *Applied Physics Letters* **92**(15), p. 154105, 2008.

[21] A. Constable, J. Kim, J. Mervis, F. Zarinetchi, and M. Prentiss, "Demonstration of a-fiber-optical light-force trap," *Optics Letters* **18**(21), pp. 1867–1869, 1993.

[22] E. Hecht, *Optics (International Edition)*, Pearson Education, 4 ed., 2003.

[23] S. Kühn, E. J. Lunt, B. S. Phillips, A. R. Hawkins, and H. Schmidt, "Optofluidic particle concentration by a long-range dual-beam trap," *Optics Letters* **34**(15), pp. 2306–2308, 2009.

[24] P. R. T. Jess, V. Garcés-Chávez, D. Smith, M. Mazilu, L. Paterson, A. Riches, C. S. Herrington, W. Sibbett, and K. Dholakia, "Dual beam fibre trap for raman micro-spectroscopy of single cells," *Optics Express* **14**(12), pp. 5779–5791, 2006.

[25] D. Rudd, C. López-Mariscal, M. Summers, A. Shahvisi, J. C. Gutiérrez-Vega, and D. McGloin, "Fiber based optical trapping of aerosols," *Optics Express* **16**(19), pp. 14550–14560, 2008.

[26] S. Kühn, B. S. Phillips, E. J. Lunt, A. R. Hawkins, and H. Schmidt, "Ultralow power trapping and fluorescence detection of single particles on an optofluidic chip," *Lab on a Chip* **10**(2), pp. 189–194, 2010.

[27] M. K. Kreysing, T. Kieβling, A. Fritsch, C. Dietrich, J. R. Guck, and J. A. Käs, "The optical cell rotator," *Optics Express* **16**(21), pp. 16984–16992, 2008.

[28] F. Lautenschläger, S. Paschke, S. Schinkinger, A. Bruel, M. Beil, and J. Guck, "The regulatory role of cell mechanics for migration of differentiating myeloid cells," *Proceedings of the National Academy of Sciences of the United States of America* **106**(37), pp. 15696–15701, 2009.

[29] T. W. Remmerbach, F. Wottawah, J. Dietrich, B. Lincoln, C. Wittekind, and J. Guck, "Oral cancer diagnosis by mechanical phenotyping," *Cancer Research* **69**(5), pp. 1728–1732, 2009.

[30] D. M. Gherardi, A. E. Carruthers, T. Čižmár, E. M. Wright, and K. Dholakia, "A dual beam photonic crystal fiber trap for microscopic particles," *Applied Physics Letters* **93**(4), p. 041110, 2008.

[31] S. D. Collins, R. J. Baskin, and D. G. Howitt, "Microinstrument gradient-force optical trap," *Applied Optics* **38**(28), pp. 6068–6074, 1999.

[32] M. Wei, K. Yang, A. Karmenyan, and A. Chiou, "Three-dimensional optical force field on a Chinese hamster ovary cell in a fiber-optical dual-beam trap," *Optics Express* **14**(7), pp. 3056–3064, 2006.

[33] N. Bellini, K. C. Vishnubhatla, F. Bragheri, L. Ferrara, P. Minzioni, R. Ramponi, I. Cristiani, and R. Osellame, "Femtosecond laser fabricated monolithic chip for optical trapping and stretching of single cells," *Optics Express* **18**(5), pp. 4679–4688, 2010.

[34] A. Ashkin, J. M. Dziedzic, J. E. Bjorkholm, and S. Chu, "Observation of a single-beam gradient force optical trap for dielectric particles," *Optics Letters* **11**(5), pp. 288–290, 1986.

[35] P. N. Prasad, *Introduction to Biophotonics*, Wiley-Interscience, 2003.

[36] K. Dholakia, P. Reece, and M. Gu, "Optical micromanipulation.," *Chemical Society Reviews* **37**, pp. 42–55, 2008.

[37] L. R. Huang, E. C. Cox, R. H. Austin, and J. C. Sturm, "Continuous particle separation through deterministic lateral displacement," *Science (New York, N.Y.)* **304**(5673), pp. 987–990, 2004.

[38] A. Yao, M. Tassieri, M. Padgett, and J. Cooper, "Microrheology with optical tweezers," *Lab on a Chip* **9**(17), pp. 2568–2575, 2009.

[39] D. R. Burnham, G. D. Wright, N. D. Read, and D. McGloin, "Holographic and single beam optical manipulation of hyphal growth in filamentous fungi," *Journal of Optics A: Pure and Applied Optics* **9**(8), p. S172, 2007.

[40] D. J. Carnegie, D. J. Stevenson, M. Mazilu, F. Gunn-Moore, and K. Dholakia, "Guided neuronal growth using optical line traps," *Optics Express* **16**(14), pp. 10507–10517, 2008.

[41] C. McDougall, D. J. Stevenson, C. T. A. Brown, F. Gunn-Moore, and K. Dholakia, "Targeted optical injection of gold nanoparticles into single mammalian cells," *Journal of Biophotonics* **2**(12), pp. 736–743, 2009.

[42] J. Finer, R. Simmons, and J. Spudich, "Single myosin molecule mechanics: piconewton forces and nanometre steps," *Nature* **368**(6467), pp. 113–119, 1994.

[43] R. J. Davenport, G. Wuite, R. Landick, and C. Bustamante, "Single-molecule study of transcriptional pausing and arrest by E. coli RNA polymerase," *Science* **287**(5462), pp. 2497–2500, 2000.

[44] E. A. Abbondanzieri, W. J. Greenleaf, J. W. Shaevitz, R. Landick, and S. M. Block, "Direct observation of base-pair stepping by rna polymerase," *Nature* **438**(7067), pp. 460–465, 2005.

[45] N. K. Metzger, K. Dholakia, and E. M. Wright, "Observation of bistability and hysteresis in optical binding of two dielectric spheres," *Physical Review Letters* **96**(6), p. 068102, 2006.

[46] J. Wu, D. Day, and M. Gu, "Shear stress mapping in microfluidic devices by optical tweezers," *Optics Express* **18**(8), pp. 7611–7616, 2010.

[47] G. Milne, *Optical Sorting and Manipulation of Microscopic Particles*. PhD thesis, School of Physics & Astronomy, University of St Andrews, 2007.

[48] K. Svoboda and S. Block, "Biological applications of optical forces," *Annual Review of Biophysics and Biomolecular Structure* **23**(1), pp. 247–285, 1994.

[49] S. Parkin, G. Knöner, T. Nieminen, N. Heckenberg, and H. Rubinsztein-Dunlop, "Picoliter viscometry using optically rotated particles," *Physical Review E* **76**(4), p. 041507, 2007.

[50] L. Z. Shi, J. M. Nascimento, C. Chandsawangbhuwana, E. L. Botvinick, and M. W. Berns, "An automatic system to study sperm motility and energetics," *Biomedical Microdevices* **10**(4), pp. 573–583, 2008.

[51] G. Milne, "Labview pattern-matching particle tracker software," http://faculty.washington.edu/gmilne/tracker.htm, 2007.

[52] D. McGloin and K. Dholakia, "Bessel beams: diffraction in a new light," *Contemporary Physics* **46**(1), pp. 15–28, 2005.

[53] X. Tsampoula, V. Garces-Chavez, M. Comrie, D. J. Stevenson, B. Agate, C. T. A. Brown, F. Gunn-Moore, and K. Dholakia, "Femtosecond cellular transfection using a nondiffracting light beam," *Applied Physics Letters* **91**(5), p. 053902, 2007.

[54] J. Baumgartl, M. Mazilu, and K. Dholakia, "Optically mediated particle clearing using Airy wavepackets," *Nature Photonics* **2**(11), pp. 675–678, 2008.

[55] J. Baumgartl, G. M. Hannappel, D. J. Stevenson, D. Day, M. Gu, and K. Dholakia, "Optical redistribution of microparticles and cells between microwells," *Lab on a Chip* **9**(10), pp. 1334–1336, 2009.

[56] N. Simpson, K. Dholakia, L. Allen, and M. Padgett, "Mechanical equivalence of spin and orbital angular momentum of light: an optical spanner," *Optics Letters* **22**(1), pp. 52–54, 1997.

[57] P. Prentice, M. Macdonald, T. Frank, A. Cuschier, G. Spalding, W. Sibbett, P. Campbell, and K. Dholakia, "Manipulation and filtration of low index particles with holographic Laguerre-Gaussian optical trap arrays," *Optics Express* **12**(4), pp. 593–600, 2004.

[58] P. Prentice, A. Cuschieri, K. Dholakia, M. Prausnitz, and P. Campbell, "Membrane disruption by optically controlled microbubble cavitation," *Nature Physics* **1**(2), pp. 107–110, 2005.

[59] M. Dienerowitz, M. Mazilu, P. J. Reece, T. F. Krauss, and K. Dholakia, "Optical vortex trap for resonant confinement of metal nanoparticles," *Optics Express* **16**(7), pp. 4991–4999, 2008.

[60] S. Kawata and T. Sugiura, "Movement of micrometer-sized particles in the evanescent field of a laser beam," *Optics Letters* **17**(11), pp. 772–774, 1992.

[61] R. J. Oetama and J. Y. Walz, "Translation of colloidal particles next to a flat plate using evanescent waves," *Colloids and Surfaces A - Physicochemical and Engineering Aspects* **211**(2-3), pp. 179–195, 2002.

[62] V. Garcés-Chávez, K. Dholakia, and G. C. Spalding, "Extended-area optically induced organization of microparticies on a surface," *Applied Physics Letters* **86**(3), p. 031106, 2005.

[63] V. Garcés-Chávez, R. Quidant, P. J. Reece, G. Badenes, L. Torner, and K. Dholakia, "Extended organization of colloidal microparticles by surface

plasmon polariton excitation," *Physical Review B - Condensed Matter and Materials Physics* **73**(8), p. 085417, 2006.

[64] P. J. Reece, V. Garcés-Chávez, and K. Dholakia, "Near-field optical micromanipulation with cavity enhanced evanescent waves," *Applied Physics Letters* **88**(22), p. 221116, 2006.

[65] M. Šiler, T. Čižmár, M. Šerý, and P. Zemánek, "Optical forces generated by evanescent standing waves and their usage for sub-micron particle delivery," *Applied Physics B-Lasers and Optics* **84**(1-2), pp. 157–165, 2006.

[66] T. Čižmár, M. Šiler, M. Šerý, P. Zemánek, V. Garcés-Chávez, and K. Dholakia, "Optical sorting and detection of submicrometer objects in a motional standing wave," *Physical Review B* **74**(3), p. 035105, 2006.

[67] M. Ploschner, M. Mazilu, T. F. Krauss, and K. Dholakia, "Optical forces near a nanoantenna," *Journal of Nanophotonics* **4**(1), p. 041570, 2010.

[68] S. Kawata and T. Tani, "Optically driven mie particles in an evanescent field along a channeled waveguide," *Optics Letters* **21**(21), pp. 1768–1770, 1996.

[69] K. Grujic, O. Hellesø, J. Wilkinson, and J. Hole, "Optical propulsion of microspheres along a channel waveguide produced by cs+ ion-exchange in glass," *Optics Communications* **239**(4-6), pp. 227 – 235, 2004.

[70] S. Gaugiran, S. Getin, J. M. Fedeli, G. Colas, A. Fuchs, F. Chatelain, and J. Derouard, "Optical manipulation of microparticles and cells on silicon nitride waveguides," *Optics Express* **13**(18), pp. 6956–6963, 2005.

[71] K. Grujic, O. G. Hellesø, J. P. Hole, and J. S. Wilkinson, "Sorting of polystyrene microspheres using a y-branched optical waveguide," *Optics Express* **13**(1), pp. 1–7, 2005.

[72] B. S. Schmidt, A. H. J. Yang, D. Erickson, and M. Lipson, "Optofluidic trapping and transport on solid core waveguides within a microfluidic device," *Optics Express* **15**(22), pp. 14322–14334, 2007.

[73] A. H. J. Yang and D. Erickson, "Optofluidic ring resonator switch for optical particle transport," *Lab on a Chip* **10**(6), pp. 769–774, 2010.

[74] G. Brambilla, G. S. Murugan, J. S. Wilkinson, and D. J. Richardson, "Optical manipulation of microspheres along a subwavelength optical wire," *Optics Letters* **32**(20), pp. 3041–3043, 2007.

[75] M. Gu, J. B. Haumonte, Y. Micheau, J. W. M. Chon, and X. S. Gan, "Laser trapping and manipulation under focused evanescent wave illumination," *Applied Physics Letters* **84**(21), pp. 4236–4238, 2004.

[76] D. Ganic, X. S. Gan, and M. Gu, "Trapping force and optical lifting under focused evanescent wave illumination," *Optics Express* **12**(22), pp. 5533–5538, 2004.

[77] M. Gu, S. Kuriakose, and X. Gan, "A single beam near-field laser trap for optical stretching, folding and rotation of erythrocytes," *Optics Express* **15**(3), pp. 1369–1375, 2007.

[78] S. Kuriakose, D. Morrish, X. Gan, J. W. M. Chon, K. Dholakia, and M. Gu, "Near-field optical trapping with an ultrashort pulsed laser beam," *Applied Physics Letters* **92**(8), p. 081108, 2008.

[79] W. Bonner, H. Hulett, R. Sweet, and L. Herzenberg, "Fluorescence activated cell sorting," *Review of Scientific Instruments* **43**(3), pp. 404–409, 1972.

[80] S. F. Ibrahim and G. Engh, "High-speed cell sorting: fundamentals and recent advances," *Current Opinion in Biotechnology* **14**(1), pp. 5–12, 2003.

[81] N. Pamme, "Continuous flow separations in microfluidic devices," *Lab on a Chip* **7**(12), pp. 1644–1659, 2007.

[82] D. Huh, W. Gu, Y. Kamotani, J. B. Grotberg, and S. Takayama, "Microfluidics for flow cytometric analysis of cells and particles," *Physiological Measurement* **26**(3), p. R73, 2005.

[83] J. Vykoukal, D. M. Vykoukal, S. Freyberg, E. U. Alt, and P. R. C. Gascoyne, "Enrichment of putative stem cells from adipose tissue using dielectrophoretic field-flow fractionation," *Lab on a Chip* **8**(8), pp. 1386–1393, 2008.

[84] S. Choi, S. Song, C. Choi, and J.-K. Park, "Microfluidic self-sorting of mammalian cells to achieve cell cycle synchrony by hydrophoresis," *Analytical Chemistry* **81**(5), pp. 1964–1968, 2009.

[85] R. Gorkin, J. Park, J. Siegrist, M. Amasia, B. S. Lee, J.-M. Park, J. Kim, H. Kim, M. Madou, and Y.-K. Cho, "Centrifugal microfluidics for biomedical applications," *Lab on a Chip* **10**(14), pp. 1758–1773, 2010.

[86] A. P. Wong, M. Gupta, S. S. Shevkoplyas, and G. M. Whitesides, "Egg beater as centrifuge: isolating human blood plasma from whole blood in resource-poor settings," *Lab on a Chip* **8**(12), pp. 2032–2037, 2008.

[87] D. L. Siegel, T. Y. Chang, S. L. Russell, and V. Y. Bunya, "Isolation of cell surface-specific human monoclonal antibodies using phage display and magnetically-activated cell sorting: applications in immunohematology," *Journal of Immunological Methods* **206**(1-2), pp. 73–85, 1997.

[88] C. Liu, T. Stakenborg, S. Peeters, and L. Lagae, "Cell manipulation with magnetic particles toward microfluidic cytometry," *Journal of Applied Physics* **105**(10), p. 102014, 2009.

[89] H. Lee, Y. Liu, D. Ham, and R. M. Westervelt, "Integrated cell manipulation system–CMOS/microfluidic hybrid," *Lab on a Chip* **7**(3), pp. 331–337, 2007.

[90] J. Giddings, F. Yang, and M. Myers, "Flow-field-flow fractionation: a versatile new separation method," *Science* **193**(4259), pp. 1244–1245, 1976.

[91] P. Reschiglian, A. Zattoni, B. Roda, E. Michelini, and A. Roda, "Field-flow fractionation and biotechnology," *Trends in Biotechnology* **23**(9), pp. 475–483, 2005.

[92] J. Yang, Y. Huang, X. B. Wang, F. F. Becker, and P. R. Gascoyne, "Differential analysis of human leukocytes by dielectrophoretic field-flow-fractionation," *Biophysical Journal* **78**(5), pp. 2680–2689, 2000.

[93] S. Choi, S. Song, C. Choi, and J. Park, "Continuous blood cell separation by hydrophoretic filtration," *Lab on a Chip* **7**(11), pp. 1532–1538, 2007.

[94] C. F. Chou, O. Bakajin, S. W. Turner, T. a. Duke, S. S. Chan, E. C. Cox, H. G. Craighead, and R. H. Austin, "Sorting by diffusion: an asymmetric obstacle course for continuous molecular separation," *Proceedings of the National Academy of Sciences of the United States of America* **96**(24), pp. 13762–13765, 1999.

[95] M. Yamada, M. Nakashima, and M. Seki, "Pinched flow fractionation: continuous size separation of particles utilizing a laminar flow profile in a pinched microchannel," *Analytical Chemistry* **76**(18), pp. 5465–5471, 2004.

[96] G. E. Karniadakis and A. Beskok, *Micro Flows: Fundamentals and Simulation*, Springer, 2002.

[97] P. Gascoyne and J. Vykoukal, "Particle separation by dielectrophoresis," *Electrophoresis* **23**(13), pp. 1973–1983, 2002.

[98] T. P. Hunt, D. Issadore, and R. M. Westervelt, "Integrated circuit/microfluidic chip to programmably trap and move cells and droplets with dielectrophoresis," *Lab on a Chip* **8**(1), pp. 81–87, 2008.

[99] S. L. Neale, A. T. Ohta, H.-Y. Hsu, J. K. Valley, A. Jamshidi, and M. C. Wu, "Trap profiles of projector based optoelectronic tweezers (OET) with HeLa cells," *Optics Express* **17**(7), pp. 5232–5239, 2009.

[100] R. S. Thomas, H. Morgan, and N. G. Green, "Negative DEP traps for single cell immobilisation," *Lab on a Chip* **9**(11), pp. 1534–1540, 2009.

[101] P. Y. Chiou, A. T. Ohta, and M. C. Wu, "Massively parallel manipulation of single cells and microparticles using optical images," *Nature* **436**(7049), pp. 370–372, 2005.

[102] K.-H. Han and A. B. Frazier, "Lateral-driven continuous dielectrophoretic microseparators for blood cells suspended in a highly conductive medium," *Lab on a Chip* **8**(7), pp. 1079–1086, 2008.

[103] U. Kim, J. Qian, S. a. Kenrick, P. S. Daugherty, and H. T. Soh, "Multitarget dielectrophoresis activated cell sorter.," *Analytical Chemistry* **80**(22), pp. 8656–8661, 2008.

[104] X. Hu, P. H. Bessette, J. Qian, C. D. Meinhart, P. S. Daugherty, and H. T. Soh, "Marker-specific sorting of rare cells using dielectrophoresis," *Proceedings of the National Academy of Sciences of the United States of America* **102**(44), pp. 15757–15761, 2005.

[105] P. Mthunzi, W. M. Lee, A. C. Riches, C. T. A. Brown, F. J. Gunn-Moore, and K. Dholakia, "Intracellular Dielectric Tagging for Improved Optical Manipulation of Mammalian Cells," *IEEE Journal of Selected Topics in Quantum Electronics* **16**(3), pp. 608–618, 2010.

[106] T. Hatano, T. Kaneta, and T. Imasaka, "Application of Optical Chromatography to Immunoassay," *Analytical Chemistry* **69**(14), pp. 2711–2715, 1997.

[107] A. Y. Lau, L. P. Lee, and J. W. Chan, "An integrated optofluidic platform for Raman-activated cell sorting," *Lab on a Chip* **8**(7), pp. 1116–1120, 2008.

[108] A. Mittag and A. Tárnok, "Basics of standardization and calibration in cytometry–a review," *Journal of Biophotonics* **2**(8-9), pp. 470–481, 2009.

[109] A. Fu, C. Spence, A. Scherer, F. Arnold, and S. Quake, "A microfabricated fluorescence-activated cell sorter," *Nature Biotechnology* **17**(11), pp. 1109–1111, 1999.

[110] T. D. Perroud, J. N. Kaiser, J. C. Sy, T. W. Lane, C. S. Branda, A. K. Singh, and K. D. Patel, "Microfluidic-based cell sorting of Francisella tularensis infected macrophages using optical forces," *Analytical Chemistry* **80**(16), pp. 6365–6372, 2008.

[111] J.-C. Baret, O. J. Miller, V. Taly, M. Ryckelynck, A. El-Harrak, L. Frenz, C. Rick, M. L. Samuels, J. B. Hutchison, J. J. Agresti, D. R. Link, D. A. Weitz, and A. D. Griffiths, "Fluorescence-activated droplet sorting (FADS): efficient microfluidic cell sorting based on enzymatic activity.," *Lab on a Chip* **9**(13), pp. 1850–1858, 2009.

[112] S. H. Cho, C. H. Chen, F. S. Tsai, J. M. Godin, and Y.-H. Lo, "Human mammalian cell sorting using a highly integrated micro-fabricated fluorescence-activated cell sorter (muFACS)," *Lab on a Chip* **10**(12), pp. 1567–1573, 2010.

[113] L. Johansson, F. Nikolajeff, S. Johansson, and S. Thorslund, "On-chip fluorescence-activated cell sorting by an integrated miniaturized ultrasonic transducer," *Analytical Chemistry* **81**(13), pp. 5188–5196, 2009.

[114] A. Wolff, I. R. Perch-Nielsen, U. D. Larsen, P. Friis, G. Goranovic, C. R. Poulsen, J. P. Kutter, and P. Telleman, "Integrating advanced functionality in a microfabricated high-throughput fluorescent-activated cell sorter," *Lab on a Chip* **3**(1), pp. 22–27, 2003.

[115] M. Andersson, A. Madgavkar, M. Stjerndahl, Y. Wu, W. Tan, R. Duran, S. Niehren, K. Mustafa, K. Arvidson, and A. Wennerberg, "Using optical tweezers for measuring the interaction forces between human bone cells and implant surfaces: System design and force calibration," *Review of Scientific Instruments* **78**(7), p. 074302, 2007.

[116] M. Wang, N. Jing, I.-H. Chou, G. L. Cote, and J. Kameoka, "An optofluidic device for surface enhanced Raman spectroscopy," *Lab on a Chip* **7**(5), pp. 630–632, 2007.

[117] R. Wilson, S. A. Bowden, J. Parnell, and J. M. Cooper, "Signal enhancement of surface enhanced Raman scattering and surface enhanced resonance Raman scattering using in situ colloidal synthesis in microfluidics," *Analytical Chemistry* **82**(5), pp. 2119–2123, 2010.

[118] M. Mazilu, A. C. De Luca, A. Riches, C. S. Herrington, and K. Dholakia, "Optimal algorithm for fluorescence suppression of modulated Raman spectroscopy," *Optics Express* **18**(11), p. 11382, 2010.

[119] K. R. Strehle, D. Cialla, P. Rösch, T. Henkel, M. Köhler, and J. Popp, "A reproducible surface-enhanced raman spectroscopy approach. Online SERS measurements in a segmented microfluidic system," *Analytical Chemistry* **79**(4), pp. 1542–1547, 2007.

[120] C. H. Camp, S. Yegnanarayanan, A. A. Eftekhar, H. Sridhar, and A. Adibi, "Multiplex coherent anti-Stokes Raman scattering (MCARS) for chemically sensitive, label-free flow cytometry," *Optics Express* **17**(25), pp. 119–128, 2009.

[121] L. Paterson, E. Papagiakoumou, G. Milne, V. Garcés-Chávez, S. A. Tatarkova, W. Sibbett, F. J. Gunn-Moore, P. E. Bryant, A. C. Riches, and K. Dholakia, "Light-induced cell separation in a tailored optical landscape," *Applied Physics Letters* **87**(12), p. 123901, 2005.

[122] M. P. MacDonald, G. C. Spalding, and K. Dholakia, "Microfluidic sorting in an optical lattice," *Nature* **426**(6965), pp. 421–424, 2003.

[123] G. Milne, D. Rhodes, M. MacDonald, and K. Dholakia, "Fractionation of polydisperse colloid with acousto-optically generated potential energy landscapes," *Optics Letters* **32**(9), pp. 1144–1146, 2007.

[124] I. Ricardez-Vargas, P. Rodriguez-Montero, R. Ramos-Garcia, and K. Volke-Sepulveda, "Modulated optical sieve for sorting of polydisperse microparticles," *Applied Physics Letters* **88**(12), p. 121116, 2006.

[125] J. Makihara, T. Kaneta, and T. Imasaka, "Optical chromatography: Size determination by eluting particles," *Talanta* **48**(3), pp. 551–557, 1999.

[126] T. Imasaka, Y. Kawabata, T. Kaneta, and Y. Ishidzu, "Optical chromatography," *Analytical Chemistry* **67**(11), pp. 1763–1765, 1995.

[127] S. J. Hart and A. V. Terray, "Refractive-index-driven separation of colloidal polymer particles using optical chromatography," *Applied Physics Letters* **83**(25), pp. 5316–5318, 2003.

[128] S. J. Hart, A. Terray, T. A. Leski, J. Arnold, and R. Stroud, "Discovery of a significant optical chromatographic difference between spores of bacillus anthracis and its close relative, bacillus thuringiensis," *Analytical Chemistry* **78**(9), pp. 3221–3225, 2006.

[129] T. Kaneta, Y. Ishidzu, N. Mishima, and T. Imasaka, "Theory of optical chromatography," *Analytical Chemistry* **69**(14), pp. 2701–2710, 1997.

[130] S. Miki, T. Kaneta, and T. Imasaka, "Visualization of an immunological reaction between single antigen and antibody molecules by optical chromatography," *Analytica Chimica Acta* **404**(1), pp. 1–6, 2000.

[131] N. Mishima, T. Kaneta, and T. Imasaka, "The "optical funnel". a technique for measuring a microorganism's power," *Analytical Chemistry* **70**(16), pp. 3513–3515, 1998.

[132] T. Kaneta, N. Mishima, and T. Imasaka, "Determination of motility forces of bovine sperm cells using an "optical funnel"," *Analytical Chemistry* **72**(11), pp. 2414–2417, 2000.

[133] J. Guck, R. Ananthakrishnan, H. Mahmood, T. J. Moon, C. C. Cunningham, and J. Kas, "The Optical Stretcher: A Novel Laser Tool to Micromanipulate Cells," *Biophysical Journal* **81**(2), pp. 767–784, 2001.

[134] T. Kaneta, J. Makihara, and T. Imasaka, "An "optical channel": A technique for the evaluation of biological cell elasticity," *Analytical Chemistry* **73**(24), pp. 5791–5795, 2001.

[135] A. Terray, J. Arnold, and S. J. Hart, "Enhanced optical chromatography in a pdms microfluidic system," *Optics Express* **13**(25), pp. 10406–10415, 2005.

[136] S. J. Hart, A. V. Terray, and J. Arnold, "Particle separation and collection using an optical chromatographic filter," *Applied Physics Letters* **91**(17), p. 171121, 2007.

[137] A. Terray, H. D. Ladouceur, M. Hammond, and S. J. Hart, "Numerical simulation of an optical chromatographic separator," *Optics Express* **17**(3), pp. 2024–2032, 2009.

[138] M. MacDonald, S. Neale, L. Paterson, A. Richies, K. Dholakia, and G. Spalding, "Cell cytometry with a light touch: sorting microscopic matter with an optical lattice," *Journal of Biological Regulators and Homeostatic Agents* **18**(2), pp. 200–205, 2004.

[139] G.-B. Liao, P. B. Bareil, Y. Sheng, and A. Chiou, "One-dimensional jumping optical tweezers for optical stretching of bi-concave human red blood cells," *Optics Express* **16**(3), pp. 1996–2004, 2008.

[140] A. Gopinathan and D. Grier, "Statistically locked-in transport through periodic potential landscapes," *Physical Review Letters* **92**(13), p. 130602, 2004.

[141] P. T. Korda, M. B. Taylor, and D. G. Grier, "Kinetically Locked-In Colloidal Transport in an Array of Optical Tweezers," *Physical Review Letters* **89**(12), p. 128301, 2002.

[142] K. Xiao and D. G. Grier, "Multidimensional optical fractionation of colloidal particles with holographic verification," *Physical Review Letters* **104**(2), p. 028302, 2010.

[143] K. C. Neuman and S. M. Block, "Optical Trapping.," *The Review of Scientific Instruments* **75**(9), pp. 2787–2809, 2004.

[144] J. Brody, P. Yager, R. Goldstein, and R. Austin, "Biotechnology at low Reynolds numbers," *Biophysical Journal* **71**(6), pp. 3430–3441, 1996.

[145] T. Squires and S. Quake, "Microfluidics: Fluid physics at the nanoliter scale," *Reviews of Modern Physics* **77**(3), pp. 977–1026, 2005.

[146] H. Bruus, *Theoretical Microfluidics*, Oxford University Press, 2008.

[147] E. Purcell, "Life at low Reynolds number," *American Journal of Physics* **45**(3), p. 11, 1977.

[148] O. Reynolds, "An experimental investigation of the circumstances which determine whether the motion of water shall be direct or sinuous, and of the law of resistance in parallel channels," *Philosophical Transactions of the Royal Society of London* **174**(1883), pp. 935–982, 1883.

[149] B. Weigl, R. Bardell, and C. Cabrera, "Lab-on-a-chip for drug development," *Advanced Drug Delivery Reviews* **55**(3), pp. 349–377, 2003.

[150] G.-B. Lee, C.-C. Chang, S.-B. Huang, and R.-J. Yang, "The hydrodynamic focusing effect inside rectangular microchannels," *Journal of Micromechanics and Microengineering* **16**(5), pp. 1024–1032, 2006.

[151] J. P. Golden, J. S. Kim, J. S. Erickson, L. R. Hilliard, P. B. Howell, G. P. Anderson, M. Nasir, and F. S. Ligler, "Multi-wavelength microflow cytometer using groove-generated sheath flow," *Lab on a Chip* **9**(13), pp. 1942–1950, 2009.

[152] A. Kummrow, J. Theisen, M. Frankowski, A. Tuchscheerer, H. Yildirim, K. Brattke, M. Schmidt, and J. Neukammer, "Microfluidic structures for flow cytometric analysis of hydrodynamically focussed blood cells fabricated by ultraprecision micromachining," *Lab on a Chip* **9**(7), pp. 972–981, 2009.

[153] D. A. Ateya, J. S. Erickson, P. B. Howell, L. R. Hilliard, J. P. Golden, and F. S. Ligler, "The good, the bad, and the tiny: a review of microflow cytometry," *Analytical and Bioanalytical Bhemistry* **391**(5), pp. 1485–1498, 2008.

[154] C. M. Lin, Y. S. Lai, H. P. Liu, C. Y. Chen, and A. M. Wo, "Trapping of bioparticles via microvortices in a microfluidic device for bioassay applications.," *Analytical Chemistry* **80**(23), pp. 8937–8945, 2008.

[155] Y. Gambin, C. Simonnet, V. VanDelinder, A. Deniz, and A. Groisman, "Ultrafast microfluidic mixer with three-dimensional flow focusing for studies of biochemical kinetics," *Lab on a Chip* **10**(5), pp. 598–609, 2010.

[156] N. Watkins, B. M. Venkatesan, M. Toner, W. Rodriguez, and R. Bashir, "A robust electrical microcytometer with 3-dimensional hydrofocusing," *Lab on a Chip* **9**(22), pp. 3177–3184, 2009.

[157] M. G. Lee, S. Choi, and J.-K. Park, "Three-dimensional hydrodynamic focusing with a single sheath flow in a single-layer microfluidic device," *Lab on a Chip* **9**(21), pp. 3155–3160, 2009.

[158] P. B. Howell, J. P. Golden, L. R. Hilliard, J. S. Erickson, D. R. Mott, and F. S. Ligler, "Two simple and rugged designs for creating microfluidic sheath flow," *Lab on a Chip* **8**(7), pp. 1097–1103, 2008.

[159] A. J. DeMello, "Control and detection of chemical reactions in microfluidic systems," *Nature* **442**(7101), pp. 394–402, 2006.

[160] A. M. Streets and S. R. Quake, "Ostwald Ripening of Clusters during Protein Crystallization," *Physical Review Letters* **104**(17), p. 178102, 2010.

[161] A. E. Nkodo, J. M. Garnier, B. Tinland, H. Ren, C. Desruisseaux, L. C. McCormick, G. Drouin, and G. W. Slater, "Diffusion coefficient of DNA molecules during free solution electrophoresis," *Electrophoresis* **22**(12), pp. 2424–2432, 2001.

[162] A. Goldman, R. Cox, and H. Brenner, "Slow viscous motion of a sphere parallel to a plane wall. i. motion through a quiescent fluid," *Chemical Engineering Science* **22**(4), pp. 637–651, 1967.

[163] G. P. Krishnan and D. T. Leighton, "Inertial lift on a moving sphere in contact with a plane wall in a shear-flow," *Physics of Fluids* **7**(11), pp. 2538–2545, 1995.

[164] Y. Zhang and S. Neelamegham, "Estimating the efficiency of cell capture and arrest in flow chambers: Study of neutrophil binding via e-selectin and icam-1," *Biophysical Journal* **83**(4), pp. 1934–1952, 2002.

[165] B. Lincoln and J. Guck, *The Microfluidic Optical Stretcher*. PhD thesis, University of Leipzig, April 2006.

[166] N. Wu, Y. Zhu, S. Brown, J. Oakeshott, T. S. Peat, R. Surjadi, C. Easton, P. W. Leech, and B. A. Sexton, "A PMMA microfluidic droplet platform for in vitro protein expression using crude E. coli S30 extract," *Lab on a Chip* **9**(23), pp. 3391–3398, 2009.

[167] R. Osellame, V. Maselli, R. M. Vazquez, R. Ramponi, and G. Cerullo, "Integration of optical waveguides and microfluidic channels both fabricated by femtosecond laser irradiation," *Applied Physics Letters* **90**(23), p. 231118, 2007.

[168] H. I. Kirei, L. Oroszi, S. Valkai, and P. Ormos, "An all optical microfluidic sorter," *Acta Biologica Hungarica* **58**(1), pp. 139–148, 2007.

[169] K. P. Nichols, J. C. T. Eijkel, and H. J. G. E. Gardeniers, "Nanochannels in SU-8 with floor and ceiling metal electrodes and integrated microchannels," *Lab on a Chip* **8**(1), pp. 173–175, 2008.

[170] A. A. S. Bhagat, P. Jothimuthu, and I. Papautsky, "Photodefinable polydimethylsiloxane (PDMS) for rapid lab-on-a-chip prototyping," *Lab on a Chip* **7**(9), pp. 1192–1197, 2007.

[171] C.-S. Chen, D. N. Breslauer, J. I. Luna, A. Grimes, W.-C. Chin, L. P. Lee, and M. Khine, "Shrinky-Dink microfluidics: 3D polystyrene chips," *Lab on a Chip* **8**(4), pp. 622–624, 2008.

[172] A. W. Martinez, S. T. Phillips, G. M. Whitesides, and E. Carrilho, "Diagnostics for the developing world: microfluidic paper-based analytical devices.," *Analytical Chemistry* **82**(1), pp. 3–10, 2010.

[173] P. K. Yuen and V. N. Goral, "Low-cost rapid prototyping of flexible microfluidic devices using a desktop digital craft cutter," *Lab on a Chip* **10**(3), pp. 384–387, 2010.

[174] C. W. T. Yang, E. Ouellet, and E. T. Lagally, "Using Inexpensive Jell-O Chips for Hands-On Microfluidics Education," *Analytical Chemistry* , May 2010. 10.1021/ac902926x.

[175] U. VitroCom Inc., New Jersey 07046-0125, "www.vitrocom.com."

[176] Y. Xia and G. Whitesides, "Soft lithography," *Annual Review of Material Science* **28**, pp. 153–184, 1998.

[177] D. J. Campbell, K. J. Beckman, C. E. Calderon, P. W. Doolan, R. M. Ottosen, A. B. Ellis, and G. C. Lisensky, "Replication and compression of bulk and surface structures with polydimethylsiloxane elastomer," *Journal of Chemical Education* **75**, pp. 537–541, 1999.

[178] "Dow corning." http://www.dowcorning.com/content/discover/discoverchem/, August 2009.

[179] S. R. Quake and A. Scherer, "From micro- to nanofabrication with soft materials," *Science* **290**(5196), pp. 1536–1540, 2000.

[180] S. K. Sia and G. M. Whitesides, "Microfluidic devices fabricated in poly(dimethylsiloxane) for biological studies," *Electrophoresis* **24**(21), pp. 3563–3576, 2003.

[181] J. C. McDonald and G. M. Whitesides, "Poly(dimethylsiloxane) as a material for fabricating microfluidic devices," *Accounts of Chemical Research* **35**(7), pp. 491–499, 2002.

[182] J. Ng, I. Gitlin, A. Stroock, and G. Whitesides, "Components for integrated poly (dimethylsiloxane) microfluidic systems," *Electrophoresis* **23**(20), pp. 3461–3473, 2002.

[183] M. Unger, H. Chou, T. Thorsen, A. Scherer, and S. Quake, "Monolithic microfabricated valves and pumps by multilayer soft lithography," *Science* **288**(5463), p. 113, 2000.

[184] MicroChem, "Nano su-8 2000: Negative tone photoresist formulations 2035-2100." http://www.microchem.com, Accessed September 2009.

[185] T. Sikanen, S. Tuomikoski, R. A. Ketola, R. Kostiainen, S. Franssila, and T. Kotiaho, "Characterization of su-8 for electrokinetic microfluidic applications," *Lab on a Chip* **5**(8), pp. 888–896, 2005.

[186] A. D. Campo and C. Greiner, "Su-8: a photoresist for high-aspect-ratio and 3d submicron lithography," *Journal of Micromechanics and Microengineering* **17**(6), pp. R81–R95, 2007.

[187] D. Meyerhofer, "Characteristics of resist films produced by spinning," *Journal of Applied Physics* **49**(7), pp. 3993–3997, 1978.

[188] M. J. Madou, *Fundamentals of Microfabrication*, CRC Press Inc, 1 ed., 1997.

[189] Wikipedia, "http://en.wikipedia.org/wiki/piranha solution," Accessed September 2009.

[190] MicroChem, "Nano su-8 2000: Negative tone photoresist formulations 2000.5-2015, v4." http://www.microchem.com, Accessed September 2009.

[191] N. K. Metzger, E. M. Wright, and K. Dholakia, "Theory and simulation of the bistable behaviour of optically bound particles in the Mie size regime," *New Journal of Physics* **8**(8), pp. 139–139, 2006.

[192] B.-H. Jo, L. M. V. Lerberghe, K. M. Motsegood, and D. J. Beebe, "Three-Dimensional Micro-Channel Fabrication in Polydimethylsiloxane (PDMS) Elastomer," *Journal of Microelectromechanical Systems* **9**(1), pp. 76–81, 2000.

[193] K. Haubert, T. Drier, and D. Beebe, "PDMS bonding by means of a portable, low-cost corona system," *Lab on a Chip* **6**, pp. 1548–1549, 2006.

[194] S. J. Cran-McGreehin, K. Dholakia, and T. F. Krauss, "Monolithic integration of microfluidic channels and semiconductor lasers," *Optics Express* **14**(17), pp. 7224–7729, 2006.

[195] S. Mohanty and D. J. Beebe, "Chips & tips: Pdms connectors for macro to microfluidic interfacing." Lab on a Chip, October 2006.

[196] J. T. Blakely, R. Gordon, and D. Sinton, "Flow-dependent optofluidic particle trapping and circulation," *Lab on a Chip* **8**(8), pp. 1350–1356, 2008.

[197] N. Metzger, E. Wright, W. Sibbett, and K. Dholakia, "Visualization of optical binding of microparticles using a femtosecond fiber optical trap," *Optics Express* **14**(8), pp. 3677–3687, 2006.

[198] M. Burns, J. Fournier, and J. Golovchenko, "Optical Binding," *Physical Review Letters* **63**(12), pp. 1233–1236, 1989.

[199] M. Burns, J. Fournier, and J. Golovchenko, "Optical matter: crystallization and binding in intense optical fields," *Science* **249**(4970), pp. 749–754, 1990.

[200] V. Karásek and P. Zemánek, "Analytical description of longitudinal optical binding of two spherical nanoparticles," *Journal of Optics A: Pure and Applied Optics* **9**(8), pp. S215–S220, 2007.

[201] W. M. Lee, R. El-Ganainy, D. N. Christodoulides, K. Dholakia, and E. M. Wright, "Nonlinear optical response of colloidal suspensions.," *Optics Express* **17**(12), pp. 10277–10289, 2009.

[202] J. Rodriguez, "Quantum electrodynamics analysis of optical binding in counterpropagating beams and effect of particle size," *Optics Letters* **33**(19), pp. 2197–2199, 2008.

[203] J. M. Taylor and G. D. Love, "Optical binding mechanisms: a conceptual model for Gaussian beam traps," *Optics Express* **17**(17), p. 15381, 2009.

[204] K. Dholakia and P. Zemánek, "Colloquium: Gripped by light: Optical binding," *Reviews of Modern Physics* **82**(2), pp. 1767–1791, 2010.

[205] P. Bartlett, S. I. Henderson, and M. J. Steven, "Measurement of the hydrodynamic forces between two polymer-coated spheres," *Philosophical Transactions of The Royal Society A* **359**(1782), pp. 883–895, 2001.

[206] J. Meiners and S. Quake, "Direct measurement of hydrodynamic cross correlations between two particles in an external potential," *Physical Review Letters* **82**(10), pp. 2211–2214, 1999.

[207] B. Brooks and T. Brooks. http://www.flickr.com/photos/basilb, Accessed December 2009.

[208] Wikipedia, "Total internal reflection in pmma." http://en.wikipedia.org/wiki/File:TIR in PMMA.jpg, Accessed December 2009.

[209] D. Axelrod, "Total Internal Reflection Fluorescence," *Annual Review of Biophysics and Biomolecular Structure* **13**(1), pp. 247–268, 1984.

[210] F. de Fornel, *Evanescent waves : from Newtonian optics to atomic optics*, Springer, Berlin, 2001.

[211] D. Axelrod, E. H. Hellen, and R. M. Fullbright, *Topics in Fluorescence Spectroscopy*, vol. 3, ch. Total internal reflection fluorescence, p. 289. Plenum Press, New York, 1992.

[212] D. Axelrod, "Selective imaging of surface fluorescence with very high aperture microscope objectives," *Journal of Biomedical Optics* **6**(1), pp. 6–13, 2001.

[213] D. Toomre and D. J. Manstein, "Lighting up the cell surface with evanescent wave microscopy," *Trends in Cell Biology* **11**(7), pp. 298–303, 2001.

[214] A. Y. Kobitski, C. D. Heyes, and G. U. Nienhaus, "Total internal reflection fluorescence microscopy–a powerful tool to study single quantum dots," *Applied Surface Science* **234**(1-4), pp. 86–92, 2004.

[215] H. Schneckenburger, "Total internal reflection fluorescence microscopy: technical innovations and novel applications," *Current Opinion in Biotechnology* **16**(1), pp. 13 – 18, 2005.

[216] Condeelis et al. http://www.einstein.yu.edu/aif/instructions/tirf/index.htm, Accessed December 2009.

[217] M. Gu, P. C. Ke, and X. S. Gan, "Trapping force by a high numerical-aperture microscope objective obeying the sine condition," *Review of Scientific Instruments* **68**(10), pp. 3666–3668, 1997.

[218] M. Gu, *Advanced Optical Imaging Theory*, Optical Sciences, Springer, Heidelberg, 2000.

[219] I. Brevik, "Experiments in phenomenological electrodynamics and the electromagnetic energy-momentum tensor," *Physics Reports-Review Section of Physics Letters* **52**(3), pp. 133–201, 1979.

[220] J. P. Barton and D. R. Alexander, "Fifth-order corrected electromagnetic field components for a fundamental gaussian beam," *Journal of Applied Physics* **66**(7), pp. 2800–2802, 1989.

[221] J. P. Barton, D. R. Alexander, and S. A. Schaub, "Theoretical determination of net radiation force and torque for a spherical particle illuminated by a focused laser beam," *Journal of Applied Physics* **66**(10), pp. 4594–4602, 1989.

[222] E. Almaas and I. Brevik, "Radiation forces on a micrometer-sized sphere in an evanescent field," *Journal of the Optical Society of America B-Optical Physics* **12**(12), pp. 2429–2438, 1995.

[223] A. H. J. Yang and D. Erickson, "Stability analysis of optofluidic transport on solid-core waveguiding structures," *Nanotechnology* **19**(4), p. 045704, 2008.

[224] I. Brevik, T. A. Sivertsen, and E. Almaas, "Radiation forces on an absorbing micrometer-sized sphere in an evanescent field," *Journal of the Optical Society of America B-Optical Physics* **20**(8), pp. 1739–1749, 2003.

[225] F. Charru, E. Larrieu, J. B. Dupont, and R. Zenit, "Motion of a particle near a rough wall in a viscous shear flow," *Journal of Fluid Mechanics* **570**, pp. 431–453, 2007.

[226] S. B. Kim, J. H. Kim, and S. S. Kim, "Theoretical development of in situ optical particle separator: cross-type optical chromatography," *Applied Optics* **45**(27), pp. 6919–6924, 2006.

[227] L. Bonetta, "The inside scoop-evaluating gene delivery methods," *Nature Methods* **2**(11), pp. 875–883, 2005.

[228] M. J. Chappell, N. D. Evans, R. J. Errington, I. A. Khan, L. Campbell, R. Ali, K. R. Godfrey, and P. J. Smith, "A coupled drug kinetics-cell cycle model to analyse the response of human cells to intervention by topotecan," *Computer Methods and Programs in Biomedicine* **89**(2), pp. 169–178, 2008.

[229] D. J. Stevenson, F. J. Gunn-Moore, P. Campbell, and K. Dholakia, "Single cell optical transfection," *Journal of the Royal Society Interface* **7**, pp. 863–871, 2010.

[230] X. Gao, K. S. Kim, and D. X. Liu, "Nonviral gene delivery: What we know and what is next," *AAPS Journal* **9**(1), pp. E92–E104, 2007.

[231] J. A. Wolff, R. W. Malone, P. Williams, W. Chong, G. Acsadi, A. Jani, and P. L. Felgner, "Direct gene-transfer into mouse muscle invivo," *Science* **247**(4949), pp. 1465–1468, 1990.

[232] E. Neumann, M. Schaeferridder, Y. Wang, and P. H. Hofschneider, "Gene-transfer into mouse lyoma cells by electroporation in high electric-fields," *Embo Journal* **1**(7), pp. 841–845, 1982.

[233] N. S. Yang, J. Burkholder, B. Roberts, B. Martinell, and D. McCabe, "Invivo and invitro gene-transfer to mammalian somatic-cells by particle bombardment," *Proceedings of the National Academy of Sciences of the United States of America* **87**(24), pp. 9568–9572, 1990.

[234] P. L. Felgner, T. R. Gadek, M. Holm, R. Roman, H. W. Chan, M. Wenz, J. P. Northrop, G. M. Ringold, and M. Danielsen, "Lipofection - a highly efficient, lipid-mediated dna-transfection procedure," *Proceedings of the National Academy of Sciences of the United States of America* **84**(21), pp. 7413–7417, 1987.

[235] K. L. Douglas, "Toward development of artificial viruses for gene therapy: A comparative evaluation of viral and non-viral transfection," *Biotechnology Progress* **24**(4), pp. 871–883, 2008.

[236] A. Lawrie, A. F. Brisken, S. E. Francis, D. C. Cumberland, D. C. Crossman, and C. M. Newman, "Microbubble-enhanced ultrasound for vascular gene delivery," *Gene Therapy* **7**(23), pp. 2023–2027, 2000.

[237] M. Tsukakoshi, S. Kurata, Y. Nomiya, Y. Ikawa, and T. Kasuya, "A novel method of dna transfection by laser microbeam cell surgery," *Applied Physics B: Lasers and Optics* **35**(3), pp. 135–140, 1984.

[238] X. Tsampoula, *Femtosecond cellular transfection using novel laser beam geometries*. PhD thesis, University of St Andrews, 2009.

[239] C. T. A. Brown, D. J. Stevenson, X. Tsampoula, C. McDougall, A. A. Lagatsky, W. Sibbett, F. J. Gunn-Moore, and K. Dholakia, "Enhanced operation of femtosecond lasers and applications in cell transfection," *Journal of Biophotonics* **1**(3), pp. 183–199, 2008.

[240] S. Mehier-Humbert and R. H. Guy, "Physical methods for gene transfer: Improving the kinetics of gene delivery into cells," *Advanced Drug Delivery Reviews* **57**(5), pp. 733–753, 2005.

[241] M. L. Torres-Mapa, L. Veldhuis, M. Ploschner, K. Dholakia, and F. Gunn-Moore, "Transient transfection of mammalian cells using a violet diode laser," *Journal of Biomedical Optics* **15**(2), 2010.

[242] L. Paterson, B. Agate, M. Comrie, R. Ferguson, T. Lake, J. Morris, A. Carruthers, C. T. Brown, W. Sibbett, P. Bryant, F. Gunn-Moore, A. Riches, and

K. Dholakia, "Photoporation and cell transfection using a violet diode laser," *Optics Express* **13**(2), pp. 595–600, 2005.

[243] H. Schneckenburger, A. Hendinger, R. Sailer, W. S. L. Strauss, and M. Schmidtt, "Laser-assisted optoporation of single cells," *Journal of Biomedical Optics* **7**(410), pp. 410–416, 2002.

[244] A. V. Nikolskaya, V. P. Nikolski, and I. R. Efimov, "Gene printer: Laser-scanning targeted transfection of cultured cardiac neonatal rat cells," *Cell Communication and Adhesion* **13**(4), pp. 217–222, 2006.

[245] G. Palumbo, M. Caruso, E. Crescenzi, M. F. Tecce, G. Roberti, and A. Colasanti, "Targeted gene transfer in eucaryotic cells by dye-assisted laser optoporation," *Journal of Photochemistry and Photobiology B-Biology* **36**(1), pp. 41–46, 1996.

[246] I. B. Clark, E. G. Hanania, J. Stevens, M. Gallina, A. Fieck, R. Brandes, B. O. Palsson, and M. R. Koller, "Optoinjection for efficient targeted delivery of a broad range of compounds and macromolecules into diverse cell types," *Journal of Biomedical Optics* **11**(1), p. 014034, 2006.

[247] T. Knoll, L. Trojan, S. Langbein, S. Sagi, P. Alken, and M. S. Michel, "Impact of holmium : Yag and neodymium : Yag lasers on the efficacy of dna delivery in transitional cell carcinoma," *Lasers in Medical Science* **19**(1), pp. 33–36, 2004.

[248] H. Schinkel, P. Jacobs, S. Schillberg, and M. Wehner, "Infrared picosecond laser for perforation of single plant cells," *Biotechnology and Bioengineering* **99**(1), pp. 244–248, 2008.

[249] L. E. Barrett, J. Y. Sul, H. Takano, E. J. Van Bockstaele, P. G. Haydon, and J. H. Eberwine, "Region-directed phototransfection reveals the functional significance of a dendritically synthesized transcription factor," *Nature Methods* **3**(6), pp. 455–460, 2006.

[250] M. Lei, H. Xu, H. Yang, and B. Yao, "Femtosecond laser-assisted microinjection into living neurons," *Journal of Neuroscience Methods* **174**(2), pp. 215–218, 2008.

[251] P. Mthunzi, K. Dholakia, and F. Gunn-Moore, "Photo-transfection of mammalian cells using femtosecond laser pulses: optimisation and applicability to stem cell differentiation," *Journal of Biomedical Optics* **15**(2), p. 041507, 2010.

[252] C. Peng, R. E. Palazzo, and I. Wilke, "Laser intensity dependence of femtosecond near-infrared optoinjection," *Physical Review E Statistical, Nonlinear and Soft Matter Physics* **75**(1), p. 041903, 2007.

[253] D. Stevenson, B. Agate, X. Tsampoula, P. Fischer, C. T. A. Brown, W. Sibbett, A. Riches, F. Gunn-Moore, and K. Dholakia, "Femtosecond optical transfection of cells: viability and efficiency," *Optics Express* **14**(16), pp. 7125–7133, 2006.

[254] U. K. Tirlapur and K. Konig, "Cell biology: Targeted transfection by femtosecond laser," *Nature* **418**(6895), pp. 290–291, 2002.

[255] X. Tsampoula, K. Taguchi, T. Cizmar, V. Garcés-Chávez, N. Ma, S. Mohanty, K. Mohanty, F. Gunn-Moore, and K. Dholakia, "Fibre based cellular transfection," *Optics Express* **16**, pp. 17007–17013, 2008.

[256] A. Uchugonova, K. Konig, R. Bueckle, A. Isemann, and G. Tempea, "Targeted transfection of stem cells with sub-20 femtosecond laser pulses," *Optics Express* **16**(13), pp. 9357–9364, 2008.

[257] A. Yamaguchi, Y. Hosokawa, G. Louit, T. Asahi, C. Shukunami, Y. Hiraki, and H. Masuhara, "Nanoparticle injection to single animal cells using femtosecond laser-induced impulsive force," *Applied Physics A-Materials Science & Processing* **93**(1), pp. 39–43, 2008.

[258] E. Zeira, A. Manevitch, A. Khatchatouriants, O. Pappo, E. Hyam, M. Darash-Yahana, E. Tavor, A. Honigman, A. Lewis, and E. Galun, "Femtosecond in-

frared laser - an efficient and safe in vivo gene delivery system for prolonged expression," *Molecular Therapy* **8**(2), pp. 342–350, 2003.

[259] J. Baumgart, W. Bintig, A. Ngezahayo, S. Willenbrock, H. M. Escobar, W. Ertmer, H. Lubatschowski, and A. Heisterkamp, "Quantified femtosecond laser based opto-perforation of living gfshr-17 and mth53a cells," *Optics Express* **16**(5), pp. 3021–3031, 2008.

[260] S. Sagi, T. Knoll, L. Trojan, A. Schaaf, P. Alken, and M. Michel, "Gene delivery into prostate cancer cells by holmium laser application," *Prostate Cancer and Prostatic Diseases* **6**(2), pp. 127–130, 2003.

[261] D. Stevenson, F. Gunn-Moore, P. Campbell, and K. Dholakia, *The Handbook of Photonics for Medical Science*, ch. Transfection by optical injection, pp. 87–117. CRC Press, USA, 1 ed., 2010.

[262] Y. A. Badr, M. A. Kereim, M. A. Yehia, O. O. Fouad, and A. Bahieldin, "Production of fertile transgenic wheat plants by laser micropuncture," *Photochemical & Photobiological Sciences* **4**(10), pp. 803–807, 2005.

[263] A. Vogel, N. Linz, S. Freidank, and G. Paltauf, "Femtosecond-laser-induced nanocavitation in water: Implications for optical breakdown threshold and cell surgery," *Physical Review Letters* **100**(3), p. 038102, 2008.

[264] F. Stracke, I. Rieman, and K. Konig, "Optical nanoinjection of macromolecules into vital cells," *Journal of Photochemistry and Photobiology B-Biology* **81**(3), pp. 136–142, 2005.

[265] T. Čižmár, V. Kollárová, X. Tsampoula, F. Gunn-Moore, W. Sibbett, Z. Bouchal, and K. Dholakia, "Generation of multiple bessel beams for a biophotonics workstation," *Optics Express* **16**(18), pp. 14024–14035, 2008.

[266] A. Adamo and K. F. Jensen, "Microfluidic based single cell microinjection," *Lab on a Chip* **8**(8), pp. 1258–1261, 2008.

[267] A. Noori, P. R. Selvaganapathy, and J. Wilson, "Microinjection in a microfluidic format using flexible and compliant channels and electroosmotic dosage control," *Lab on a Chip* **9**(22), pp. 3202–3211, 2009.

[268] R. Ziv, Y. Steinhardt, G. Pelled, D. Gazit, and B. Rubinsky, "Micro-electroporation of mesenchymal stem cells with alternating electrical current pulses," *Biomedical Microdevices* **11**(1), pp. 95–101, 2009.

[269] N. Bao, Y. Zhan, and C. Lu, "Microfluidic electroporative flow cytometry for studying single-cell biomechanics," *Analytical Chemistry* **80**(20), pp. 7714–7719, 2008.

[270] J. Wang, M. J. Stine, and C. Lu, "Microfluidic cell electroporation using a mechanical valve," *Analytical Chemistry* **79**(24), pp. 9584–9587, 2007.

[271] Y. Zhan, J. Wang, N. Bao, and C. Lu, "Electroporation of cells in microfluidic droplets," *Analytical Chemistry* **81**(5), pp. 2027–2031, 2009.

[272] T. Zhu, C. Luo, J. Huang, C. Xiong, Q. Ouyang, and J. Fang, "Electroporation based on hydrodynamic focusing of microfluidics with low dc voltage," *Biomedical Microdevices* **12**(1), pp. 35–40, 2009.

[273] C. M. Pitsillides, E. K. Joe, X. Wei, R. R. Anderson, and C. P. Lin, "Selective cell targeting with light-absorbing microparticles and nanoparticles," *Biophysical Journal* **84**(6), pp. 4023–4032, 2003.

[274] J. Ng and C. T. Chan, "Size-selective optical forces for microspheres using evanescent wave excitation of whispering gallery modes," *Applied Physics Letters* **92**(25), p. 251109, 2008.

[275] S. Gaugiran, S. Gétin, J. M. Fedeli, and J. Derouard, "Polarization and particle size dependence of radiative forces on small metallic particles in evanescent optical fields. Evidences for either repulsive or attractive gradient forces," *Optics Express* **15**(13), pp. 8146–8156, 2007.

[276] J. Krajniak and L. Hang, "Long-term high-resolution imaging and culture of c. elegans in chip-gel hybrid microfluidic device for developmental studies," *Lab on a Chip* , p. DOI: 10.1039/c001986k, 2010.

[277] H. Andersson and A. van den Berg, "Microfluidic devices for cellomics: a review," *Sensors and Actuators B: Chemical* **92**(3), pp. 315–325, 2003.

[278] M. U. Kopp, "Chemical Amplification: Continuous-Flow PCR on a Chip," *Science* **280**(5366), pp. 1046–1048, 1998.

[279] C. Zhang, Z. Zhao, N. A. Abdul Rahim, D. van Noort, and H. Yu, "Towards a human-on-chip: culturing multiple cell types on a chip with compartmentalized microenvironments," *Lab on a Chip* **9**(22), pp. 3185–3192, 2009.